MICROMECHANICAL MODELING OF THE DUCTILE FRACTURE PROCESS

A Dissertation

Presented to

The Graduate Faculty of The University of Akron

In Partial Fulfillment

of the Requirements for the Degree

Doctor of Philosophy

Tuo Luo

December, 2018

MICROMECHANICAL MODELING OF THE DUCTILE FRACTURE PROCESS

Tuo Luo

Dissertation

Approved:

Advisor
Dr. Xiaosheng Gao

Committee Member
Dr. Chang Ye

Committee Member
Dr. Gregory Morscher

Committee Member
Dr. Ernian Pan

Committee Member
Dr. Chien-Chung Chan

Accepted:

Department Chair
Dr. Sergio Felicelli

Dean of the College
Dr. Donald P. Visco Jr.

Dean of the Graduate School
Dr. Chand K. Midha

Date

ABSTRACT

This dissertation aims to develop valid numerical approaches to investigate the micromechanics of ductile fracture process and predict the ductile material failure under various loading conditions.

As the first portion of this work, a layered unit cell micromechanics model is proposed. This model consists of three void containing material units stacked in the direction normal to the localization plane. Localization takes place in the middle material unit while the two outer units undergo elastic recovery after failure occurs. Thus, a failure criterion is established as the material is considered failure when the macroscopic effective strain of the outer material units reaches the maximum value. Comparisons of the present model with several previous models suggest that the present model is not only easy to implement in finite element analysis but also more suitable to robustly determine the failure strain. A series of unit cell analyses are conducted for various macroscopic stress triaxialities and Lode parameters to investigate the dependency of failure strain on stress state. The analysis results also reveal the effect of the stress state on the deformed void shape within and near the localization band. Additionally, analyses are conducted to demonstrate the effect of the voids existing outside the localization band.

Next, the unit cell model is utilized to investigate the effect of hydrogen on ductile fracture demonstrated by its influence on the process of void growth and coalescence. The

evolution of local stress and deformation states results in hydrogen redistribution in the material, which in turn changes the material's flow property due to the hydrogen enhanced localized plasticity effect. The result shows that hydrogen reduces the ductility of the material by accelerating void growth and coalescence, and the effect of hydrogen on ductile fracture is strongly influenced by the stress state experienced by the material, as characterized by the stress triaxiality and the Lode parameter.

The predicted material responses of three modified Gurson models are also investigated: GTN model, shear-modified-GTN model, and the shear-modified-GTN applied with anisotropic material model. A single material point test model equivalents to a computational cell of Gurson type models is utilized to demonstrate the effect of damage parameters and its evolution through the loading process when undergoing proportional stress loading. The shear-modified-GTN with anisotropic material model is implemented and calibrated using experimental data of commercially pure titanium, which exhibits complex plastic anisotropy and tension-compression asymmetry. The predicted results show good agreement with the experimental results obtained from various loading applications and specimen geometries. In addition, the predicted results also reveal the important effect of volumetric damage and shear damage under the influence of plastic anisotropy.

ACKNOWLEDGMENT

First and foremost, I need to thank Dr. Xiaosheng Gao, my advisor and committee chair. Your help and guidance allowed me to move through this process. You believed in my research potential and encouraged me to join your group. You empowered me when I had doubts and pushed me to learn and expand my research abilities. Your dedication and immerse knowledge have always inspired me. I have no doubt that what I have learned from you, I will carry forward in my own career.

I am also grateful to my committee members: Dr. Ernian Pan, Dr. Gregory Morscher, Dr. Chang Ye, and Dr. Chien-Chuang Chan. Each of you brought your own expertise and perspective to this research which only strengthened this dissertation. Many thanks to each of you for your thoughtful feedback and encouragement. Additional thanks to Dr. Yingcai Xiao, this dissertation committee would never be formed without your expertise and support.

I want to thank my friends and group members at The University of Akron, including Jun Zhou, Jinyuan Zhai, Clayton Reakes, Chuanshi Huang, and Chuan Zeng for the stimulating discussions, for the sleepless nights and for all the fun we have had in the last five years.

This dissertation would be impossible to complete without the support from my family. I am grateful that my parents and parents-in-law are always patient and supportive.

Thank my wonderful wife Yao and son Ryan for your understanding during this process, especially if it meant I needed to divert time away to work on this dissertation. This work is dedicated to them.

TABLE OF CONTENTS

Page

LIST OF TABLES

LIST OF FIGURES

Figure Page

CHAPTER I

INTRODUCTION

1.1 Motivations and Background

Fracture is the phenomenon that an object separated into two or more pieces under stress. The understanding of fracture is partially intuitive for us as this phenomenon occurs everywhere naturally or have been utilized deliberately. Historically, human gain and apply knowledge of fracture when interacting with environment. For example, as early as Neolithic age, human have used moose antler to knap brittle flint to make sharp-edged stone tools, and in ancient Asia, metal workers have practiced co-fusion steel-making technique to create steel blades that are less prone to fracture upon impact.

The scientific investigation of the mechanics and physics of fracture starts after the industrial revolution. In this period, massive types of new materials were introduced to the manufacture of products and understanding the material's fracture limit is vital for successful product design. As science and technology advanced, structures also became more colossal and complex, and unwanted fracture were causing significantly more damage to our society in terms of human lives and properties compare to pre-industrial revolution times.

Among all the building materials, metals were widely used to construct surface and air vehicles, buildings and structures. Other than the appreciated high strength-weight ratio of metal, another reason for the extensive application of metal is that upon failure, many

types of metal will deform plastically before fracture. This much-appreciated phenomenon can slow down the fracture process as a large amount of energy is absorbed by plastic deformation. Such that errors in the design process will less likely result in immediate catastrophic failure and allow more time to correct problems. This property of deforming plastically before the fracture is called ductility, we say material with this property exhibits ductile fracture in contrast to brittle fracture.

Later, the accidents of Liberty ships of US during World War II made researchers aware certain ductile material could behave like brittle material under special circumstances, in this case, under low temperature. To prevent future disaster, intensive studies were promoted in the field of fracture mechanics. Since then, our understanding of how ductile material fails and our ability to prevent such failure has increased considerably. For example, as shown in Fig. 1.1, the frontal offset crash test of two automobiles built in 1959 (right) and 2009 (left) from the same manufacturer shows the dramatic but expected difference of structural integrity from 50 years apart. We will briefly review the development of fracture mechanics and damage mechanics in the following part.

Figure 1.1. After the 40-mph frontal offset crash test involving two Chevrolets, the 2009 Malibu's occupant compartment remained intact (left), while the one in the 1959 Bel Air (right) collapsed.

1.2 Fracture mechanics and damage model

The hypothesis and investigation of fracture mechanics start with macroscopic approaches as a direct application of classical continuum mechanics and later shifted the focus to the concept of defect. The defect could be a presumed or existing crack on a structural, and by computing the crack extension by fatigue or the plastic energy release rate at the crack tip, the fracture phenomenon could be estimated under the assumption of the crack extending does not change local stress distribution. Although these phenomenological methods have proven useful to quantify life expectancy of structural components by applications in the aerospace area, the assumption of existing crack limited the prediction of crack initiation.

Later a fundamental model developed by Gurson has allowed the arbitrary direction of crack growth, even without an initial crack, be predicted using numerical models. The Gurson ductile damage model is based on a micro-mechanics observation of ductile fracture, namely, the nucleation, growth, and coalescence of the void. The original Gurson model estimates the ductile damage based on yield potential for dilatant plasticity, using porosity of material (f) as damage parameter, which obeys a growth law consistent with the mechanics of void growth under axisymmetric stress state. Upon the framework of Gurson model, the immediate modifications of this model such as GTN model, can consider more complex factors such as isotropic material hardening, void nucleation, and void coalescence. Later, other modifications such as GLD model has considered the effect of void shape, and some considered anisotropic matrix material.

Despite its popularity and success, the above extensions of Gurson model are mainly based on solutions for voids subject to axisymmetric stressing and therefore ignores

the damage induced softening under shear dominated stressing. As experimental evidence from Bao and Wierzbicki (2004) has shown the softening under shear dominated stress state cannot be ignored, more recently modifications to the Gurson-type porous models including the work by Nahshon and Hutchinson (2008), Xue (2008), Zhou et al. (2014), Malcher et al. (2014), among others to consider shear-induced damage. These works introduced new shear damage related parameters to the GTN model based on experimental data on shear localization or void ligaments estimation under shear strain accumulation.

1.3 Unit cell modeling

While detailed and carefully designed experiments can provide many insights into the ductile fracture process, monitoring the stress state evolution on the microscale and obtaining reliable fracture strain remain as major obstacles. Micromechanical modeling provides a viable alternative. Finite element micromechanical analysis has proven to be extremely useful in guiding the development of improved ductile fracture models.

In the damage models, the constitutive equations are describing the relations between stress and strain in a solid element and representing the homogenized behaviors of the microstructures in the element. In a finite element application, it may sound strange as a finite element is considered a mathematical entity to solve boundary value problems in continuum mechanics because this implies the element size is a material parameter. But if consider element as a representative volume element (RVE), a computational unit cell, it becomes physically meaningful. Based on this understanding, backed up by experimental evidence, the investigation of the effect of stress state on a micromechanics unit cell model

had been considering an effective method to reveal the microstructure related ductile mechanics and has provided essential insights for developing new damage models.

As a long history of experiments and unit cell model result shows, the ductile fracture process in the metal is strongly influenced by the stress state subjected by the material. In these materials, voids nucleated at inclusions by de-cohesion of the particle-matrix interface or by particle cracking (van Stone et al., 1985; Garrison and Moody, 1987). These voids then grow in size under high triaxial stress states and then coalescence by inter-void flow localization, leading to fracture initiation (Benzerga and Leblond, 2010). On the other hand, voids change little in volume but significant in orientation and shape under shear-dominated stress state and the material fails after strain localization into a narrow band (Tvergaard, 2008, 2009; Nielsen et al., 2012).

Although the phenomenological ductile fracture process has been clearly shown in previous unit cell analysis, but the boundary condition is highly idealized and assumed uniform stress state and deformation across every material point, therefore does not reflect the multi-scale nature of the unit cell model and cannot be compared with macroscopic experiment as the reality of fracture tends to localize into one layer of material is conflict with unit cell boundary condition. The unit cell model in Chapter III is an approach to addressing this issue and hopefully will bring some attention to this problem.

1.4 Dissertation structure

Different aspects of research objectives to be achieved through this dissertation are listed as the following:

1) Develop a reliable failure criterion to determine the material failure strain of unit cell and study the effect of stress state on ductile fracture mechanics. Analyze the effect of voids existing outside the localization band to the fracture mechanics to comprehend ductile fracture on a multi-scale basis.
2) Study the effect of hydrogen embrittlement on ductile material mechanics using a unit cell model. Determine the influence of hydrogen on the process of void growth and coalescence under various stress state.
3) Investigate the damage evolution of various Gurson type model extensions including a shear modified model and a model accounting material anisotropy. Evaluate the capability of these models to differential volumetric damage and shear damage through a single material point analysis, as well as calibration and verification with experimental data.

Here is a simple outline of the dissertation structure.

Chapter I is a general introduction, it reviews the motivations and background of this research.

Chapter II will introduce the stress invariants and its functions to specify stress state and discuss the elastic and plastic response of material prior considering fracture mechanics, specifically the plasticity response of J_2 material and a tension-compression asymmetry anisotropic material.

Chapter III presents a unit cell model consists of three void containing material units to investigate its multi-scale nature, and to establish a more reliable failure criterion compare to previous studies. The analysis results obtained through this model will illustrate the effect of stress state on the ductile fracture process and on void shape deformation within and near the localization band.

Chapter IV will utilize the unit cell model to study the effect of hydrogen embrittlement on reducing the ductility of material, specifically by accelerating void growth and coalescence.

Chapter V is aiming to evaluate the damage evolution of several damage models, including GTN, Shear extended GTN and its application on anisotropic material. The evaluation is performed through a single material point analysis, focusing on the effect of stress state on volumetric damage and shear damage evolution, and anisotropic material response.

Chapter VI continues the evaluation of anisotropic shear extended GTN model by calibration and verification of the model with experimental data. With consideration of both volumetric and shear damage, the ductile damage model is capable of describing an anisotropic tension/compression asymmetry material and its ductile fracture process.

Chapter VII summarizes the main conclusions of this dissertation research and provides some pertinent recommendations for future studies.

CHAPTER II

PLASTICITY MODELS AND THE EFFECT OF STRESS STATE

2.1 Stress tensor and its invariants

In continuum mechanics, the stress tensor is a convenient and concise way of expressing the stress state inside the material. While stress component values are depending on coordinate, the principal stress values are independent of the coordinate, and so is the invariants. Here we define σ_{ij} as the stress tensor and σ_1, σ_2 and σ_3 be the principal stress values, then the hydrostatic stress (mean stress) can be expressed as

$$\sigma_m = \frac{1}{3} I_1 = \frac{1}{3}(\sigma_1 + \sigma_2 + \sigma_3) \tag{2.1}$$

where I_1 represents the first invariant of the stress. For general tensile stress state, I_1 is a positive value while for the compression, I_1 is negative. Let σ'_{ij}be the stress deviator tensor and σ'_1, σ'_2 and σ'_3 be principal values of the deviatoric stress tensor, *i.e.*

$$\sigma'_{ij} = \sigma_{ij} - \sigma_m \delta_{ij} \tag{2.2}$$

where δ_{ij} represents the Kronecker delta. The first invariant of the deviatoric stress tensor is calculated by σ'_{ii}, and the summation convention is adopted for repeated indices. It is obvious that the first invariant of the deviatoric stress tensor is zero. The second and third invariants of the stress deviator tensor are defined as

$$J_2 = \frac{1}{2}\sigma'_{ij}\sigma'_{ji} = -(\sigma'_1\sigma'_2 + \sigma'_2\sigma'_3 + \sigma'_3\sigma'_1)$$

$$= \frac{1}{6}[(\sigma_1 - \sigma_2)^2 + (\sigma_2 - \sigma_3)^2 + (\sigma_3 - \sigma_1)^2] \qquad (2.3)$$

$$J_3 = \det(\sigma'_{ij}) = \frac{1}{3}\sigma'_{ij}\sigma'_{jk}\sigma'_{ki} = \sigma'_1\sigma'_2\sigma'_3$$

The von Mises equivalent stress is related to the second invariant of stress deviator tensor as

$$\sigma_e = \sqrt{3J_2} \qquad (2.4)$$

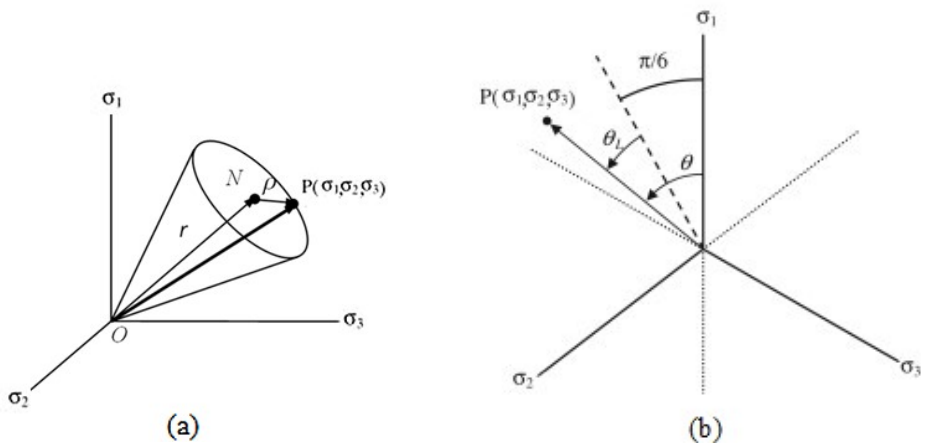

Figure 2.1 The stress state represented in (a) principal stress space (b) the π plane

A principal stress state (σ_1, σ_2, σ_3), can be mathematically represented by a vector $\overrightarrow{OP}$ in the principle stress coordinate system, with the three principal stresses as axes σ_1, σ_2, σ_3, as shown in Fig. 2.1(a). Consider a vector $\overrightarrow{ON}$ passing through the origin and having equal angles with the coordinate axes. $\overrightarrow{ON}$ is called the hydrostatic axis, where every point corresponds to $\sigma_1 = \sigma_2 = \sigma_3$.

The plane passing through the origin and perpendicular to $\overrightarrow{ON}$ is called the π plane as shown in Fig. 2.1(b) and the hydrostatic stress is zero on this plane. Consider an arbitrary

stress state at point P with stress components σ_1, σ_2, and σ_3. The stress vector $\overrightarrow{OP}$ can be decomposed into two components, the component $\vec{r}$ parallel to $\overrightarrow{ON}$ and the $\vec{\rho}$ on the octahedral plane whose normal direction is along the vector $\overrightarrow{ON}$ direction, then

$$r = \sqrt{3}\,\sigma_m = \frac{I_1}{\sqrt{3}} \tag{2.5}$$

$$\rho = \sqrt{\frac{2}{3}}\sigma_e = \sqrt{2J_2} \tag{2.6}$$

where σ_m and $\sigma_e$represent the hydrostatic stress (mean stress) and the equivalent stress, respectively. Consequently, the stress triaxiality ratio is

$$T = \frac{\sigma_m}{\sigma_e} = \frac{\sqrt{2}}{3}\frac{r}{\rho} \tag{2.7}$$

Therefore, for a given stress triaxiality ratio T, there are infinite stress states, each corresponds to a point on the surface of a cone with $\overrightarrow{ON}$ as the axis, Fig. 2.1(a). To distinguish these stress states having the same T (triaxiality ratio) value, we project their location to the π plane as point P, Fig. 2.1(b), then differentiate each by a Lode angle θ. There are many different variations on the definition of the Lode angle. In early work of Lode(1926), the Lode angle θ is defined as the angle measured counter-clockwise from the projection of the σ_1 axis to a point on the π plane (constant hydrostatic stress), as shown in Fig. 2. 1(b). σ_1, σ_2, and σ_3 are the projections of the principal stress axes on the π plane. Recently, Xue (2007) defined an alternative Lode angle, θ_L, relative to the shear meridian axis also shown in Fig. 2.1(b). The shear meridian axis (θ=30° or π/6) represents all states of stress that can be formed by combining a state of pure shear with a hydrostatic stress. There is also a tensile meridian axis (θ=0°) representing states of stress formed by

combining uniaxial tension with hydrostatic stress, and a compression meridian axis (θ=60° or π/3) formed by combining uniaxial compression with a hydrostatic stress. The two angles are related by $\theta_L = \theta - \frac{\pi}{6}$. The Lode angle θ has following relation with the stress invariants

$$\mathrm{Cos}(3\theta) = \frac{27J_3}{2\sigma_e^3} \tag{2.8}$$

Barsoum and Faleskog (2007) used a Lode parameter to describe Lode angle dependence, and the following relationship between principal stress and Lode angle can be established

$$\mu = \frac{2\sigma_2 - \sigma_1 - \sigma_3}{\sigma_1 - \sigma_3} = \sqrt{3}\tan\left(\theta - \frac{\pi}{6}\right) \tag{2.9}$$

Therefore, when von Mises equivalent stress (σ_e) is known, the stress triaxiality ratio (T) together with the Lode parameter (μ) can be used to specify the stress state.

2.2 Isotropic material model

Prior to investigating the damage mechanism of ductile material, the material's elastic and plastic response needs to be accurately described. When the deformation caused by loading is reversible, the material is considered in the elastic range. For elastic isotropic continuum material, it's elastic property can be described by Hooke's law. In tensor form, the stress and strain relationship can be defined simply as:

$$\sigma_{ij} = 3K\left(\frac{1}{3}\varepsilon_{kk}\delta_{ij}\right) + 2G\left(\varepsilon_{ij} - \frac{1}{3}\varepsilon_{kk}\delta_{ij}\right). \tag{2.10}$$

where σ_{ij} is the stress tensor, ε_{ij} the strain tensor, δ_{ij} is the Kronecker delata, K is the bulk modulus defined as $K = \frac{E}{3(1-2v)}$, and G is the shear modulus defined as $G = \frac{E}{2(1+v)}$, where E is the Young's modulus and v is the Possion's ratio.

When the material does not return to its previous dimension when the load is removed, there is a permanent irreversible deformation and the material is considered deformed plastically. A plasticity model is then required to describe such a phenomenon. A complete plasticity model needs a yield criterion to determine the elastic limit, a flow rule to regulate the direction of plastic deformation, and a hardening law to describe the evolution of subsequent yield surface. A popular, simple and reasonably accurate continuum plasticity model is the Von Mises plasticity theory. For a material that obeys J_2 flow plasticity theory, it's plasticity behavior is characterized by the Von Mises equivalent stress-strain curve. The equivalent stress-strain curve can be obtained from either a uniaxial tension test, a compression test or a pure torsion test. However, if the stress-strain curves obtained from those tests for a certain material are very different, the Mises plasticity theory is then considered insufficient to describe the plastic behavior of this material.

2.3 Anisotropic plasticity model

A typical type of material can not sufficiently describe by Von Mises plasticity theory is those has a hexagonal close-packed (HCP) crystal structure. Out of three common crystalline structures BCC, FCC and HCP, the HCP structure rarely have a sufficient number of slip systems for an arbitrary shape change and is the most likely to form deformation twins when strained. Both the effect of lack of slip system and crystal twinning can lead to a dramatic material strength differences in different directions of loading.

Historically, several typical anisotropic yield criteria with symmetric yield surface have been proposed to model anisotropic plasticity, including Hill (1948), Barlet (1989) have been evaluated using uniaxial and biaxial tension data, and considered been inadequate for considering tension/compression asymmetry by Andar et al. (2012) and Jia et, al. (2013). To account for both anisotropy and tension/compression asymmetry induced by twinning, several anisotropic criteria expressed in terms of the stress deviator was developed by Cazacu and Barlat (2004); Cazacu et al. (2006). Among those, Cazacu et al. (2006) is capable of describing such complex anisotropic matrix plasticity behavior. This model is based on a linear transformation of the deviatoric part of the Cauchy stress tensor, similar to previous studies by Barlat and coworkers (Barlat et al., 1991, 1997) and Lademo et al. (1999). The effective stress of this plasticity model is expressed as

$$\sigma_{Ae}(\Sigma_i, k) = \sigma_M$$

$$\sigma_{Ae} = m\sqrt{(|\Sigma_1| - k\Sigma_1)^2 + (|\Sigma_2| - k\Sigma_2)^2 + (|\Sigma_3| - k\Sigma_3)^2} \qquad (2.11)$$

with

$$m = \sqrt{\frac{1}{(|\theta_1| - k\theta_1)^2 + (|\theta_2| - k\theta_2)^2 + (|\theta_3| - k\theta_3)^2}}$$

$$\theta_1 = \frac{2}{3}L_{11} - \frac{1}{3}L_{12} - \frac{1}{3}L_{13}$$

$$\theta_2 = \frac{2}{3}L_{12} - \frac{1}{3}L_{22} - \frac{1}{3}L_{23}$$

$$\theta_3 = \frac{2}{3}L_{13} - \frac{1}{3}L_{23} - \frac{1}{3}L_{33}$$

where σ_M is the uniaxial tensile yield strength along an axis of orthotropy, k is used to capture the material strength differential effect, m is defined so that Eq. (2.11) is identically satisfied for uniaxial tensile loading along this orthotropy axis, Σ_i are the principal components of the transformed stress tensor and $\Sigma = L : \boldsymbol{K} : \sigma$, σ is the Cauchy stress tensor, $\boldsymbol{K}$ is the 4th order deviatoric projection operator, and L is the 4th order tensor which satisfies

the major and minor symmetric and the requirement of invariance with respect to the orthotropy group. This linear transformation "weights" the different components of the stress tensor of the anisotropic material in order to account for the anisotropy of the material. The transformed tensor is called the "isotropic plasticity equivalent (IPE) deviatoric stress tensor" (Karafillis and Boyce, 1993) and is used as the argument in the yield function of Eq. (2.11). To ensure that it reduces to the fourth-order identity tensor for isotropic conditions, the following constraints are imposed:

$$\begin{aligned} L_{11} + L_{12} + L_{13} &= 1 \\ L_{12} + L_{22} + L_{23} &= 1 \\ L_{13} + L_{23} + L_{33} &= 1 \end{aligned} \tag{2.12}$$

The additional constraints of Eq. (2.12) also ensure that the transformed stress tensor Σ is deviatoric.

When the material deforms plastically, the inelastic part of the deformation is defined by the flow rule

$$\dot{\varepsilon}_{ij}^{p} = \frac{\dot{\lambda}\partial\phi}{\partial\Sigma_{ij}} = \frac{\dot{\lambda}\partial\phi}{\partial\sigma_{mn}} L_{mnkl} K_{klij} \tag{2.13}$$

where $\dot{\varepsilon}_{ij}^{p}$ is the rate tensor plastic strain components and $\dot{\lambda}$ is a positive scalar called the plastic multiplier.

Let (x, y, z) be the reference directions associated with the orthotropy. In the case of a sheet material, x, y, and z represent the rolling direction, the long transverse direction, and the normal direction (through-thickness direction), respectively. Relative to the orthotropy axes the transformed stress tensor Σ (in vector form) can be expressed in terms of the Cauchy stress tensor according to

$$\begin{bmatrix}\Sigma_{xx}\\ \Sigma_{yy}\\ \Sigma_{zz}\\ \Sigma_{xy}\\ \Sigma_{yz}\\ \Sigma_{xz}\end{bmatrix}=\begin{bmatrix} L_{11} & L_{12} & L_{13} & & & \\ L_{12} & L_{22} & L_{23} & & & \\ L_{13} & L_{23} & L_{33} & & & \\ & & & L_{44} & & \\ & & & & L_{55} & \\ & & & & & L_{66}\end{bmatrix}\begin{bmatrix} \frac{2}{3} & -\frac{1}{3} & -\frac{1}{3} & & & \\ -\frac{1}{3} & \frac{2}{3} & -\frac{1}{3} & & & \\ -\frac{1}{3} & -\frac{1}{3} & \frac{2}{3} & & & \\ & & & 1 & & \\ & & & & 1 & \\ & & & & & 1\end{bmatrix}\begin{bmatrix}\sigma_{xx}\\ \sigma_{yy}\\ \sigma_{zz}\\ \sigma_{xy}\\ \sigma_{yz}\\ \sigma_{xz}\end{bmatrix} \quad (2.14)$$

or

$$\begin{bmatrix}\Sigma_{xx}\\ \Sigma_{yy}\\ \Sigma_{zz}\\ \Sigma_{xy}\\ \Sigma_{yz}\\ \Sigma_{xz}\end{bmatrix}=\begin{bmatrix} \theta_1 & \phi_1 & \Omega_1 & & & \\ \theta_2 & \phi_2 & \Omega_2 & & & \\ \theta_3 & \phi_3 & \Omega_3 & & & \\ & & & L_{44} & & \\ & & & & L_{55} & \\ & & & & & L_{66}\end{bmatrix}\begin{bmatrix}\sigma_{xx}\\ \sigma_{yy}\\ \sigma_{zz}\\ \sigma_{xy}\\ \sigma_{yz}\\ \sigma_{xz}\end{bmatrix} \quad (2.15)$$

where

$$\begin{aligned}\theta_1 &= \tfrac{2}{3}L_{11}-\tfrac{1}{3}L_{12}-\tfrac{1}{3}L_{13},\ \phi_1=\tfrac{2}{3}L_{12}-\tfrac{1}{3}L_{11}-\tfrac{1}{3}L_{13},\ \Omega_1=\tfrac{2}{3}L_{13}-\tfrac{1}{3}L_{11}-\tfrac{1}{3}L_{12}\\ \theta_2 &= \tfrac{2}{3}L_{12}-\tfrac{1}{3}L_{22}-\tfrac{1}{3}L_{23},\ \phi_2=\tfrac{2}{3}L_{22}-\tfrac{1}{3}L_{12}-\tfrac{1}{3}L_{23},\ \Omega_2=\tfrac{2}{3}L_{23}-\tfrac{1}{3}L_{12}-\tfrac{1}{3}L_{22}\\ \theta_3 &= \tfrac{2}{3}L_{13}-\tfrac{1}{3}L_{23}-\tfrac{1}{3}L_{33},\ \phi_3=\tfrac{2}{3}L_{23}-\tfrac{1}{3}L_{13}-\tfrac{1}{3}L_{33},\ \Omega_3=\tfrac{2}{3}L_{33}-\tfrac{1}{3}L_{13}-\tfrac{1}{3}L_{23}\end{aligned} \quad (2.16)$$

It is easy to observe that the following relationships exist

$$\begin{aligned}\Omega_1 &= -(\theta_1+\phi_1)\\ \Omega_2 &= -(\theta_2+\phi_2)\\ \Omega_3 &= -(\theta_3+\phi_3)\end{aligned} \quad (2.17)$$

Due to its complex nature, anisotropic material model such as above often requires the calibration of numerous material parameter through several sets of tension, compression, and torsion specimens. Though careful calibration, the anisotropic feature of material can then be described. For example, a set of anisotropic material parameters listed in Table2.1 is adopted from Stewart and Cazacu (2011) used to represent transversely

isotropic materials for which the matrix has a weaker in-plane yield strength than through-thickness yield strength.

Table 2.1 Adopted Anisotropy and strength differential coefficients

k	L_{11}	L_{12}	L_{13}	L_{22}	L_{23}	L_{33}	L_{44}	L_{55}	L_{66}
0	1.054	-0.129	0.075	1.054	0.075	0.85	0.775	1.0	1.0

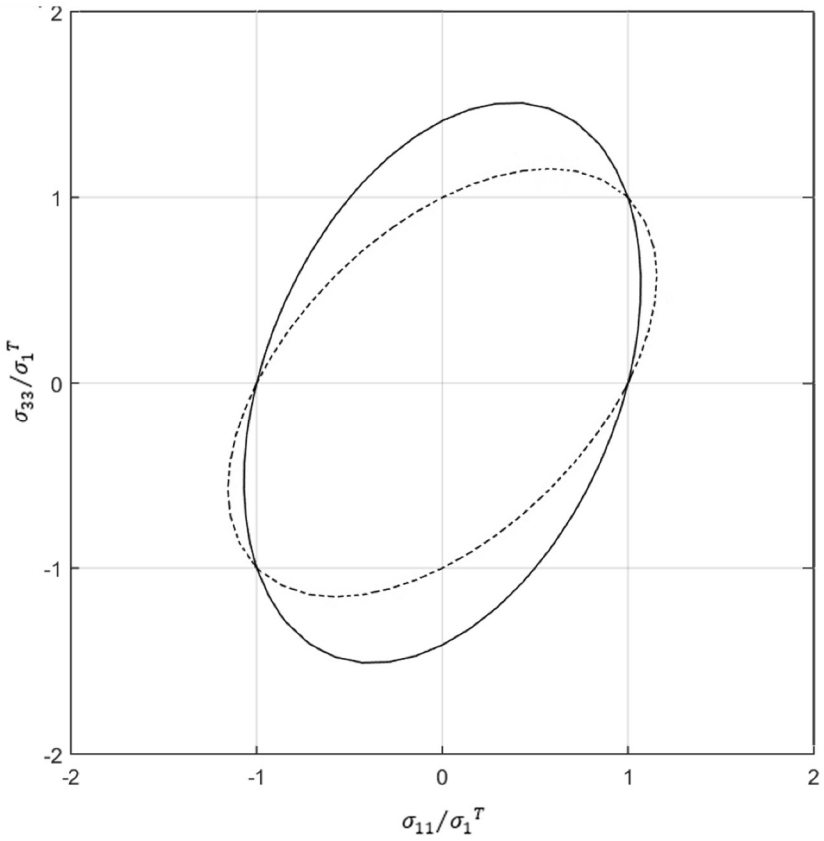

Figure 2.2 Plane stress yield locus comparison between Anisotropic and Von Mises Material

Fig. 2.2 shows the plane stress yield locus according to the above parameters. X is the in-plane direction with Z being the through-thickness direction. Compare to the Von Mises yield locus as shown by the dotted line, it's obvious the yield stress of the anisotropic material is different between in-plane direction and normal direction and is different from Von Mises loci at stress states in between. The material parameter k here is set as 0, but if calibrated with negative or positive values, the material is expected to further show tension-compression asymmetry. Furthermore, when calibration for real material, it's often that the material hardening in various directions will not follow the hardening of uniaxial tensile loading at various stage of equivalent plastic strain. The material parameters can then be mapped between yield locus calibrated from different strain level to capture this complex behavior. An example of the calibration of this model further coupled with damage parameters including volumetric damage and shear damage will be given in Chapter VI.

CHAPTER III

INVESTIGATION OF THE MICROMECHANICS OF DUCTILE DAMAGE MODEL THROUGH UNIT CELL MODEL

3.1 Introduction

The ductile fracture process in metals is strongly influenced by the stress state subjected by the material. In these materials, voids nucleated at inclusions and second-phase particles by decohesion of the particle matrix interface or by particle cracking (van Stone et al., 1985; Garrison and Moody, 1987). Under high triaxial stress states, voids grow in size, followed by inter-void flow localization, leading to fracture initiation (Benzerga and Leblond, 2010). On the other hand, under shear-dominated loading, voids change little in size but significantly in shape and orientation, and the onset of material fracture takes place after strain localization in a narrow band (Tvergaard, 2008, 2009; Nielsen et al., 2012).

There is a long history of experimental and modeling efforts to predict ductile fracture. The experimental work by Bridgman (1952) showed that the strain to failure increased significantly when the tensile test was carried out in a pressurized environment. Using notched tensile specimens, Hancock and Mackenzie (1976) and Hancock and Brown (1983) demonstrated that the strain to initiate ductile fracture decreases with the stress triaxiality. In the widely used Johnson-Cook fracture model (Johnson and Cook, 1985), the dependence of the failure strain on the stress triaxiality is described by an exponentially decaying function. More recently, Bao and Wierzbicki (2004), Barsoum and Faleskog

(2007), Gao et al. (2010) and Zhou et al. (2012) showed that the strain to failure not only depends on the stress triaxiality but also depends on the Lode parameter.

Early micromechanical treatment of ductile fracture considered growth of isolated voids in solids (McClintock, 1968; Rice and Tracey, 1969). Gurson (1977) proposed a homogenized yield surface for void containing materials based on the maximum plastic work principle. The Gurson model, with further development by Tvergaard and Needleman (Tvergaard, 1981, 1982; Tvergaard and Needleman, 1984), has been widely used in modeling of ductile fracture. In the Gurson-Tvergaard-Needleman (GTN) model, damage evolution is completely due to the increase of void volume fraction, which is strongly influenced by the stress triaxiality, and the final void coalescence stage is approximated by artificially accelerating the void growth rate. More recent modifications to the Gurson-type porous material models include the work by Nahshon and Hutchinson (2008), Xue (2008), Zhou et al. (2014), Malcher et al. (2014), Zhai et al. (2016), among others to take into account shear-induced damage.

Although experiments can reveal the macroscopics of ductile fracture process, monitoring the stress state evolution on the microscale and obtaining reliable fracture strain still remain challenging. Micromechanical finite element analysis, however, provides a viable alternative. Typically, detailed finite element analyses are conducted for an RMV, often referred to as the unit cell analysis, under various stress states to study the void growth and coalescence process. Koplik and Needleman (1988) conducted axisymmetric unit cell analyses to calibrate the micromechanical parameters in the GTN model and showed that the onset of void coalescence by internal necking can be identified by a shift of the deformation to a macroscopic uniaxial strain state. Faleskog et al. (1998) conducted a series

of unit cell analyses and showed that the q-parameters in the GTN model depend on the material flow properties. Kim et al. (2004) and Gao and Kim (2006) showed that the void growth and coalescence process and the resulting macroscopic behavior of the RMV are not only influenced by the stress triaxiality but also influenced by the Lode parameter. It is worth mentioning that in these analyses, only normal stress components were imposed on the unit cell and the deformed boundaries remained parallel to the undeformed boundaries. Barsoum and Faleskog (2007) proposed a unit cell model to simulate a thin-walled, double notched tube subjected to combined tension and torsion loading. Proportional stresses including a shear stress component were applied on the unit cell's periodic boundaries. The failure criterion was based on the theoretical framework of plastic localization into a band by Rice (1977). Following the work by Needleman and Tvergaard (1992), the localization criterion was defined as when the ratio between the norm of the deformation gradient rates inside and outside the band, denoted as η, becomes sufficiently large. In their later work, Barsoum and Faleskog (2011) suggested that the critical η-value should be chosen as 10. However, they also stated that this criterion cannot be used as an indicator for material failure under high stress triaxialities when the Lode parameter is close to zero. Tvergaard (2008, 2009, 2012) conducted a series of plane strain analyses to study the behavior of cylindrical voids in a shear-field. Using the same unit cell model and failure criterion as Barsoum and Faleskog (2007, 2011), Dunand and Mohr (2014) conducted extensive numerical analyses to demonstrate that the macroscopic equivalent plastic strain for material failure after monotonic proportional loading decreases with stress triaxiality and is a convex, non-symmetric function of the Lode parameter. In Dunand and Mohr (2014), the critical η-value was chosen to be 5. The arbitrariness in selection of the critical η-value

is largely due to the difficulty in defining η at the unit cell level, which motivated a recent study by Wong and Guo (2015) to propose an energy-based method to establish the criterion for onset of void coalescence. The idea supporting this method comes from the observation that as failure by void coalescence takes place in a band, and material outside this band undergoes elastic loading. Elastic unloading is said to have occurred when the overall elastic work rate of the unit cell becomes negative and void coalescence happens when the ratio of the overall elastic and plastic work rates reaches a minimum. However, local unloading may cause the computed overall elastic work rate to become negative. Moreover, void coalescence is due to the competition between the reduction of the ligament between voids and the strain hardening of the ligament material. Since the elastic and plastic work rates of the ligament are included in computing the overall work rates, non-negligible errors in failure prediction may occur for some cases.

From the above literature review, a few points can be made about the unit cell analysis. Firstly, with an assumed periodic void distribution, a material unit can be modeled with detailed finite elements subjected to various stress states. The purpose of the unit cell analysis is to study the deformation and void behavior and to establish a failure criterion in terms of the homogenized, macroscopic quantities at the material unit level. Secondly, failure occurs in a localized band and material outside of this band undergoes elastic recovery. The change of deformation mode outside the localization band gives an indication of fracture initiation. Thirdly, if identical deformation is enforced for all material units, a localized failure band will not appear. In many of the previous studies, all material units were assumed to be the same and subjected to the same deformation, thus the unit

cell only included one material unit. Consequently, unrealistic predictions were made under certain conditions.

In this chapter, a numerical model is proposed, in which the unit cell consists of a material unit, where fracture initiates, and two adjacent material units outside the localization band. A material failure criterion is established by detecting the occurrence of elastic unloading outside the localization band. Section 3.2 provides a detailed description of the proposed unit cell model, including how to impose the boundary conditions and how to establish the failure criterion. Section 3.3 presents and discusses numerical results under various scenarios. The effects of the stress state on void behavior and ductile fracture initiation are discussed. For comparison, analyses are also conducted using the methods proposed by Barsoum and Faleskog (2007, 2011) and Wong and Guo (2015). It is shown that the present model leads to improved predictions. Finally, some concluding remarks are made in Section 3.4.

3.2 Problem formulation

3.2.1 Characterization of the macroscopic stress state of the RMV

Let Σ_{ij} be the macroscopic Cauchy stress tensor and S_{ij} be the stress deviator, $S_{ij} = \Sigma_{ij} - \Sigma_m\delta_{ij}$, where δ_{ij} denotes the Kronecker Delta, Σ_m represents the mean stress, $\Sigma_m = \Sigma_{ii}/3$, and the summation convention is adopted for repeated indices. The von Mises equivalent macroscopic stress is defined as

$$\Sigma_e = \sqrt{3J_2} = \sqrt{\frac{3}{2}S_{ij}S_{ij}}\ . \tag{3.1}$$

The stress triaxiality is defined as the ratio between mean stress and von Mises equivalent stress

$$T = \frac{\Sigma_m}{\Sigma_e}. \tag{3.2}$$

The Lode parameter is used to distinguish different deviatoric stress states and is defined as

$$\mu = \sqrt{3}\tan\left(\theta - \tfrac{\pi}{6}\right), \tag{3.3}$$

where θ denotes the Lode angle, with $\cos(3\theta) = \frac{27J_3}{2\sigma_e^3}$ and $J_3 = \frac{S_{ij}S_{jk}S_{ki}}{3}$.

3.2.2 Micromechanics of ductile fracture

Fig. 3.1 illustrates the mechanisms of ductile fracture schematically. Voids nucleate from inclusions at a relatively low stress level and then grow to larger sizes under increased strain of the triaxial loading, or elongate/rotate under shear-dominated loading. Assuming a periodic distribution of voids, the material can be considered as comprised of a number of void-containing RMVs. However, the void growth or void-shearing behavior in all RMVs is not uniform. As strain continuingly increases, the void having larger initial size or under more favorable condition grows or deforms faster than others so that large plastic flow is localized around it, resulting in numerous micro-cavities being nucleated from the nearby particles. Eventually this void wins and the RMV fractures. Therefore, the fracture process is confined in a layer of RMVs. After the RMV fractures, other RMVs in adjacent layers undergo elastic recovery and do not rupture.

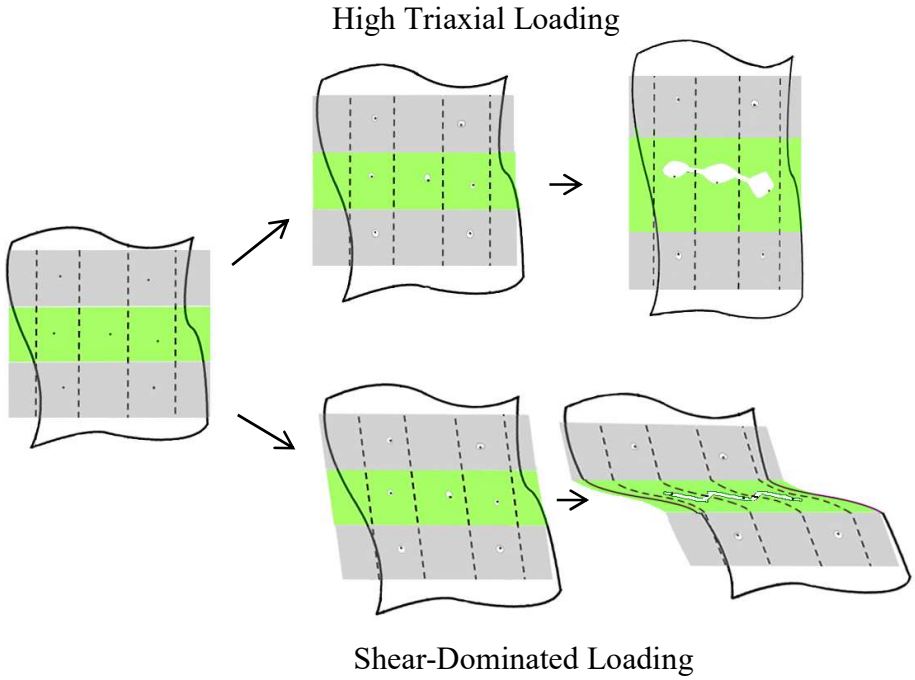

Figure 3.1. Schematic illustration of the ductile fracture by void growth followed by internal necking or by void shearing and strain localization

3.2.3 A unit cell model

The fracture mechanisms described above lead to a simple numerical approach to study the fracture process. Fig. 3.2 shows a piece of material containing three layers of material units subjected a set of normal and shear stress components. Because of periodic symmetry, a unit cell can be defined to include three material units, Fig. 3.3(a). Fig. 3.3(b) shows the dimensions of the material unit, $2D_0 \times 2D_0 \times 2D_0$. The present unit cell is different from the ones used in many previous studies where a single material unit was considered. If the unit cell were to consist of a single material unit, it would imply that all material units are identical and experience the same deformation, and thus failure would not localize in one layer of material. Furthermore, using three material units in the unit cell enables a simple method to identify fracture initiation. When a material unit fractures, the

material units above and below it in adjacent layers undergo elastic unloading. By monitoring the stress-strain behavior of the adjacent material units above or below it, one can determine if fracture has taken place. Ductile fracture can be due to void growth and coalescence or localized plastic strain or the combined effect of them. Tekoğlu et al. (2015) analyzed the competition between these failure mechanisms. As will be shown in next section, the unit cell model and the method to determine the onset of fracture proposed in this study not only are easy to implement in finite element analysis but also offer many advantages comparing to previous models.

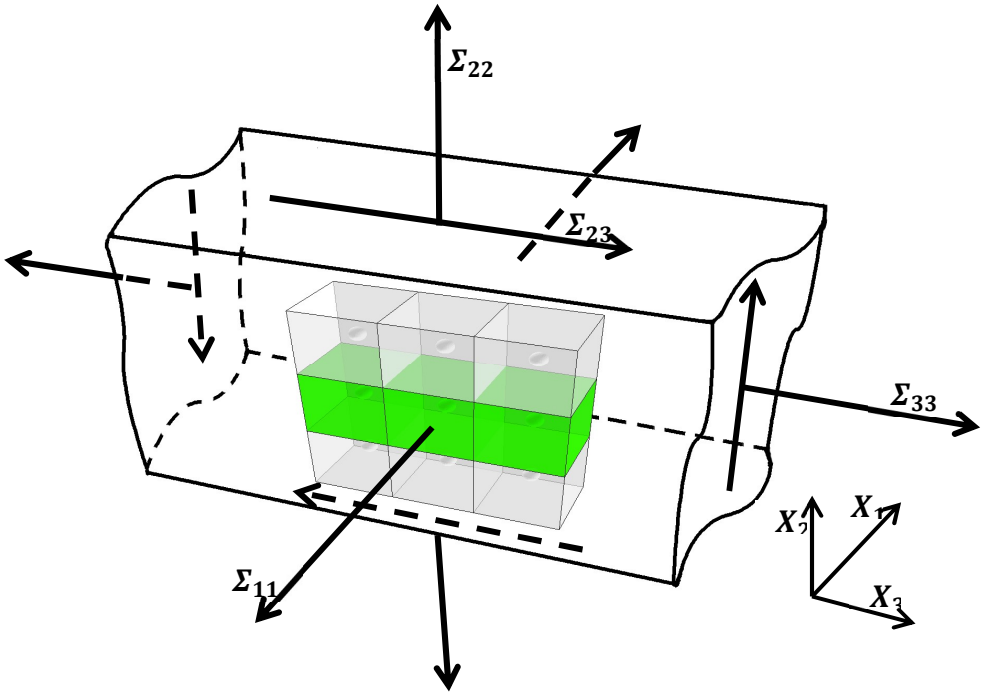

Figure 3.2. The micromechanical model of a material comprised of layers of void containing material units subjected to macroscopic stress components

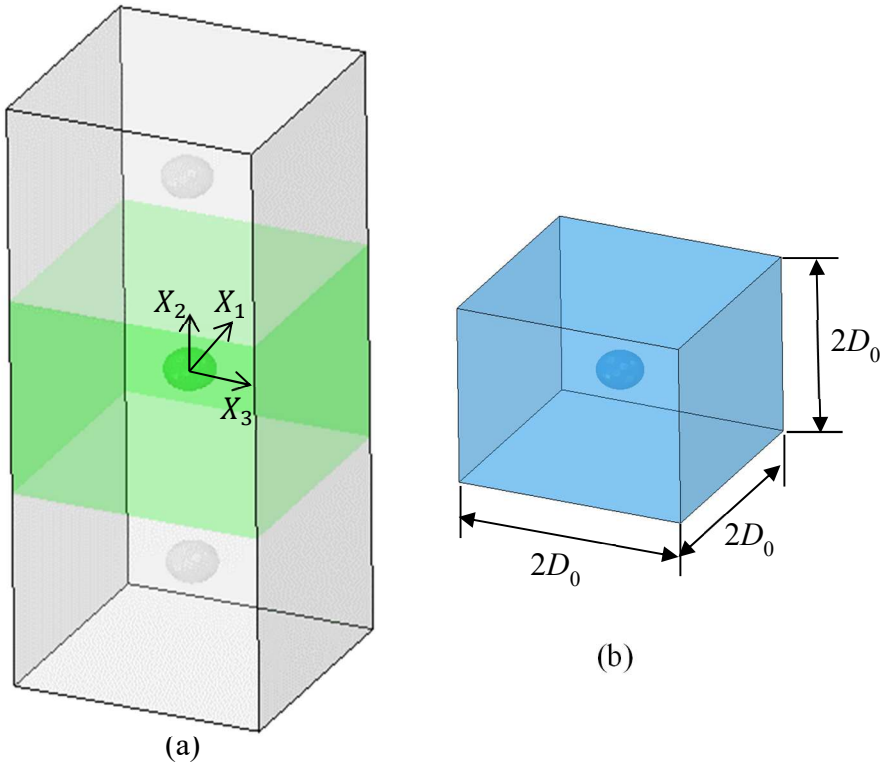

Figure 3.3. (a) A unit cell consisting of three void-containing material units, (b) a material unit

To study the behavior of the unit cell under various stress states, the stresses imposed on the unit cell should include both normal and shear components. Here the applied stress consists of three normal stress components and a shear stress component, the same as in Barsoum and Faleskog (2007), Dunand and Mohr (2014), and Wong and Guo (2015). As will be shown in Section 3.3.1, depending on the stress state, localization can occur in different planes. For example, localization occurs in the layer of material units in the X_1-X_3 plane as μ = -1 or in the layer of material units in the X_1-X_2 plane as μ = 1. The

three material units in the unit cell should be stacked in the direction normal to the localization plane to let localization take place in the middle material unit.

Fig. 3.4 displays a typical ½-symmetric finite element mesh of the sandwiched unit cell shown in Fig. 3.3, where the three material units are stacked along the X_2-direction. The initial dimensions of the half unit cell are then given by $D_1 = D_0$ along X_1-axis, $D_2 = 6D_0$ along X_2-axis and $D_3 = 2D_0$ along X_3-axis. Among the three material units, the middle one will experience localized failure while the other two will undergo elastic recovery. Each material unit contains a spherical void at its center. A slightly larger initial void is placed in the middle material unit to ensure localization occurs in this unit. Here the initial void radius is $R_1 = 0.2D_0$ in the middle material unit and $R_2 = 0.198D_0$ in the other two material units. This corresponds to an initial void volume fraction of 0.004188 in the middle material unit. Mesh difference between the middle material unit and the outside material units are carefully controlled as small as possible so that the mesh-introduced inhomogeneity is minimal. With this setup, the overall behavior of the three material units are virtually the same prior to the occurrence of localization in the middle unit, and the model captures the interaction among neighboring voids as well. The mesh consists of 27,000 hybrid, 8-node hexahedral elements.

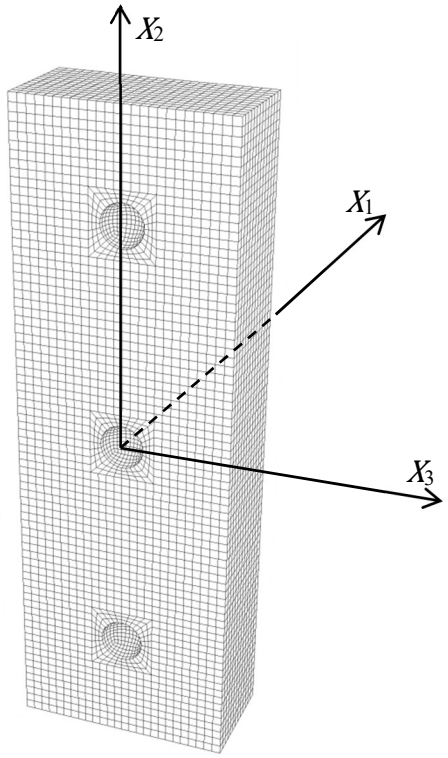

Figure 3.4. A typical finite element mesh for one half of the sandwiched unit cell

3.2.4 Boundary condition

Since the stress state is characterized by three normal components, Σ_{11}, Σ_{22} and Σ_{33}, and one shear component, Σ_{23}, for proportional loading, the macroscopic deformation gradient will take the form of

$$\boldsymbol{F} = \begin{bmatrix} F_{11} & 0 & 0 \\ 0 & F_{22} & 0 \\ 0 & F_{23} & F_{33} \end{bmatrix}. \tag{3.4}$$

Periodic boundary conditions are imposed on the $X_2 = \pm\frac{D_2}{2}$ and $X_3 = \pm\frac{D_3}{2}$ surfaces. If the applied shear stress component is nonzero, these surfaces will not remain straight after deformation. Symmetry allows to model one half of the unit cell and the

symmetry condition is imposed on $X_1 = 0$. On $X_1 = D_1$, homogenous conditions are applied, indicating surfaces normal to the X_1 direction will remain planar and parallel because the shear loading is only applied on the X_2-X_3 plane. Four displacement measures δ_i (i = 1, 2, 3, 4) are introduced to describe the boundary conditions as follows

$$\begin{aligned} &\text{On } X_1 = 0: \quad u_1 = 0, \\ &\text{On } X_1 = D_1: \quad u_1 = \delta_1, \end{aligned} \tag{3.5}$$

$$\begin{aligned} \text{On } X_2 = \pm\tfrac{D_2}{2}: \; & u_1\left(X_1, \tfrac{D_2}{2}, X_3\right) = u_1\left(X_1, -\tfrac{D_2}{2}, X_3\right), \\ & u_2\left(X_1, \tfrac{D_2}{2}, X_3\right) = u_2\left(X_1, -\tfrac{D_2}{2}, X_3\right) + \tfrac{D_2}{D_0}\delta_2, \\ & u_3\left(X_1, \tfrac{D_2}{2}, X_3\right) = u_3\left(X_1, -\tfrac{D_2}{2}, X_3\right) + \tfrac{D_2}{D_0}\delta_4, \end{aligned} \tag{3.6}$$

$$\begin{aligned} \text{On } X_3 = \pm\tfrac{D_3}{2}: \; & u_1\left(X_1, X_2, \tfrac{D_3}{2}\right) = u_1\left(X_1, X_2, -\tfrac{D_3}{2}\right), \\ & u_2\left(X_1, X_2, \tfrac{D_3}{2}\right) = u_2\left(X_1, X_2, -\tfrac{D_3}{2}\right), \\ & u_3\left(X_1, X_2, \tfrac{D_3}{2}\right) = u_3\left(X_1, X_2, -\tfrac{D_3}{2}\right) + \tfrac{D_3}{D_0}\delta_3. \end{aligned} \tag{3.7}$$

3.2.5 Displacement-controlled loading

To study the effect of stress state on the response of the unit cell, a proportional loading approach is applied such that the macroscopic stress triaxiality and Lode parameter of the unit cell remain constant during the entire loading history. This can be done by keeping the ratios between the applied macroscopic stress components constant

$$\psi_1 = \frac{\Sigma_{11}}{\Sigma_{22}}, \quad \psi_2 = \frac{\Sigma_{33}}{\Sigma_{22}}, \quad \psi_3 = \frac{\Sigma_{23}}{\Sigma_{22}}. \tag{3.8}$$

The finite element simulations are under displacement control. The approach proposed and described in Barsoum and Faleskog (2007) and Wong and Guo (2015) are used to apply the displacement-controlled loading. By taking the volume average of the local deformation gradient, the macroscopic deformation gradient can be given by the following expression

$$\overline{\boldsymbol{F}} = \frac{1}{V_0}\int_{S_0} \boldsymbol{x}\otimes\boldsymbol{N}\mathrm{d}S_0 \ . \tag{3.9}$$

where V_0 is the volume of the unit cell in the undeformed configuration, S_0 is the outer surface with the outward normal $\boldsymbol{N}$, and $\boldsymbol{x}$ denotes the current position of a point on the deformed surface. Utilizing the boundary conditions described by Eqs. (3.5-3.7), $\overline{\boldsymbol{F}}$ can be expressed as

$$\overline{\boldsymbol{F}} = \begin{bmatrix} \frac{D_0+\delta_1}{D_0} & 0 & 0 \\ 0 & \frac{D_0+\delta_2}{D_0} & 0 \\ 0 & \frac{\delta_4}{D_0} & \frac{D_0+\delta_3}{D_0} \end{bmatrix}. \tag{3.10}$$

Therefore, the velocity gradient can be expressed as

$$\boldsymbol{L} = \dot{\overline{\boldsymbol{F}}}\overline{\boldsymbol{F}}^{-1} = \begin{bmatrix} \frac{\dot{\delta_1}}{D_0+\delta_1} & 0 & 0 \\ 0 & \frac{\dot{\delta_2}}{D_0+\delta_2} & 0 \\ 0 & \frac{\dot{\delta_4}}{D_0+\delta_2} - \frac{\delta_4}{D_0+\delta_2}\frac{\dot{\delta_3}}{D_0+\delta_3} & \frac{\dot{\delta_3}}{D_0+\delta_3} \end{bmatrix}, \tag{3.11}$$

and the rate of deformation tensor can be calculated by

$$\boldsymbol{D} = \frac{\boldsymbol{L}+\boldsymbol{L}^T}{2}. \tag{3.12}$$

Consequently, the total work rate can be expressed as

$$\dot{W} = V\boldsymbol{\Sigma}_{ij}\boldsymbol{D}_{ij} = \widehat{\mathbf{D}}^T\,\widehat{\boldsymbol{\Sigma}}, \tag{3.13}$$

where V is the current volume of the unit cell including the void, vectors $\widehat{\mathbf{D}}$ and $\widehat{\mathbf{\Sigma}}$ are generalized displacement rate and generalized force vectors respectively, defined as

$$\widehat{\boldsymbol{\Sigma}} = \begin{bmatrix} V\Sigma_{11} \\ V\Sigma_{22} \\ V\Sigma_{33} \\ V\Sigma_{23} \end{bmatrix} \quad \widehat{\boldsymbol{D}} = \begin{bmatrix} D_{11} \\ D_{22} \\ D_{33} \\ 2D_{23} \end{bmatrix} = \boldsymbol{Q}\dot{\boldsymbol{\delta}}, \tag{3.14}$$

with

$$\boldsymbol{Q} = \begin{bmatrix} \frac{1}{D_0+\delta_1} & 0 & 0 & 0 \\ 0 & \frac{1}{D_0+\delta_2} & 0 & 0 \\ 0 & 0 & \frac{1}{D_0+\delta_3} & 0 \\ 0 & 0 & -\frac{\delta_4}{(D_0+\delta_2)(D_0+\delta_3)} & \frac{1}{D_0+\delta_2} \end{bmatrix}. \tag{3.15}$$

Next, consider an orthogonal transformation

$$\widehat{\mathbf{\Sigma}} = \boldsymbol{CP} \text{ and } \widehat{\mathbf{D}} = \boldsymbol{C}\dot{\boldsymbol{q}} \tag{3.16}$$

such that $\boldsymbol{P} = (P_1, 0, 0, 0)^T$. A 4×4 orthogonal matrix can be constructed as

$$\boldsymbol{C} = \begin{bmatrix} a_1 & a_2/\sqrt{A_{12}} & a_1a_3/\sqrt{A_{12}A_{123}} & a_1a_4/\sqrt{A_{123}A_{1234}} \\ a_2 & -a_1/\sqrt{A_{12}} & a_2a_3/\sqrt{A_{12}A_{123}} & a_2a_4/\sqrt{A_{123}A_{1234}} \\ a_3 & 0 & -A_{12}/\sqrt{A_{12}A_{123}} & a_3a_4/\sqrt{A_{123}A_{1234}} \\ a_4 & 0 & 0 & -A_{123}/\sqrt{A_{123}A_{1234}} \end{bmatrix}, \tag{3.17}$$

where

$$\begin{aligned} {a_1}^2 + {a_2}^2 + \cdots + {a_4}^2 &= 1, \\ A_{1\cdots n} = {a_1}^2 + \cdots + {a_n}^2 &\text{ where } 2 \le \mathrm{n} \le 4. \end{aligned} \tag{3.18}$$

Here, a 4×4 $\boldsymbol{C}$ matrix is needed and a_i's are defined as follows

$$a_1 = \frac{\psi_1}{\psi_0}, \quad a_2 = \frac{1}{\psi_0}, \quad a_3 = \frac{\psi_2}{\psi_0}, \quad a_4 = \frac{\psi_3}{\psi_0}, \tag{3.19}$$

where $\psi_0 = \sqrt{1 + {\psi_1}^2 + {\psi_2}^2 + {\psi_3}^2}$. After the orthogonal transformation, the total work rate can be expressed as

$$\dot{W} = \dot{\boldsymbol{q}}^{\boldsymbol{T}}\boldsymbol{P}, \tag{3.20}$$

meaning $\boldsymbol{P}$ and $\dot{\boldsymbol{q}}$ are work conjugate. From Eqs. (3.14-3.16), the values of δ_i used to describe the displacement boundary conditions are controlled by

$$\dot{\boldsymbol{\delta}} = \boldsymbol{Q}^{-1}\boldsymbol{C}\dot{\boldsymbol{q}}. \tag{3.21}$$

By prescribing $\dot{q}_1$and setting $P_2 = P_3 = P_4 = 0$, constant values of ψ_i's can be maintained during the loading history. This procedure is implemented in ABAQUS (2013) by using the MPC user subroutine.

As demonstrated by Wong and Guo (2015), different choices of ψ_i's can result in the same values of T and μ. To compare the results with Barsoum and Faleskog (2007, 2011) and Wong and Guo (2015), this paper only presents the analyses for the $\psi_1 = \psi_2$ case. Let $\rho_n = \psi_1 = \psi_2$ and $\rho_s = \psi_3$, T and μ can be expressed as

$$T = \frac{(1+2p_n)\cdot sign(\Sigma_{22})}{3\sqrt{(1-p_n)^2+3{p_s}^2}}, \qquad \mu = -\frac{(1-p_n)\cdot sign(\Sigma_{22})}{\sqrt{3[(1-p_n)^2+4{p_s}^2]}}. \tag{3.22}$$

For given values of T and μ, Barsoum and Faleskog (2007, 2011) showed that solutions of $\rho_n$and $\rho_s$can be given as

$$\rho_n = \frac{3T\sqrt{3+\mu^2}+2\mu}{3T\sqrt{3+\mu^2}-4\mu}, \qquad \rho_s = \frac{3\sqrt{1-\mu^2}}{3T\sqrt{3+\mu^2}-4\mu}, \tag{3.23}$$

which are valid for $\Sigma_{22} \neq 0$ and $T \gtrless \frac{4\mu}{3\sqrt{3+\mu^2}}$.

The equations described above to prescribe the displacement-controlled loading are derived for the case where localization is to occur in the X_1-X_3 plane. Barsoum and Faleskog (2011) showed that, in general, localization may take place in a plane oriented at an angle θ from the X_1-X_3 plane, which can be accounted for by rotating the Cartesian coordinate system by θ about the X_1-axis. The stress components in the new coordinate system can be expressed in terms of the specified values of ρ_n and ρ_s as

$$\frac{\Sigma'_{11}}{\Sigma'_{22}} = \frac{\rho_n}{\sin^2\theta\rho_n + \cos^2\theta - 2\sin\theta\cos\theta\rho_s}, \tag{3.24}$$

$$\frac{\Sigma'_{33}}{\Sigma'_{22}} = \frac{\sin^2\theta + \cos^2\theta\rho_n + 2\sin\theta\cos\theta\rho_s}{\sin^2\theta\rho_n + \cos^2\theta - 2\sin\theta\cos\theta\rho_s}, \tag{3.25}$$

$$\frac{\Sigma'_{23}}{\Sigma'_{22}} = \frac{\sin\theta\cos\theta(\rho_n - 1) + \cos 2\theta\rho_s}{\sin^2\theta\rho_n + \cos^2\theta - 2\sin\theta\cos\theta\rho_s}. \tag{3.26}$$

With this coordinate transformation, the equations described above can be used for cases where localization takes place in a plane oriented at an angle θ from the X_1-X_3 plane.

It is worth noting that variation of the stress state is inevitable in actual fracture specimens or structural components. We refer to a number of recent studies regarding the effect of non-proportional loading path. For examples, Basu and Benzerga (2015) and Thomas et al. (2016) investigated the effect of different non-proportional loading paths on failure strain, while Papasidero et al. (2015) made efforts to determine the actual loading path of Bao and Wierzbicki's well-known experiments (2004). It is possible to modify the displacement-controlled applied load to reflect the change of stress state provided the loading path is specified.

3.2.6 Macroscopic effective strain measure

Eq. (3.9) can be used to evaluate the macroscopic deformation gradient of a material unit. Since the surface surrounding the material unit consists of six square faces, the total surface integral can be obtained by summing the six surface integrals on the six faces. For the material unit shown in Fig. 3.3(b), the integrals over faces $X_1 = \pm D_0$ and $X_3 = \pm D_0$ can be easily evaluated using the boundary conditions imposed on these faces as described in Eqs. (3.5) and (3.7),

$$\frac{1}{V_0}\int_{X_1=D_0}(\boldsymbol{x}^{\pm}-\boldsymbol{x}^{-})\otimes\boldsymbol{E_1}\mathrm{d}S_0 = \begin{bmatrix} \frac{D_0+\delta_1}{D_0} & 0 & 0 \\ 0 & 0 & 0 \\ 0 & 0 & 0 \end{bmatrix}, \tag{3.27}$$

$$\frac{1}{V_0}\int_{X_3=D_0}(\boldsymbol{x}^{\pm}-\boldsymbol{x}^{-})\otimes\boldsymbol{E_3}\mathrm{d}S_0 = \begin{bmatrix} 0 & 0 & 0 \\ 0 & 0 & 0 \\ 0 & 0 & \frac{D_0+\delta_3}{D_0} \end{bmatrix}, \tag{3.28}$$

where $\boldsymbol{E}_1$ and $\boldsymbol{E}_3$ are unit vectors in X_1 and X_3 directions respectively. Since one or both of the remaining faces, $X_2 = X_2^*$ and $X_2 = X_2^* - 2D_0$, are inside the unit cell, Fig. 3.3(a), contributions from these two surface integrals should be evaluated by

$$\begin{aligned} &\frac{1}{V_0}\int_{X_2=X_2^*}\boldsymbol{x}\otimes\boldsymbol{E_2}\mathrm{d}S_0 - \frac{1}{V_0}\int_{X_2=X_2^*-2D_0}\boldsymbol{x}\otimes\boldsymbol{E_2}\mathrm{d}S_0 \\ =&\frac{1}{V_0}\int_{X_2=X_2^*}\left[\begin{pmatrix} 0 \\ 2D_0 \\ 0 \end{pmatrix}+\boldsymbol{u}\right]\otimes\boldsymbol{E_2}\mathrm{d}S_0 - \frac{1}{V_0}\int_{X_2=X_2^*-2D_0}\left[\begin{pmatrix} 0 \\ 2D_0 \\ 0 \end{pmatrix}+\boldsymbol{u}\right]\otimes\boldsymbol{E_2}\mathrm{d}S_0 \\ =&\begin{bmatrix} 0 & 0 & 0 \\ 0 & \frac{D_0+\bar{\delta}_2}{D_0} & 0 \\ 0 & \frac{\bar{\delta}_4}{D_0} & 0 \end{bmatrix}, \end{aligned} \tag{3.29}$$

where $\boldsymbol{E}_2$ is the unit vector in X_2-direction, $\boldsymbol{u}$ is the displacement vectors on the evaluated surface respectively, $\bar{\delta}_2 = \int_{X_2=X_2^*} u_2 \mathrm{d}S_0 - \int_{X_2=X_2^*-2D_0} u_2 \mathrm{d}S_0$ and $\bar{\delta}_4 = \int_{X_2=X_2^*} u_3 \mathrm{d}S_0 - \int_{X_2=X_2^*-2D_0} u_3 \mathrm{d}S_0$, $X_2^* = 3D_0$ for the top material unit, and $X_2^* = D_0$ for the middle material unit. Because the model is symmetric about the X_2-X_3 plane, $\int_{X_2=X_2^*} u_1 \mathrm{d}S_0 - \int_{X_2=X_2^*-2D_0} u_1 \mathrm{d}S_0 = 0$. Therefore, the macroscopic deformation gradient of a material unit is

$$\overline{\boldsymbol{F}} = \begin{bmatrix} \frac{D_0+\delta_1}{D_0} & 0 & 0 \\ 0 & \frac{D_0+\bar{\delta}_2}{D_0} & 0 \\ 0 & \frac{\bar{\delta}_4}{D_0} & \frac{D_0+\delta_3}{D_0} \end{bmatrix}, \tag{3.30}$$

For non-singular deformation gradient $\boldsymbol{F}$, polar decomposition can be performed

$$\boldsymbol{F} = \boldsymbol{RU} = \boldsymbol{VR}, \tag{3.31}$$

where $\boldsymbol{R}$ is an orthogonal rotation tensor, and $\boldsymbol{U}$ and $\boldsymbol{V}$ are symmetric stretch tensors. The left Cauchy-Green deformation tensor is defined as

$$\boldsymbol{B}^{-1} = (\boldsymbol{F}^{-1})^T \boldsymbol{F}^{-1} = (\boldsymbol{V}^{-1})^T \boldsymbol{V}^{-1} = (\boldsymbol{V}^{-1})^2. \tag{3.32}$$

The true strain can now be written in terms of $\boldsymbol{V}$ as

$$\boldsymbol{\varepsilon} = -\frac{1}{2}\ln \boldsymbol{B}^{-1} = -\frac{1}{2}\ln(\boldsymbol{V}^{-1})^2 = \ln \boldsymbol{V}. \tag{3.33}$$

The stretch tensor $\boldsymbol{V}$ can be expressed in term of its eigenvalues and eigenvectors as

$$\boldsymbol{V} = \sum_{i=1}^{3} \lambda_i \boldsymbol{n}_i \otimes \boldsymbol{n}_i, \tag{3.34}$$

where λ_i (i = 1, 2, 3) are eigenvalues of $\boldsymbol{V}$ and $\boldsymbol{n}_i$ (i = 1, 2, 3) are corresponding eigenvectors. For a material unit, the macroscopic deformation gradient is given by Eq. (3.30), and the corresponding principal stretches are

$$\lambda_1 = \frac{\sqrt{2{D_0}^2+{\bar{\delta}_2}^2+{\delta_3}^2+2D_0(\bar{\delta}_2+\delta_3)+{\bar{\delta}_4}^2+\sqrt{\left((\bar{\delta}_2-\delta_3)^2+{\bar{\delta}_4}^2\right)\left((2D_0+\bar{\delta}_2+\delta_3)^2+{\bar{\delta}_4}^2\right)}}}{\sqrt{2}D_0},$$

$$\lambda_2 = \frac{(D_0+\delta_1)}{D_0}, \tag{3.35}$$

$$\lambda_3 = \frac{\sqrt{2{D_0}^2+{\bar{\delta}_2}^2+{\delta_3}^2+2D_0(\bar{\delta}_2+\delta_3)+{\bar{\delta}_4}^2-\sqrt{\left((\bar{\delta}_2-\delta_3)^2+{\bar{\delta}_4}^2\right)\left((2D_0+\bar{\delta}_2+\delta_3)^2+{\bar{\delta}_4}^2\right)}}}{\sqrt{2}D_0},$$

and therefore, the principal logarithmic strains are

$$\varepsilon_1 = \ln\lambda_1,$$

$$\varepsilon_2 = \ln\lambda_2, \tag{3.36}$$

$$\varepsilon_3 = \ln\lambda_3.$$

Finally, the effective strain can be calculated as

$$\varepsilon_e = \sqrt{\frac{2}{3}((\varepsilon_1-\varepsilon_m)^2+(\varepsilon_2-\varepsilon_m)^2+(\varepsilon_3-\varepsilon_m)^2)}, \tag{3.37}$$

where $\varepsilon_m = \frac{\varepsilon_1+\varepsilon_2+\varepsilon_3}{3}$.

Similarly, the macroscopic effective strain of the whole unit cell can be calculated using the principal stretches given by Eq. (3.38), corresponding to the macroscopic deformation gradient of the unit cell defined by Eq. (3.10)

$$\lambda_1 = \frac{\sqrt{2{D_0}^2+{\delta_2}^2+{\delta_3}^2+2D_0(\delta_2+\delta_3)+{\delta_4}^2+\sqrt{((\delta_2-\delta_3)^2+{\delta_4}^2)((2D_0+\delta_2+\delta_3)^2+{\delta_4}^2)}}}{\sqrt{2}D_0},$$

$$\lambda_2 = \frac{(D_0+\delta_1)}{D_0}, \tag{3.38}$$

$$\lambda_3 = \frac{\sqrt{2{D_0}^2+{\delta_2}^2+{\delta_3}^2+2D_0(\delta_2+\delta_3)+{\delta_4}^2-\sqrt{((\delta_2-\delta_3)^2+{\delta_4}^2)((2D_0+\delta_2+\delta_3)^2+{\delta_4}^2)}}}{\sqrt{2}D_0}.$$

3.2.7 The material model

The material chosen in this study obeys a power-law hardening, true stress-strain relation

$$\begin{aligned} \sigma &= E\varepsilon \qquad \varepsilon \le \varepsilon_0 \,, \\ \sigma &= \sigma_0 \left(\frac{\varepsilon}{\varepsilon_0}\right)^N \quad \varepsilon > \varepsilon_0 \,. \end{aligned} \tag{3.39}$$

where E represents the Young's modulus, σ_0 is the initial yield stress, ε_0 is the initial yield strain and N is the strain hardening exponent. The material parameters are taken to be $\varepsilon_0 = \frac{\sigma_0}{E} = 0.002$, $v = 0.3$ (Poisson's ratio), and $N = 0.1$.

3.3 Results and discussion

In the sandwiched unit cell model described in section 3.2.3, the three material units are stacked in the direction normal to the localization plane, where localization is to take place in the middle unit. Therefore, one needs to assume a localization plane orientation before conducting unit cell analysis. However, the orientation of the localization plane is affected by the stress state subjected by the material. This is demonstrated first in this section by analyzing a block of material subjected to different stress states. The subsequent unit cell analyses consider two unit cell models for each stress state, one has three material units stacked along X2 direction and the other has three material units stacked along X3 direction. The favored model under each applied stress state is selected as the one which leads to a lower localization strain.

3.3.1 Effect of stress state on the orientation of the localization plane

To demonstrate the effect of the stress state on the orientation of the localization plane, consider a block of material consisting of 3×3 material units as shown in Fig. 3.5. The initial void in the material unit at the center is slightly larger than in other eight material units to trigger the onset of localization. The initial void volume fraction of the center material units is 0.004188. Periodic boundary conditions are imposed on the $X_2 = \pm 3D_0$ and $X_3 = \pm 3D_0$ surfaces. Symmetry condition is imposed on $X_1 = 0$ and homogeneous boundary condition is applied on $X_1 = D_0$. Displacement-controlled loading is imposed on the model to ensure the ratios between the applied macroscopic stress components remain constant during the loading history. For the cases of $\Sigma_{11} = \Sigma_{33}$ and specified $T = 3$ and μ = -1, 0, 1, corresponding to generalized tension, generalized shear and generalized compression respectively, Fig. 3.6 shows the matrix plastic strain distribution after the analysis results have shown clearly visible evidence of strain localization, i.e., further strain accumulation localizes in a band. Since only the center void is slightly larger while the other voids have the same size, the resulted localization plane is not due to predefined perturbations. It is clear from Fig. 3.6 that for μ = -1, localization takes place in the row of material units in the X_1-X_3 plane and so as for μ = 0, but for μ = 1, localization takes place in the X_1-X_2 plane. It is also worth noting that failure in the $\mu = \pm 1$ cases is due to void growth and internal necking while in the μ = 0 case is due to a combination of void growth and void shearing.

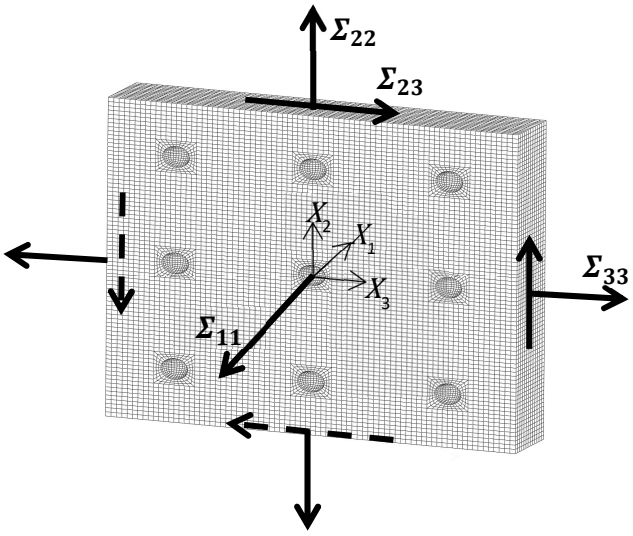

Figure 3.5. Finite element mesh of a block of material consisting of 3 × 3 material units

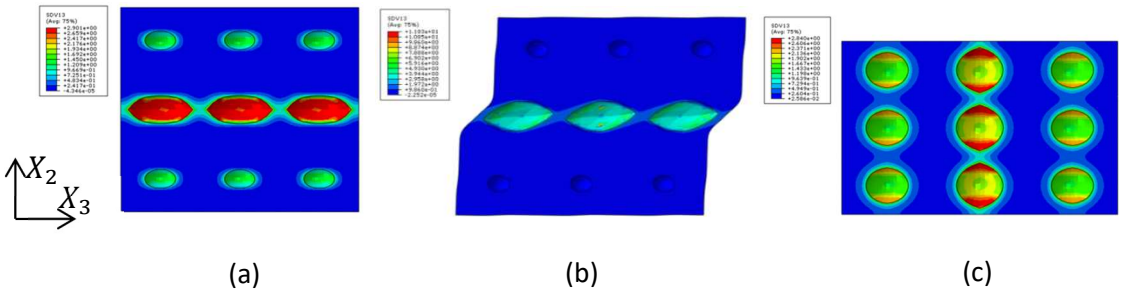

Figure 3.6. Matrix plastic strain distribution for $T = 3$, and (a) $\mu = -1$, (b) $\mu = 0$, (c) $\mu = 1$.

For the sandwiched unit cell model described in Section 3.2, three material units are stacked in the direction normal to the plane where localization is to occur. However as shown in Fig. 3.6, the orientation of the localization plane is influenced by the stress state subjected by the material. Without knowing the orientation of the localization plane a priori, a series of unit cell analyses can be conducted by rotating the Cartesian coordinate system by different θ-angles about the X_1-axis, Barsoum and Faleskog (2011). The θ-angle corresponding to the actual orientation of the localization plane would result in the

predicted localization strain to be minimum. The process is straightforward but tedious and time-consuming. As the main objectives of the present paper are to introduce this new sandwiched unit cell model and to establish an easy-to-implement failure criterion, analyses to determine the orientation of the localization plane under different stress state will only be conducted for a few cases in section 3.3.6 as a discussion for error estimation. Elsewhere in this paper, a simple approach is adopted, where two unit cell models are considered for each stress state, one has three material units stacked along X_2 direction and the other has them stacked along X_3 direction. The second model is achieved by rotating the Cartesian coordinate system of the first model by $\pi/2$ about the X_1-axis. These two models correspond to the cases where localization occurs in the X_1-X_3 plane and X_1-X_2 plane respectively. The favored model under each applied stress state is selected as the one which leads to a lower localization strain. It is observed from a series of numerical simulations that for $\mu \leq 0$ the model with three material units stacked along X_2 direction yields a lower localization strain while for $\mu > 0$ the model with three material units stacked along X_3 direction yields a lower localization strain.

3.3.2 Unit cell analysis

For the sandwiched unit cell model, after localization occurs in the middle material unit (inside layer), the other two material units (outside layers) will soon experience elastic unloading. Therefore, the deformation of the unit cell quickly localizes toward the inside layer, which can be analyzed by examining the strain variation of the inside and outside layers respectively. Consider a case of $T = 0.8$ and $\mu = 0$. Fig. 3.7 shows the evolution of the macroscopic effective strain of the inside layer and outside layer as the displacement-

controlled loading increases. Before the onset of localization, the two curves coincide, suggesting the two material units are almost identical and experiencing the same deformation. The two curves start to deviate as localization initiates: the effective strain of the outside layer increases at a reduced rate comparing to the inside layer. As the deformation continues, the effective strain of the inside layer increases rapidly while the effective strain of the outside layer reaches a maximum and then decreases. The macroscopic effective strain decrease for the outside layer is the result of the elastic strain reduction due to unloading. Since the applied load is displacement-controlled, the unloading does not look dramatic in the effective strain vs. the applied load history curve. However, the inset in Fig. 3.7, with the scale of the ordinate magnified, clearly show the point when the macroscopic effective strain of the outside layer starts decreasing.

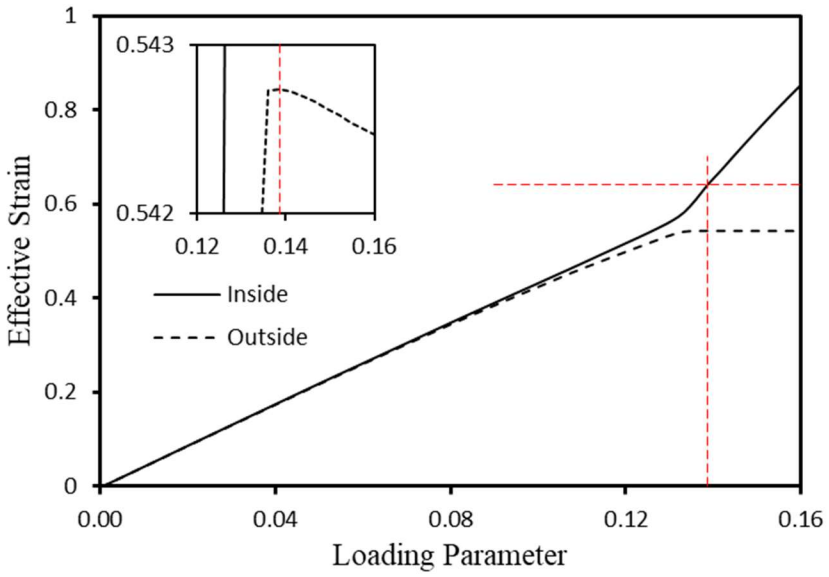

Figure 3.7. Macroscopic effective strain vs. loading parameter curves for the inside and outside layers ($T = 0.8$, $\mu = 0$).

To further understand the deformation and localization process experienced by the unit cell, the evolution processes of the macroscopic effective strain and effective stress of the inside layer, outside layer and whole unit cell for the case of $T = 0.8$ and $\mu = 0$ are compared in Fig. 3.8. The effective stress is calculated using Eq. (3.1) with the macroscopic stress components computed as

$$\Sigma_{ij} = \frac{1}{V}\int \sigma_{ij}\, \mathrm{d}V, \tag{3.40}$$

where σ_{ij} represents the Cauchy stress output at element Gauss points and V is the volume of the material unit or the whole unit cell.

Fig. 3.8(a) shows that after the onsite of localization, the overall effective strain of unit cell keeps increasing steadily, but the strain is quickly localized into the inside layer while the strain in the outside layer stops increasing. As the deformation of the inside layer continues, the ligament size reduces due to void growth and/or void shearing. When the effect of ligament reduction overtakes the effect of material strain hardening, the load carrying capacity of the inside layer decreases, and as a result, the effective stress of the inside layer, outside layer and the whole unit cell decreases, Fig. 3.8(b). This process can be more clearly illustrated by plotting the macroscopic effective stress vs. effective strain curves for the inside layer, outside layer and the whole unit cell, Figs 3.8(c-e). The elastic unloading of the outside layer shown in Fig. 3.8(e) can serve as an indicator for fracture. After this point, the inside layer quickly loses its load carrying capacity to sustain continued loading, and the unit cell fails by ductile fracture.

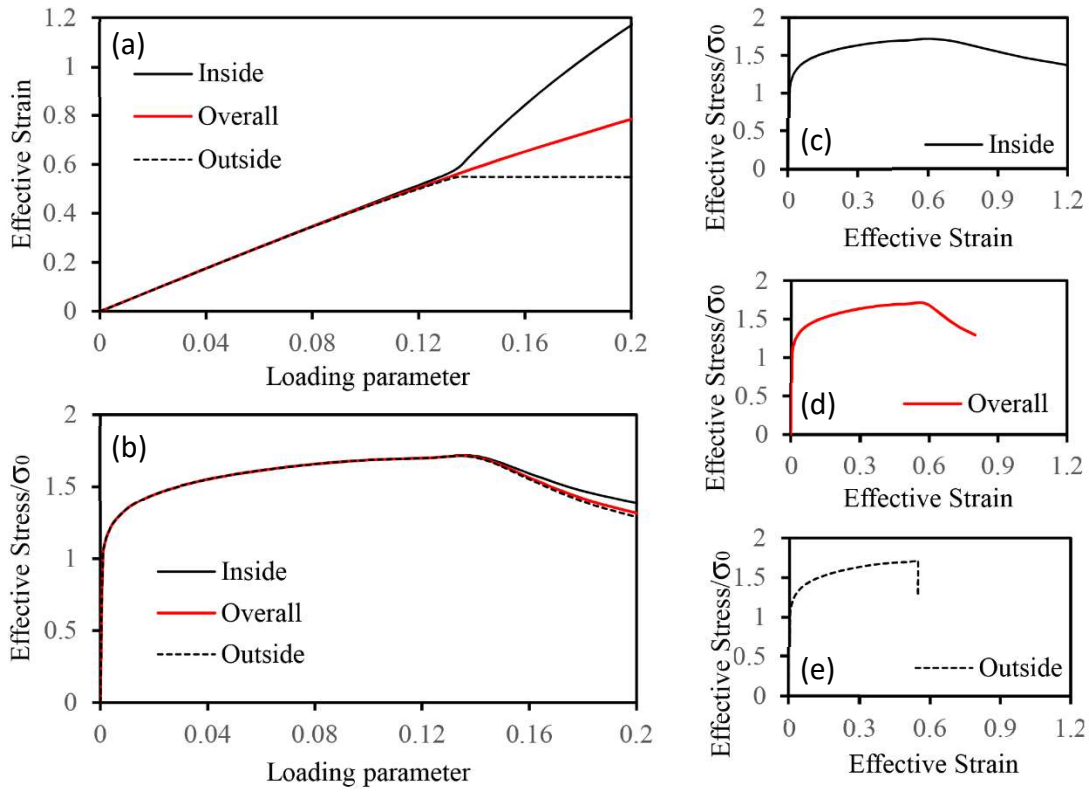

Figure 3.8. Evolution of the macroscopic effective strain and effective stress of the inside layer, outside layer and whole unit cell ($T = 0.8$, $\mu = 0$): (a) effective strain vs. loading history, (b) effective stress vs. loading history, (c) effective stress vs. effective strain for the inside layer, (d) effective stress vs. effective strain for the whole unit cell, (e) effective stress vs. effective strain for the outside layer.

Similar analyses can be done for the μ = -1 and μ = 1 cases and the results are shown in Fig. 3.9 and Fig. 3.10 respectively. In these cases, the applied stress triaxiality is $T = 0.8$.

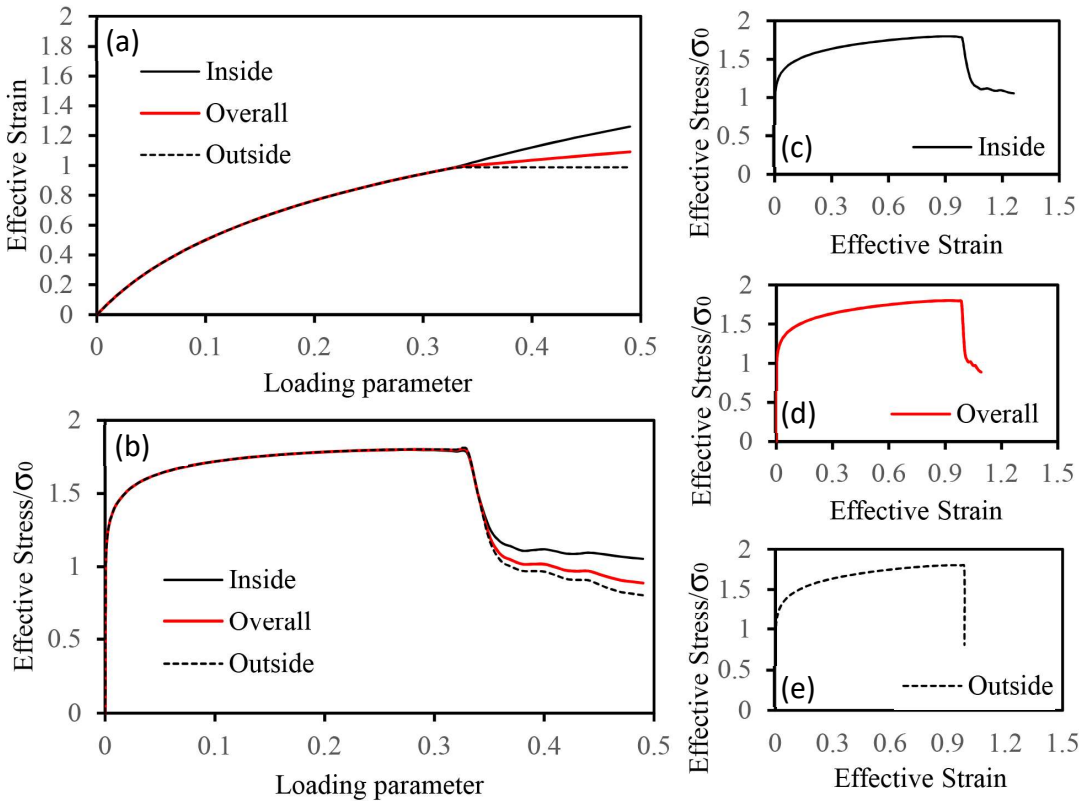

Figure 3.9. Evolution of the macroscopic effective strain and effective stress of the inside layer, outside layer and whole unit cell ($T = 0.8$, $\mu = -1$): (a) effective strain vs. loading history, (b) effective stress vs. loading history, (c) effective stress vs. effective strain for the inside layer, (d) effective stress vs. effective strain for the whole unit cell, (e) effective stress vs. effective strain for the outside layer.

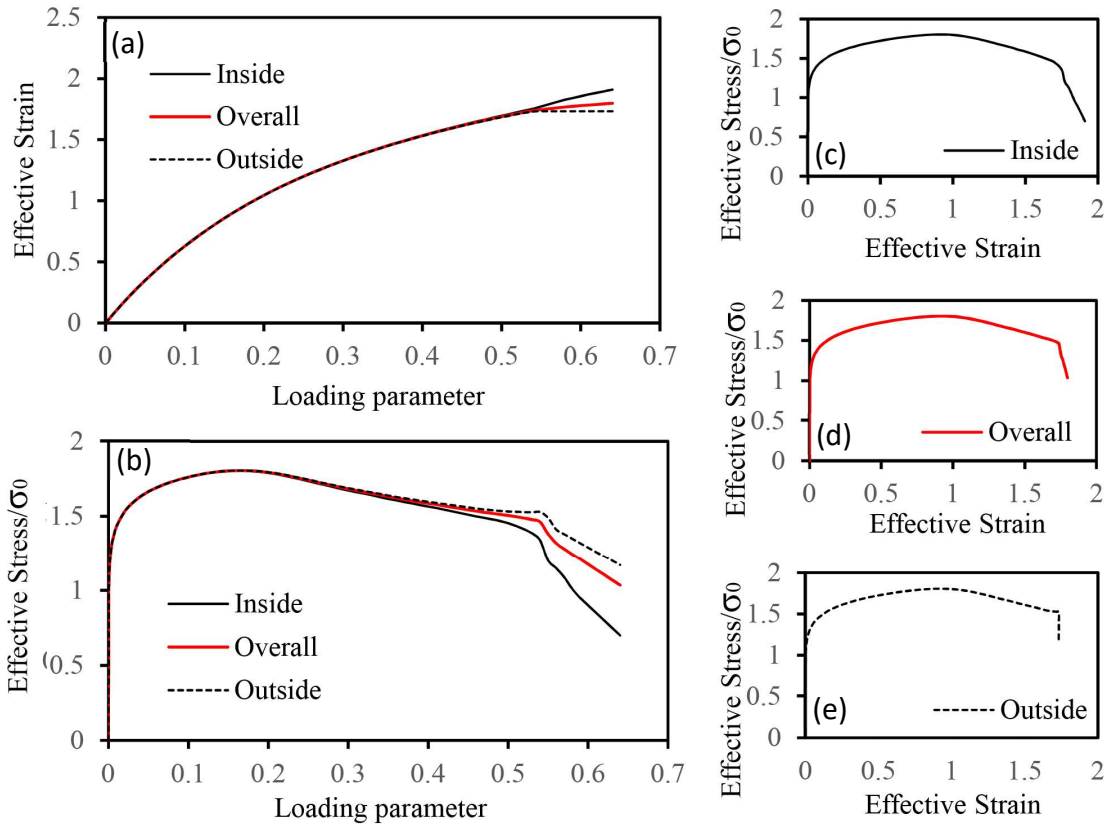

Figure 3.10. Evolution of the macroscopic effective strain and effective stress of the inside layer, outside layer and whole unit cell ($T = 0.8$, $\mu = 1$): (a) effective strain vs. loading history, (b) effective stress vs. loading history, (c) effective stress vs. effective strain for the inside layer, (d) effective stress vs. effective strain for the whole unit cell, (e) effective stress vs. effective strain for the outside layer.

The above discussion suggests that the localization process can be divided into two stages. The first stage is from the point when the macroscopic effective strain of the outside layer deviates from the macroscopic effective strain of the inside layer to the point when the macroscopic effective strain of the outside layer reaches the maximum. From hereafter is the second stage, in which the outside layer undergoes elastic unloading while the

deformation of the unit cell quickly localizes in the inside layer and the material loses the load carrying capacity shortly after.

Consequently, a material failure criterion can be established as a result of the unit cell analysis: failure occurs when the macroscopic effective strain of the outside layer reaches the maximum. The material failure strain under a given stress state can then be defined as the macroscopic effective strain of the unit cell when the outside layers start to unload elastically. For the example of $T = 0.8$ and $\mu = 0$, the first stage of localization starts at a macroscopic effective strain level of 0.4; the maximum value of the macroscopic effective strain of the outside layer is 0.55, and in the meantime the macroscopic effective strain of the inside layer is 0.64 and the macroscopic effective strain of the unit cell is 0.58, which is defined as the failure strain of the material at the prescribed stress state in this paper.

Note that because of the multi-scale nature of the sandwiched unit cell model, although the overall loading at the unit cell level is proportionally imposed, the stress state at the length-scale of the material unit becomes non-proportional after the onset of localization. In the present study, the prescribed stress state is enforced on the unit cell level, e.g., the T and μ values remain constant at this length-scale through the whole loading history. But when examining the stress state for an individual material unit, e.g., the inside or outside material unit, as is shown in Fig. 3.11, the T and μ values deviate from the prescribed value after the onsite of localization. Due to the multi-scale nature of the model, the failure strain can be defined at different length scales, e.g., the inside layer, the outside layer, and the whole unit cell. For examples, when analyzing the effects of voids in the outside layers on the ductile fracture process, it is natural to examine their effect on

the failure strain of the inside layer; but when predicting failure strain for engineering applications, it is more relevant to define the failure strain at the unit cell level.

Moreover, in an actual material, the large plastic deformation in the localization band will result in the nucleation of secondary micro voids in large numbers. Rapid growth and coalescence of these secondary voids will further soften the material, which in turn will intensify the localization process and accelerate material failure. This is, however, not taken into account here, and thus the post-localization process is not accurately modeled in the present study.

3.3.3 Effect of the voids in the outside layers

In several previous studies (Barsoum and Faleskog, 2007, 2011; Dunand and Mohr, 2014; Wong and Guo, 2015), the unit cell has a similar overall geometry as the present model. But these previous models only included a single void located at the center of the unit cell while treating the material outside the localization plane as void free. However, voids do nucleate elsewhere and interact with each other. It is expected that the presence of the voids in the outside layers would have an influence on the void behavior in the inside layer.

To investigate this issue, two unit cell models are analyzed here. The first one is the proposed model consisting of three void-containing material units, referred to as VPO hereafter. The second one also consists of three material units but only the middle unit contains a void at its center, referred to as VAO hereafter. The same boundary conditions and displacement-controlled macroscopic loading are imposed on the two models.

Fig. 3.11 compares the evolution of the macroscopic stress triaxiality and Lode parameter of the inside layer and outside layer during the loading history. Here the applied $T = 1.2$ and $\mu = 0.5$. In Figs. 3.11(a) and (b), where the proposed unit cell model is used, T and μ remain the same for the inside and outside layers and maintain the applied values until localization takes place. In Figs. 3.11(c) and (d), where the outside layer is void free, T and μ for neither layer equal to the applied values: T for the outside (inside) layer is less (greater) than the applied value while μ for the outside (inside) layer is greater (less) than the applied value. Furthermore, T and μ do not maintain constant values for each layer: T for the outside (inside) layer decreases (increases), while μ for the outside (inside) layer increases (decreases), as loading continues.

Fig. 3.12 compares the T and μ vs. macroscopic effective strain curves for the inside layer between the two models. As can be seen from Fig. 3.12(a), the absence of voids in the outside layers raises the stress triaxiality imposed on the inside layer. Consequently, void growth in the inside layer becomes faster, making failure to occur earlier. For the applied $T = 1.2$ and $\mu = 0.5$, the proposed unit cell model predicts a failure strain for the inside layer as 0.48, while the model without voids in the outside layers predicts a failure strain of 0.37.

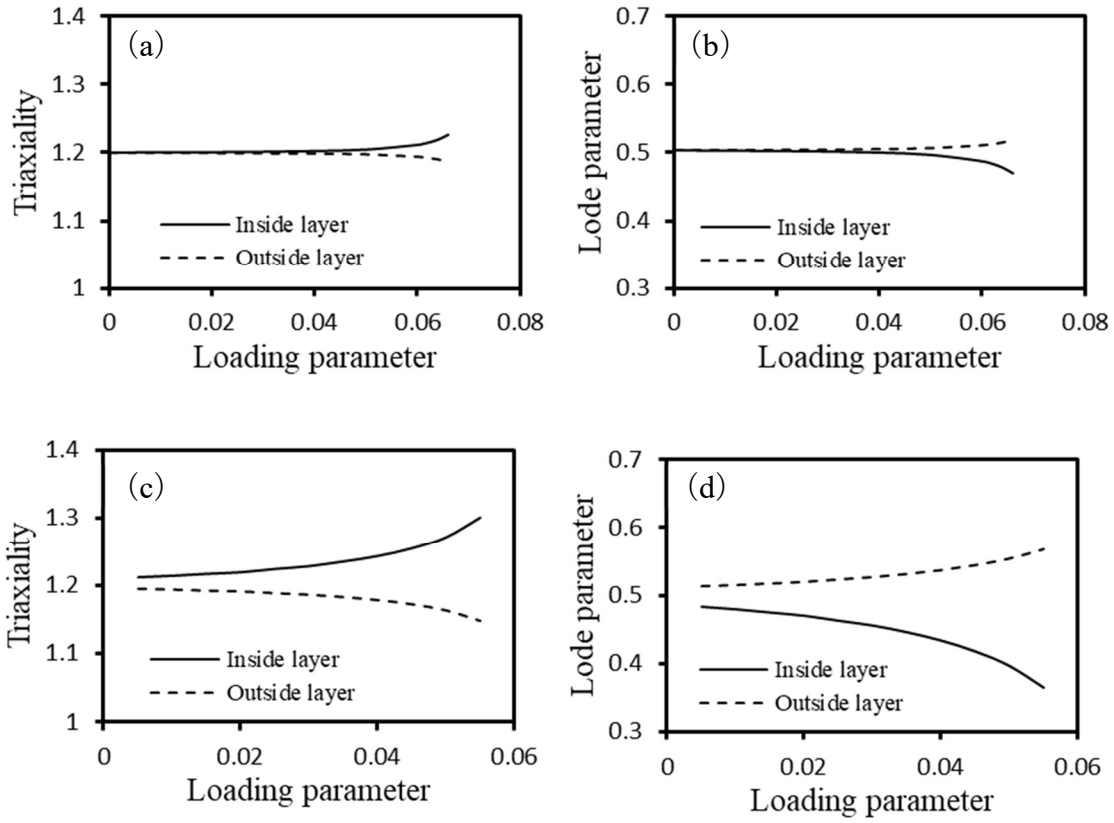

Figure 3.11. Evolution of the macroscopic stress triaxiality and Lode parameter of the inside layer and outside layer during the loading history: (a) stress triaxiality, the proposed unit cell model; (b) Lode parameter, the proposed unit cell model; (c) stress triaxiality, the model without voids in the outside layers; (d) Lode parameter, the model without voids in the outside layers

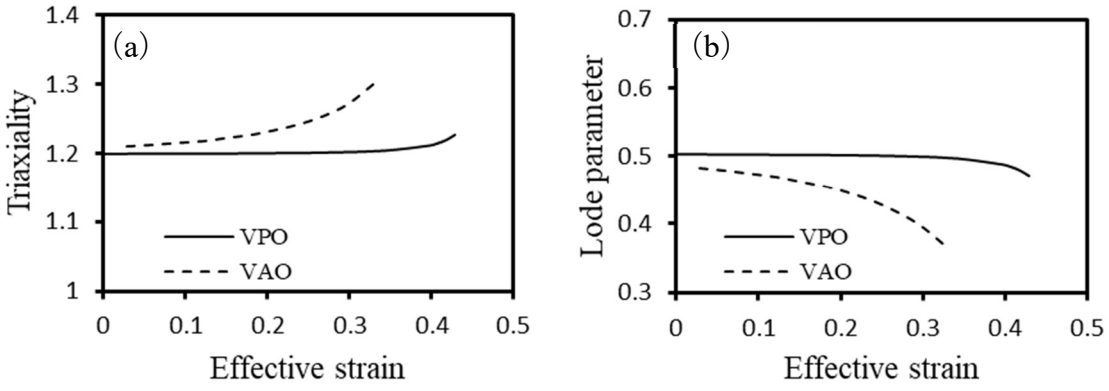

Figure 3.12. Comparison of the macroscopic stress state of the inside layer between the two unit cell models: (a) stress triaxiality vs. effective strain, (b) Lode parameter vs. effective strain

Fig. 3.13 shows the predicted failure strain for the inside layer using the two unit cell models under various applied T and μ values, where the solid lines represent the results from the proposed model while the dashed lines represent the results from the model without voids in the outside layers. In general, the proposed model predicts a higher value of failure strain than the model without voids in the outside layers, except for when μ is around 0. When $\mu \approx 0$, the two models predict the same value of failure strain. This is further illustrated in Fig. 3.14, where the case of $T = 0.8$ and $\mu = 0$ is taken into consideration. As explained in the previous section, the failure strain in this section is defined at the inside layer level. Although the maximum effective strain of the outside layer is different in the two unit cell models, the corresponding effective strain values of the inside layer are almost the same.

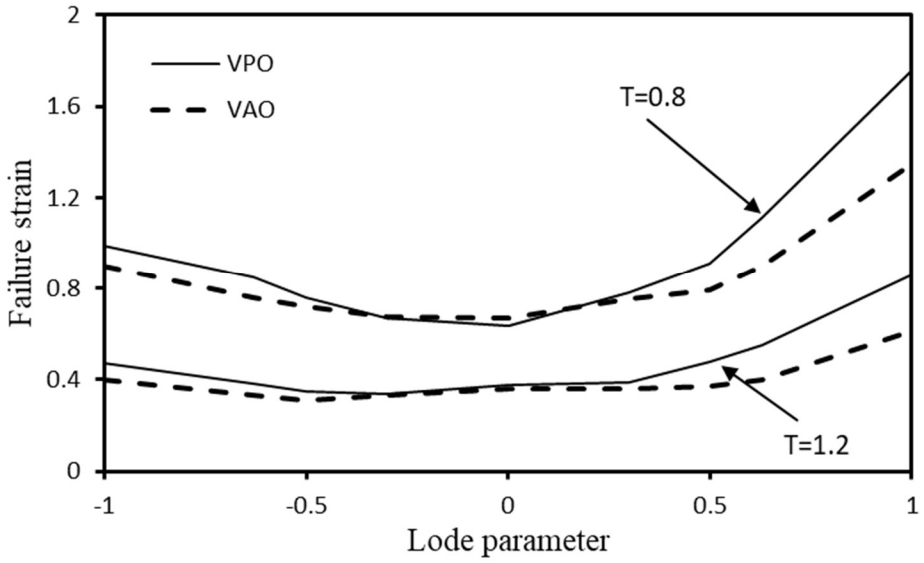

Figure 3.13. Predicted failure strain of the inside layer using two unit cell models under various applied T and μ values

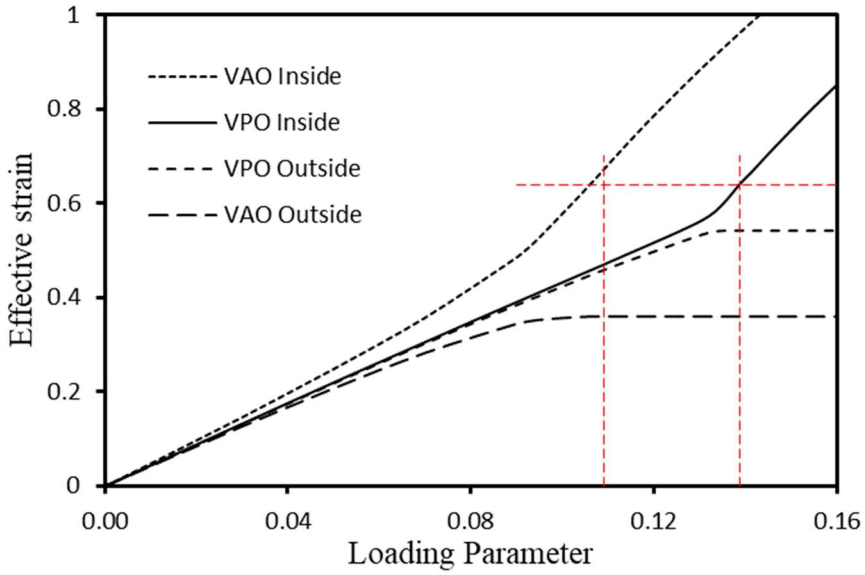

Figure 3.14. Comparison of the macroscopic effective strain vs. loading parameter curves for the inside and outside layers between the two unit cell models ($T = 0.8$, $\mu = 0$).

For the case of $T = 0.8$ and $\mu = 0$, Fig. 3.15 compares the macroscopic stress-strain responses between the proposed model and the model without voids in the outside layers. As shown in Fig. 3.15(a), the VAO model has a slightly higher stress-strain curve for the outside layer, but elastic unloading occurs earlier than the VPO model. Consequently, as shown in Fig. 3.15(b), almost the same amount of overall constraint is imposed on the inside layer. This is evident from Fig. 3.16, where the macroscopic stress triaxiality vs. effective strain and Lode parameter vs. effective strain curves for the inside layer are displayed. The inside layer in the VPO model and the VAO model experience almost the same stress triaxiality and Lode parameter. Therefore, the predicted failure strain shows little difference.

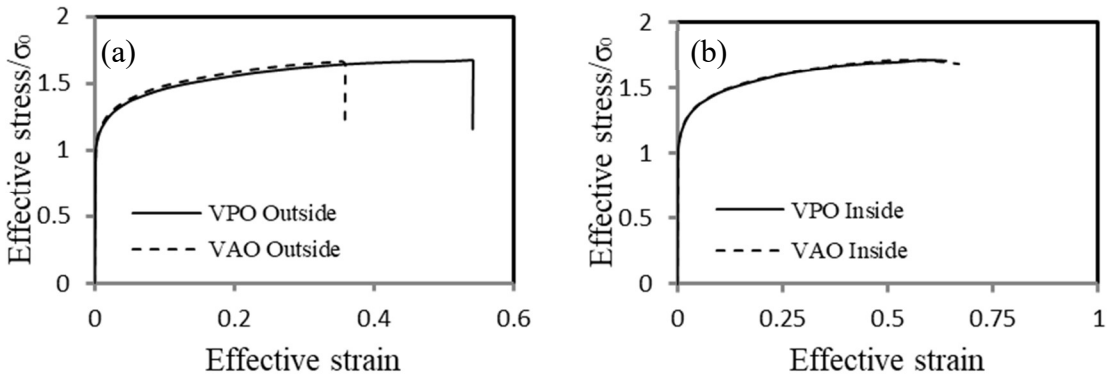

Figure 3.15. Comparison of the macroscopic stress-strain responses between the proposed model and the model without voids in the outside layers for the case of $T = 0.8$ and $\mu = 0$.

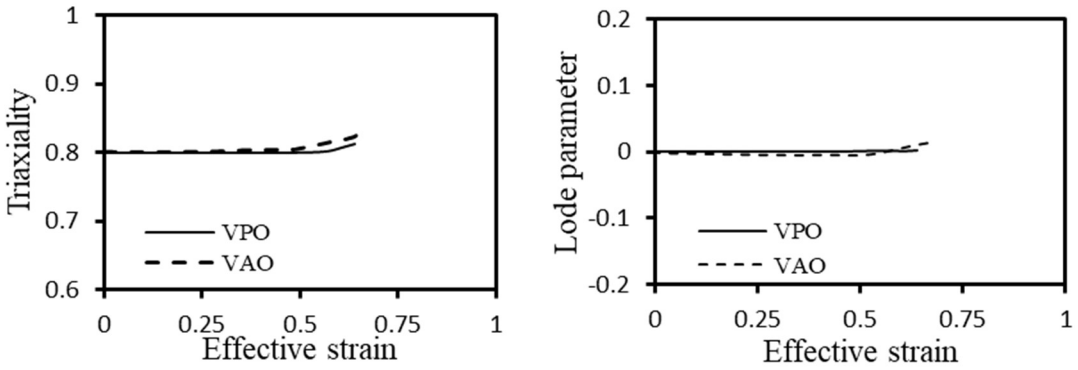

Figure 3.16. Comparison of the macroscopic stress triaxiality and Lode parameter of the inside layer between the proposed model and the model without voids in the outside layers for the case of $T = 0.8$ and $\mu = 0$.

Nahshon and Hutchinson (2008) also noticed the effect of the voids outside the localization band. Our analyses confirm that voids in the outside layer do affect the stress state and void behavior in the inside layer in general, except for when $\mu \approx 0$. To account for this effect, the unit cell model consisting of three void-containing material units is adopted in this study.

3.3.4 Comparison with localization criteria adopted in previous studies

3.3.4.1 The method based on the localization criterion of Rice-Needleman-Tvergaard

Needleman and Tvergaard (1992) introduced an often-used localization criterion based on the theoretical framework of plastic localization into a band by Rice (1977). Using this criterion, Barsoum and Faleskog (2007) presented a numerical approach to predict ductile failure by comparing the norm of the deformation gradient rates inside and outside the band,

$$\eta = \left\| \bar{\dot{\boldsymbol{F}}} \right\| / \left\| \bar{\dot{\boldsymbol{F}}}^{o} \right\| \to \infty, \tag{3.41}$$

where $\bar{\dot{\boldsymbol{F}}}$ and $\bar{\dot{\boldsymbol{F}}}^{o}$ represent the macroscopic deformation gradient rates inside and outside the band of localized deformation respectively. This method has been adopted in several recent studies, such as Barsoum and Faleskog (2011) and Dunand and Mohr (2014), with different critical η-values used to set the failure criterion. For the analyses performed in this section, the macroscopic deformation gradient rates inside and outside the localization band will be computed by taking the volume average of the deformation gradient rates obtained in the inside layer and outside layer respectively.

Barsoum and Faleskog (2011) commented that this method cannot be applied to high triaxiality cases when the Lode parameter is close to zero. In these cases, it was observed that the η-value display a spike as soon as plasticity sets in. Here this problem is examined by considering the applied stress state of $T = 2$ and $\mu = 0$. For comparison, the two unit cell models described in the previous section, one including voids in the outside layers and the other ignoring voids in the outside layers, are employed in the finite element analyses. Fig. 3.17 compares the curves of the computed η vs. macroscopic effective strain of the inside layer obtained from the two models. In the small deformation region the result obtained from the VAO model does show a spike. However, the result obtained from the VPO model does not display such spike.

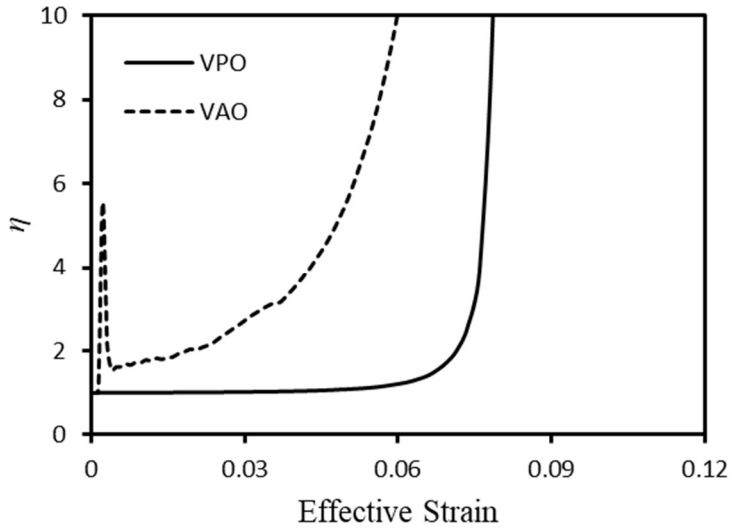

Figure 3.17. The computed η vs. macroscopic effective strain of the inside layer obtained from the two models ($T = 2$, $\mu = 0$)

The spike in the η vs. macroscopic effective strain curve is due to the ignorance of voids in the outside layers. Since the outside layer is void free, once plasticity sets in, the deformation will be concentrated around the void in the inside layer, resulting a quick increase of η. However, this localized deformation around the void does not propagate rapidly to form a localization band to cause material failure. As can be seen in Fig. 3.17, η drops immediately after the spike, then increases monotonically, and becomes unstable at a much later stage of loading.

The choice of critical η-value would have a large influence on the predicted failure strain. Theoretically, η should goes to infinity. But practically different critical values of η have been suggested in previous studies. From the results presented in Fig. 3.17, the choice of a critical η-value of 2, 5 and 10 would predict a failure strain for the inside layer of 0.0017, 0.0023, and 0.06 respectively using the VAO model, and 0.071, 0.078 and 0.08 respectively using the VPO model.

However, as indicated in Fig. 3.18, the ambiguity of choosing different critical η-values can be avoided by using the failure criterion proposed in this study, i.e., failure occurs when the macroscopic effective strain of the outside layer reaches the maximum. From Fig. 3.18, the predicted failure strain is 0.097 and 0.103 using the VPO and VAO models respectively.

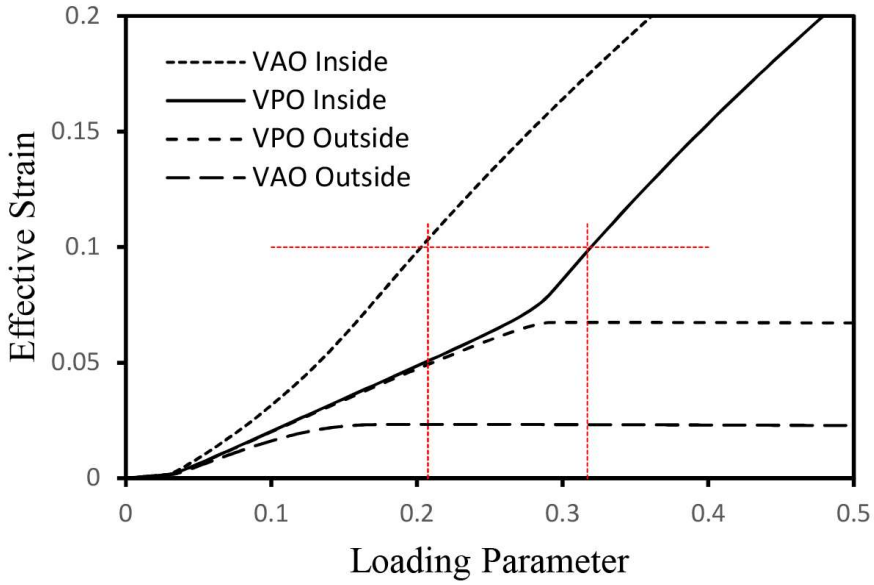

Figure 3.18. Macroscopic effective strain vs. loading parameter curves for the inside and outside layers ($T = 2$, $\mu = 0$).

3.3.4.2 The energy-based criterion by Wong and Guo

Wong and Guo (2015) recently proposed an energy-based method to predict the onset of void coalescence by comparing the elastic energy and plastic energy during the loading history. The overall elastic and plastic work rates of the unit cell are calculated as

$$\dot{W}_e = \int_V \sigma : d^e \, \mathrm{d}V \quad \text{and} \quad \dot{W}_p = \int_V \sigma : d^p \, \mathrm{d}V \,, \tag{3.42}$$

where σ is the local Cauchy stress tensor, and d^e and d^p are the elastic and plastic parts of the rate of deformation tensor respectively. This method identifies the state of elastic unloading as when $\frac{\dot{W}_e}{\dot{W}_p}$ changes from positive to negative. Since $\dot{W}_p$ remains positive or zero as it is related to plastic deformation, the sign change of $\frac{\dot{W}_e}{\dot{W}_p}$ is caused by $\dot{W}_e$. The onset of void coalescence is said to occur when $\frac{\dot{W}_e}{\dot{W}_p}$ reaches a minimum.

In the analyses presented below, the applied load on the sandwiched unit cell is characterized by T = 2, and μ = -1, 0 and 1 respectively. Figs 3.19 to 3.20 present the numerical results, where the effective strain of the inside layer is used as the abscissa of all plots, the green "+" symbol corresponds to the strain value, E_e, when $\frac{\dot{W}_e}{\dot{W}_p}$ becomes negative, the black "×" symbol corresponds to the strain value, E_c, when $\frac{\dot{W}_e}{\dot{W}_p}$ reaches the minimum, the black "○" symbol corresponds to the strain value, E_η, when the η-value reaches 10, and the red "■" symbol corresponds to the strain value, E_f, the failure strain for the inside layer determined by the criterion proposed in this paper. Subfigures (a) show the effective stress-strain curves of the inside layer. Subfigures (b) show the plots of the effective strain of the outside layer vs. the effective strain of the inside layer. Subfigures (c) show the evolution of $\frac{\dot{W}_e}{\dot{W}_p}$ of the inside layer, the outside layer, and the whole unit cell respectively. Subfigures (d) shows the evolution of the elastic and plastic work rates, $\dot{W}_e$ and $\dot{W}_p$ normalized by minimum $\dot{W}_e$ magnitude, for the outside layer.

Fig. 3.19 shows that for μ = -1, E_e occurs shortly after the effective stress of the inside layer reaches the maximum, and E_η, E_c, and E_f values determined by the three methods are the same. Fig. 3.20 shows that for L = 0, E_η and E_e are same and are slightly

less than E_f, but E_c can only be reached at a much later loading stage. Fig. 3.21 shows that for $\mu = 1$, E_e occurs shortly after the effective stress of the inside layer reaches the maximum, while E_η and E_f are the same and are slightly less than E_c. These results suggest that using the proposed sandwiched unit cell model with $\eta > 10$, the failure criterion put forth by Barsoum and Faleskog (2007) can be considered equivalent to the failure criterion proposed in this paper.

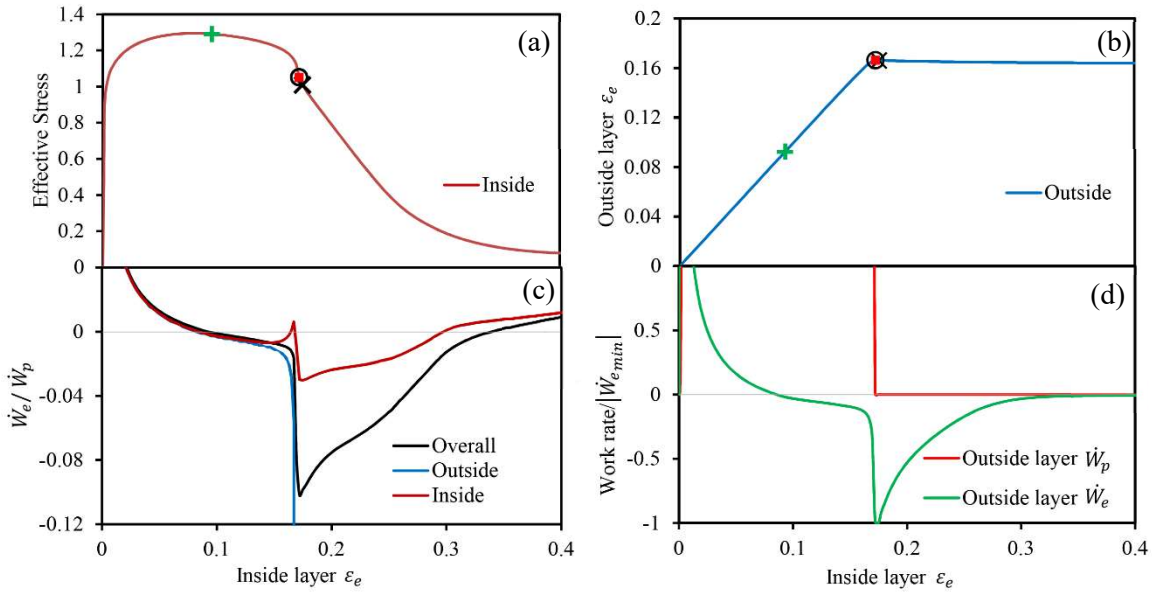

Figure 3.19. Numerical results for $T = 2$ and $\mu = -1$: (a) the effective stress-strain curve of the inside layer, (b) the effective strain of the outside layer vs. the effective strain of the inside layer, (c) evolution of $\frac{\dot{W}_e}{\dot{W}_p}$ of the inside layer, the outside layer, and the whole unit cell, (d) evolution of $\dot{W}_e$ and $\dot{W}_p$ for the outside layer.

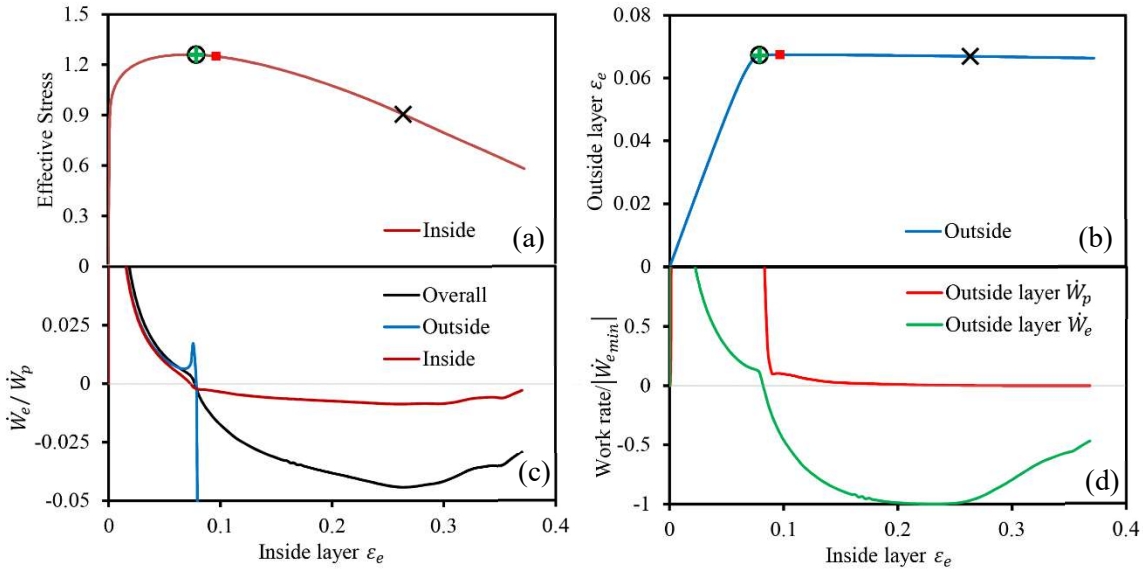

Figure 3.20. Numerical results for $T = 2$ and $\mu = 0$: (a) the effective stress-strain curve of the inside layer, (b) the effective strain of the outside layer vs. the effective strain of the inside layer, (c) evolution of $\frac{\dot{W}_e}{\dot{W}_p}$ of the inside layer, the outside layer, and the whole unit cell, (d) evolution of $\dot{W}_e$ and $\dot{W}_p$ for the outside layer.

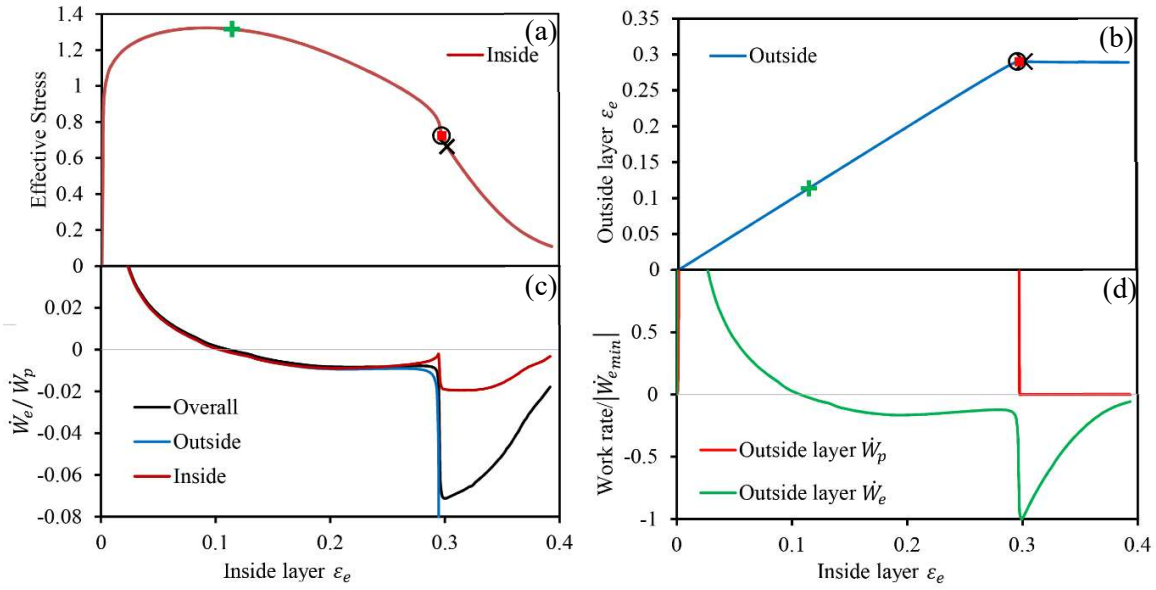

Figure 3.21. Numerical results for $T = 2$ and $\mu = 1$: (a) the effective stress-strain curve of the inside layer, (b) the effective strain of the outside layer vs. the effective strain of the inside layer, (c) evolution of $\frac{\dot{W}_e}{\dot{W}_p}$ of the inside layer, the outside layer, and the whole unit cell, (d) evolution of $\dot{W}_e$ and $\dot{W}_p$ for the outside layer.

Now the attention is turned to the energy-based method. During the void growth process, the material in the vicinity of the void will experience elastic unloading while the material away from the void may still be under elastic-plastic loading. The elastic work rate of the material unit includes contributions from the vicinity of the void as well as the region away from the voids. When the negative contribution from the vicinity of the void overtakes the positive contribution from the region away from the void, the total $\dot{W}_e$ becomes negative. However, this does not mean that macroscopically the material unit is under elastic unloading. Figs 3.19-3.21 clearly demonstrate this, where E_f is always greater than E_e, especially for the $\mu = \pm 1$ cases.

From subfigures (c) it can be seen that $\frac{\dot{W}_e}{\dot{W}_p}$ of the inside layer and that of the outside layer are the same in the early loading stage. As the effective strain of the inside layer approaches to E_f, the $\frac{\dot{W}_e}{\dot{W}_p}$ curves for the inside layer and outside layer start to deviate. When the effective strain of the inside layer is equal to E_f, $\dot{W}_p$ for the outside layer goes to zero thus $\frac{\dot{W}_e}{\dot{W}_p}$ goes to -∞ for all three cases, and for the $\mu = \pm 1$ cases, $\frac{\dot{W}_e}{\dot{W}_p}$ for the inside layer as well as for the whole unit cell reaches the minimum values. For the $\mu = 0$ case, the minimum of the overall $\frac{\dot{W}_e}{\dot{W}_p}$ occurs much later than E_f, therefore, Wong and Guo's void coalescence criterion (Wong and Guo, 2015) predicts a much larger failure strain than the model proposed in this paper does.

3.3.5 The effect of stress state on ductile fracture

3.3.5.1 Failure strain as a function of stress triaxiality and Lode parameter

In this section, the sandwiched unit cell model and the failure criterion proposed in this study are applied to analyze the effect of stress state on ductile fracture. Here the failure strain is defined as the overall effective strain of the unit cell model at the instant when the effective strain of the outside layer reaches the maximum. Various values of stress triaxiality, from 0.4 to 3, and Lode parameter, from -1 to 1, are imposed on the unit cell. Finite element analysis results indicate that cases with low triaxiality and high Lode parameter may encounter void surface contact due to limited void growth. Since void surface contact is not taken into account in the present study, these cases are omitted. Discussions regarding void surface contact modeling and void collapse behavior were

reported in a number of previous studies (Tvergaard, 2008; Tvergaard, 2009; Nielsen et al., 2012; Liu et al., 2016). Fig. 3.22 shows the predicted failure strain as a function of the stress triaxiality and Lode parameter based on the cases analyzed. For a given Lode parameter, the failure strain can be approximated as an exponentially decaying function of the stress triaxiality. For a given stress triaxiality, the failure strain changes little around $\mu = 0$, but increases as μ approaches -1 and 1, Fig. 3.23. Note that the minimum failure strain is not necessary at $\mu = 0$. For example, the minimum failure strain occurs at $\mu \approx -0.3$ when $T > 0.8$. Fig. 3.23 also suggests that the effect of the Lode parameter is more pronounced when the stress triaxiality is low. Fig. 3.24 shows the deformed void shape in the inside layer when failure strain is reached under various stress states, where the numbers in the figure indicate the corresponding strain values. Similar results were reported in previous studies (Barsoum and Faleskog, 2011; Tvergaard, 2012; Dunand and Mohr, 2014).

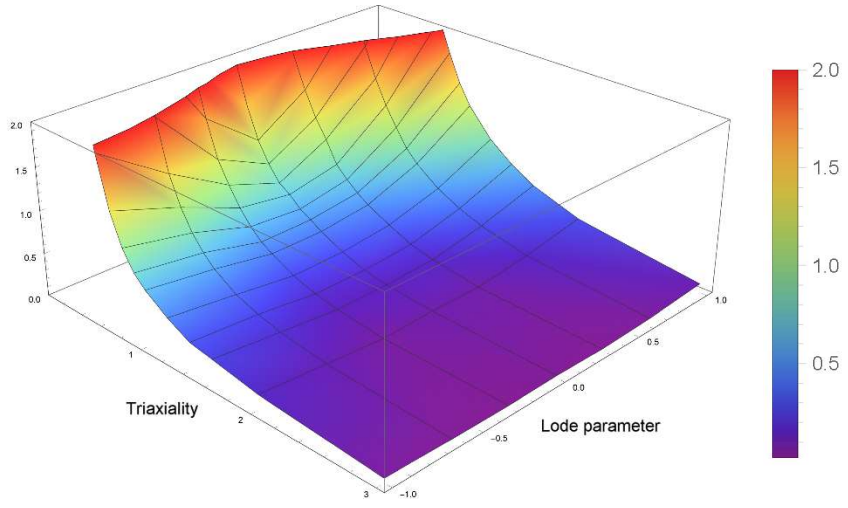

Figure 3.22. Failure strain as a function of the stress triaxiality and Lode parameter.

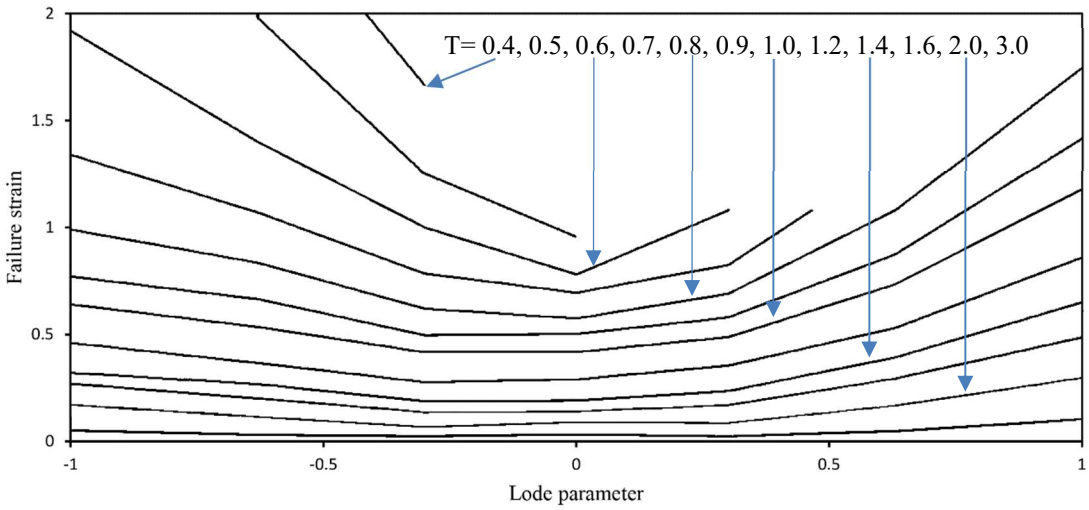

Figure 3.23. Variation of the failure strain with the Lode parameter

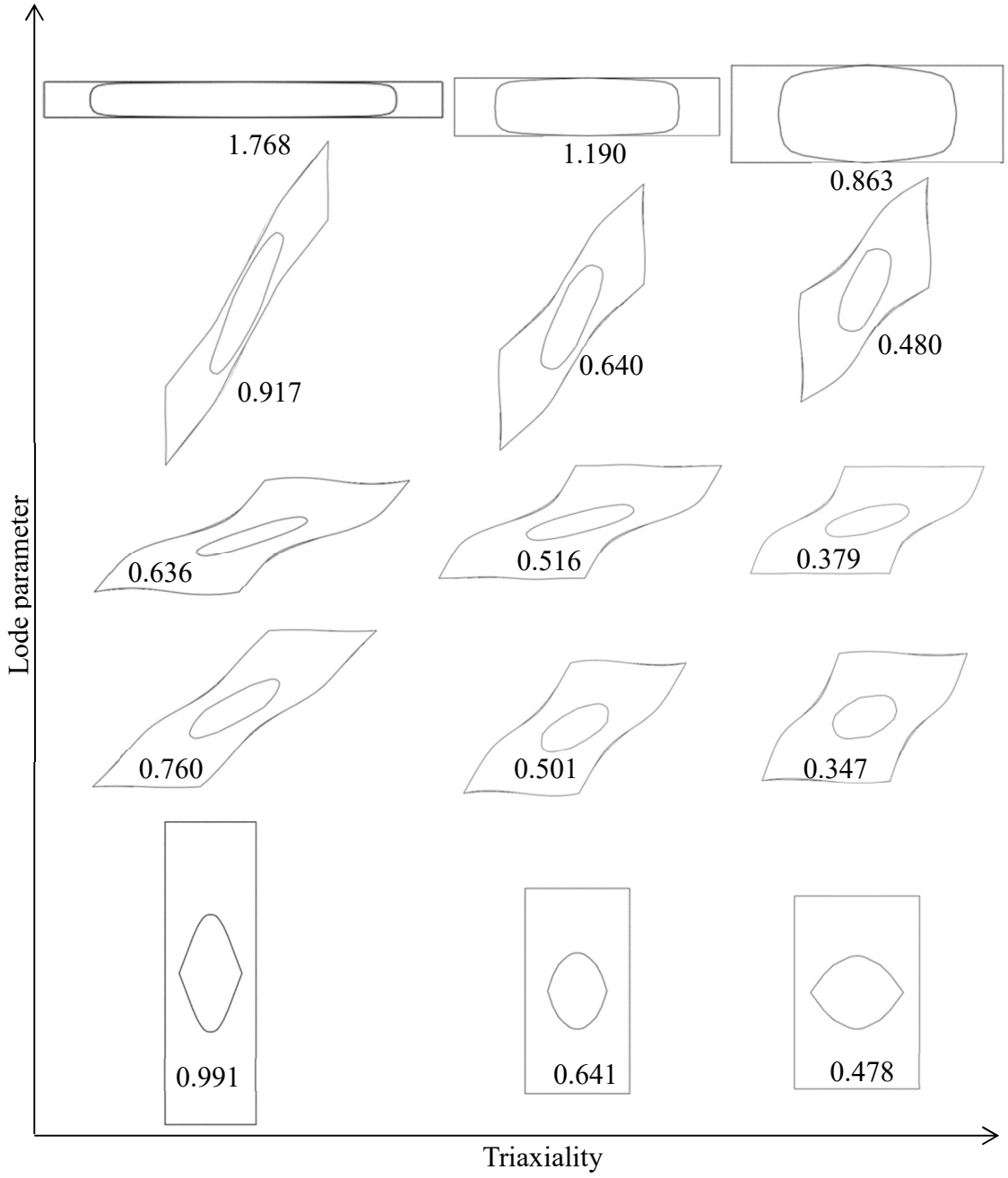

Figure 3.24. Deformed void shape in the inside layer under various stress states (T = 0.8, 1, 1.2, and μ = -1, -0.5, 0, 0.5, 1)

3.3.5.2 Material failure due to void shearing

Since the pioneer works of McClintock (1968) and Rice and Tracey (1969), a significant amount of research has been directed toward void growth modeling while modeling material failure due to void shearing has received less attention. The proposed unit cell model allows for analyzing material failure under low triaxiality, shear-dominated stress states. Fig. 3.25 shows the void shearing/rotation and shear band formation process for the $T = 0.5$ and $\mu = 0$ case. Here for illustration purpose, several unit cells are pieced together side-by-side. Figs. 3.25(a)-(c) show the deformed void shape and the plastic strain distribution at three stages, before the onset of localization, after the onset of localization, and when the plastic strain in the ligament becomes very large, respectively. Before localization, voids are stretched and rotated uniformly in the material. As the deformation continues, voids in the inside layer elongate and rotate more than voids in the outside layers, leading to localization. Eventually, the elongated voids in the inside layer become almost parallel to the localization plane as the ligament between neighboring voids is significantly reduced. After failure occurs, voids in the inside layer feature a needle-like spindle shape, thin and sharp at both ends and slightly expanded in the middle, while voids in the outside layer stop deforming.

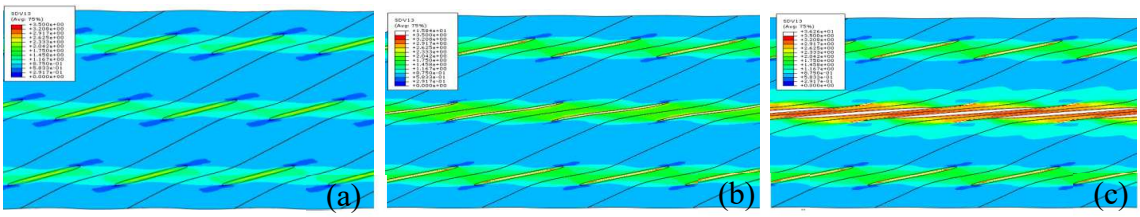

Figure 3.25. Deformed void shape and plastic strain distribution at three stages: (a) before the onset of localization, (b) after the onset of localization, (c) when the plastic strain in the ligament reaches ~3. Several unit cells are pieced together side-by-side for illustration purpose. The imposed stress state is governed by $T = 0.5$ and $\mu = 0$.

As the stress triaxiality increases, voids in the outside layer stretch and rotate less while voids in the inside layer have a more tendency to expand. Figs. 3.26(a-c) show the deformed void shape as the plastic strain in the ligament reaches ~3 as T increases from 0.5 to and 1. For all three cases, $\mu = 0$.

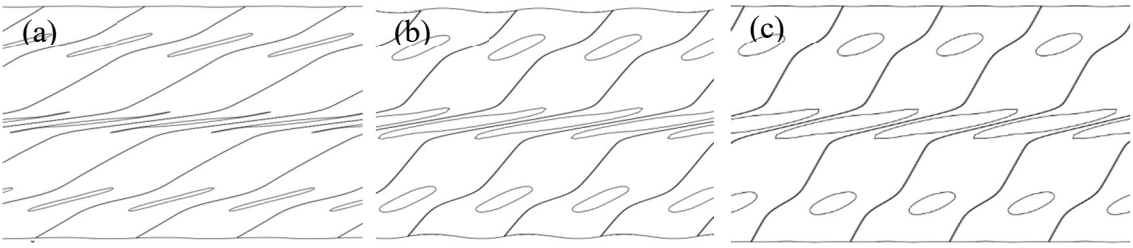

Figure 3.26. Deformed void shape for (a) $T = 0.5$, (b) $T = 0.8$, and (c) $T = 1$ cases. For all three cases, $\mu = 0$.

3.3.6 The effect of the orientation of the localization plane

In the unit cell model presented above, the orientation of the localization plan is predefined. However, the orientation of the localization plane is influenced by the stress state subjected by the material. Barsoum and Faleskog (2011) studied the effect of the stress state and defined the orientation of the localization plane as the one which leads to a minimum failure strain at the given stress triaxiality and Lode parameter. Their results suggest that the Lode parameter has a strong effect on the orientation of the localization plane while the effect of the stress triaxiality is insignificant. Here we consider $T = 1$ with varying L values and follow the approach of Barsoum and Faleskog (2011). By varying the incline angle of the assumed localization plane, θ, different values of failure strain can be obtained for a given pair of T and μ values. Fig. 3.27 shows the failure strain vs. θ curves for different stress states. The red "●" on each curve represents the critical orientation, θ_c, which has the minimum failure strain. Clearly there are two sets of critical incline angles for the stress states considered, shown as the solid lines in Fig. 3.28. The dashed line in Fig. 3.28 represents a reference angle corresponding to the principal stress directions. For the stress state shown in Fig. 3.2, the X_1-direction is always a principal stress direction. This θ-angle is measured by rotating the X_2-X_3 plane so that the two coordinate axes align with the two principal directions. Clearly the two solid lines are symmetric about the dashed line, corresponding to opposite shear directions.

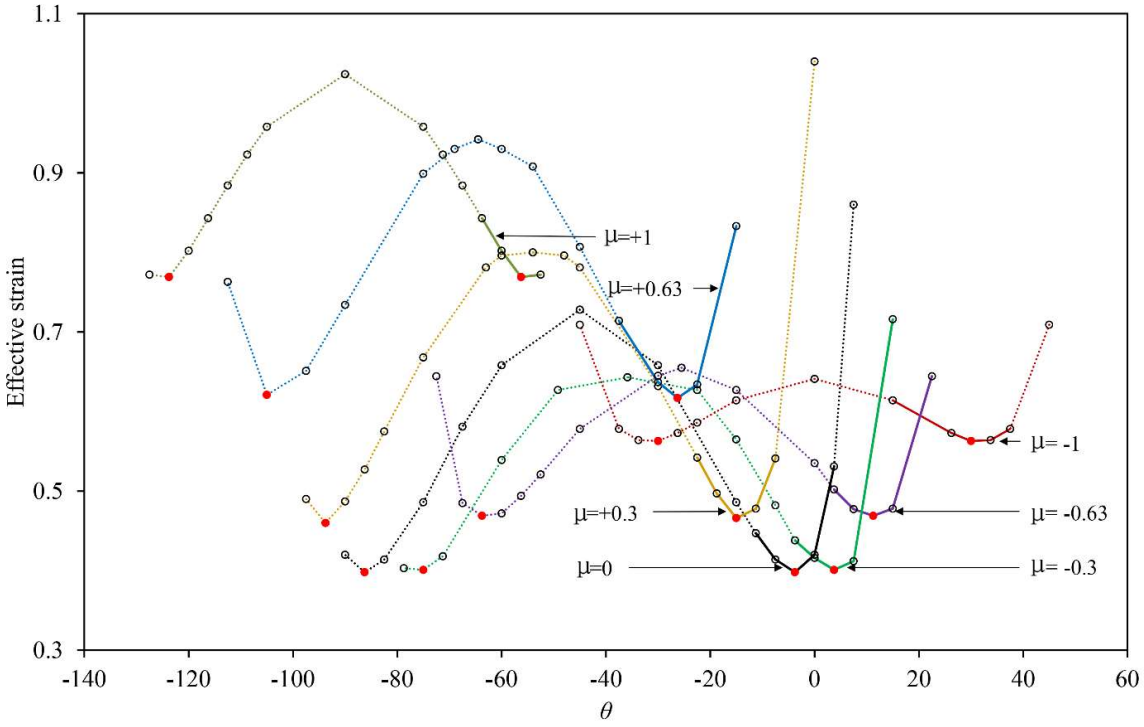

Figure 3.27. Failure strain vs. the inclination angle of the localization plane for different μ values with $T = 1$.

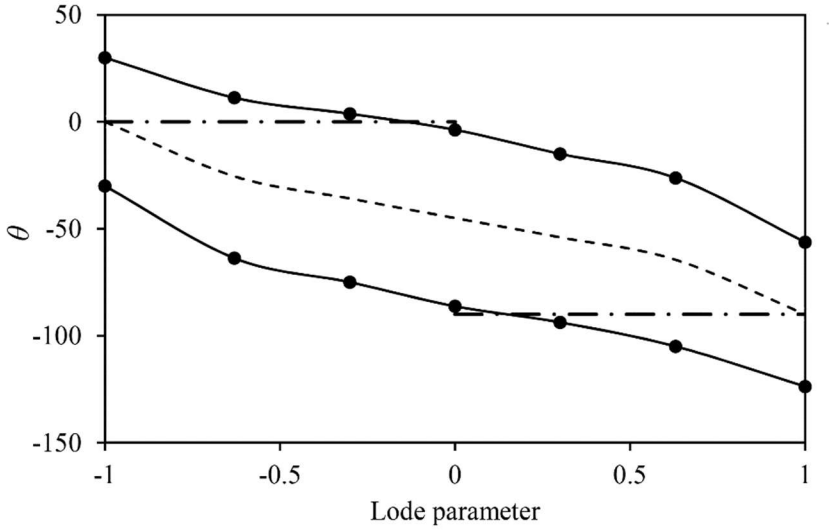

Figure 3.28. The inclination angle of the localization plane vs. Lode parameter. The critical inclination angle at each Lode parameter value is marked as solid circle.

In the unit cell analyses presented in previous sections, two unit cell models are considered for each stress state, one has three material units stacked along X_2 direction and the other has three material units stacked along X_3 direction. These two orientations are illustrated in Fig. 3.28 as dash-dotted lines. Fig. 3.28 shows that the difference between the determined critical orientation and the assumed localization orientation in the previous unit cell analyses is about 30º for the $\mu = \pm 1$ cases, where the difference is negligible when the Lode parameter is between -0.6 and 0.4. Since the main objectives of the present study are to introduce the three material unit, sandwiched unit cell model and to establish an easy-to-implement failure criterion, detailed analysis to determine the orientation of the localization plane at each stress state is not carried out. This will be considered in future studies.

3.4 Concluding Remarks

A unit cell model consisting of three void-containing material units is proposed to study ductile fracture by void coalescence and strain localization. The three material units are stacked in the direction normal to the plane where localization is set to take place. The boundary conditions are prescribed such that the macroscopic stress triaxiality and Lode parameter of the unit cell remain constant during the loading history. As deformation continues, localization takes place in the middle material unit, resulting in the material losing load carrying capacity. In the meantime, the other two material units undergo elastic recovering. Therefore, failure is said to have occurred once elastic unloading happens to the outside material units. With the sandwiched unit cell model, this failure criterion is very easy to implement in finite element analysis.

Analyses are conducted to study the effect of voids outside the localization band. It is found that for most cases voids in the outside layer do affect the stress state and void behavior in the inside layer and therefore should be accounted for in the unit cell model. Comparisons of present model with previous models are also conducted. The analysis results suggest that the criterion proposed by Barsoum and Faleskog (2007) can be considered equivalent to the failure criterion proposed in this paper if the proposed sandwiched unit cell model is adopted with $\eta > 10$. For $T = 2$, the energy-based method of Wong and Guo (2015) predicts similar failure strain at $\mu = \pm 1$, but a much larger failure strain at $\mu = 0$. In addition, the effect of the stress state on the orientation of the localization plane is investigated by considering $T = 1$ with varying μ values following the approach of Barsoum and Faleskog (2011).

A series of unit cell analyses are conducted for various macroscopic stress triaxialities and Lode parameters. The analysis results confirm that for a fixed Lode parameter, the failure strain decreases exponentially with the stress triaxiality and for a given stress triaxiality, it increases as μ approaches -1 and 1. It is found that the effect of the Lode parameter is more pronounced when the stress triaxiality is low. The analysis results also reveal the effect of the stress state on the deformed void shape within and near the localization band. In particular, under shear dominated conditions, voids tend to elongate and rotate, resulting in spindle-shaped voids aligning towards the direction of the localization plane.

CHAPTER IV

INVESTIGATION OF THE EFFECT OF HYDROGEN ON DUCTILE FRACTURE THROUGH AN UNIT CELL MODEL

4.1 Introduction

From the last chapter, we learned that the stress state identified by different Lode parameter and stress triaxiality can lead to various fracture mode and fracture strain for ductile material. In this chapter, we are going to investigate how the ductile process will be affected when the matrix material undergoes plastic softening introduced by hydrogen diffused in metal.

Hydrogen has an atomic structure of one proton and a single electron and is, in its natural state, a diatomic molecular gas, H_2. The di-atomic hydrogen molecule is too large to enter the surface of a solid metal, unless dissociated into single atoms by electrochemical or chemisorption process. Nevertheless, molecular hydrogen gas can also readily enter a molten metal surface, often added accidentally as water contained in fluxes, mold dressings, and alloying additions, dissociating into the mono-atomic form on dissolution, and remaining as a mono-atomic solute on solidification. After dissolved in metal, hydrogen remains either at normal interstitial lattice (NILS) and is relatively mobile at ambient temperature or trapped into trapping sites such as dislocations that are readily available in the crystal or newly generated by plastic straining. When it is so trapped in dislocations, one of the observations is that the hydrogen atom will enhance the slip of dislocations by

reducing the barriers to dislocation motion as shown in Vlasov and Zaznoba (1999), and San Marchi et al. (2008) or reduces dislocation-dislocation interactions which facilitates planar slip and increase pile-up phenomena that leads to damage initiation as shown in Chateau et al. (2002). As per dislocation theory of plastic deformation, we consider the plastic deformation of metal as a homogenized representation of slip of dislocations (defects in crystal) occurs at atom-level. Therefore, mechanisms enhance the slip of dislocations will limit the ductility of material via the onset of extensive localized plasticity. This effect is called hydrogen enhanced localized plasticity (HELP) and can be modeled according to Birnbaum and Sofronis (1994).

A prerequisite to model the HELP effect is the accurate modeling of hydrogen transportation. Hydrogen transport in material has been found strongly influenced by the hydrostatic stress gradient and the plastic strain as shown in Johnson et al. (1958) and Troiano (1960). Thus the hydrogen transport equation is fully coupled with the elastic-plastic deformation. Sofronis and McMeeking (1989) proposed a hydrogen transport model which coupled diffusion with hydrostatic stress and plastic strain. Oh et al. (2010) implemented this coupled hydrogen transport model in the commercial finite element program ABAQUS via a user subroutine. A similar approach will be applied in this chapter to implement the hydrogen transportation.

Previous studies have discussed the effect of HELP through various approaches. Through detail and carefully performed experiments, Maier (1995) studied the effects of low activity hydrogen in a low alloy spheroidized steel and found that locally accumulated hydrogen can assist both void nucleation and void growth. To understand the effect of HELP under specific stress state, Liang et al. (2008) demonstrated that large amounts of

hydrogen trapped by dislocations have a strong effect on void coalescence through an axisymmetric unit cell containing a spherical void subject under different triaxiality values. Recently, Huang et al. (2018) has performed unit cell analysis considered the effect of Lode parameter and 3D shear deformation and has shown Lode parameter also has a significant influence on the ductile fracture in terms of void shape evolution and failure strain variation. However, the previous studies either omitted strain rate term in hydrogen diffusion equation such as Sofronis and McMeeking (1989) and Liang et al. (2008) or included the strain rate term, but the specifics of loading speed and steady state are not clearly discussed when applying to dimensionless unit cell model such as Huang et al. (2018). As the hydrogen diffusion requires low enough loading speed to reach steady state of hydrogen distribution between trapping site and NILS as shown in Taha and Sofronis (2001), and with unit cell assumption as dimensionless micromechanics model, the loading speed required to reach steady state in a micromechanics model, if not omitted in hydrogen diffusion governor equation, should not be determined arbitrarily. Therefore, in this chapter, we will first determine the loading speed to reach a steady state of hydrogen distribution, and then conduct a series of analysis using a unit cell model subject to stress states determined by various triaxiality and Lode parameter to investigate the effect of hydrogen on ductile fracture by its influence on the process of void growth and coalescence.

4.2 Hydrogen transportation

Dissolved in metal, hydrogen remains either at normal interstitial lattice or trapped into reversible trapping sites such as pre-exist or newly generated dislocations. Therefore, the total hydrogen concentration can be expressed as

$$C = C_N + C_T = \beta\theta_N N_N + \alpha\theta_T N_T \tag{4.1}$$

where:

C_N is the hydrogen concentration at NILS,

C_T is the hydrogen concentration at the trapping site,

α is the number of sites per trap,

β is the number of NILS per solvent atom,

θ_N is occupancy of NILS,

θ_T is occupancy of the trapping sites,

N_N is the number of solvent atoms per unit lattice volume,

N_T is trap density.

The two populations are assumed to be in equilibrium and the relationship between θ_N and θ_T can be described as in Oriani (1970)

$$\frac{\theta_T}{1-\theta_T} = \frac{\theta_N}{1-\theta_N}\exp\left(\frac{W_B}{R\Theta}\right) \tag{4.2}$$

where:

W_B is the binding energy of the trapping sites,

R is gas constant,

Θ is the absolute temperature.

The governing equation for hydrogen transport detailed in Oh et al. (2009) is written as

$$\frac{C_N + C_T(1-\theta_T)}{C_N}\frac{\partial C_T}{\partial t} - \nabla(D_N \nabla C_N) + \nabla\left(\frac{D_N C_N V_H}{R\Theta}\nabla\sigma_m\right) + \theta_T \frac{dN_T}{d\varepsilon_P}\frac{\partial \varepsilon_P}{\partial t} = 0 \tag{4.3}$$

where:

D_L is the hydrogen diffusion constant through NILS,

V_H is the partial molar volume of hydrogen,

σ_m is mean stress,

ε_p is plastic strain,

$\frac{\partial \varepsilon_p}{\partial t}$ is the plastic strain rate.

Oh et al. (2010) provided a relation between trap density and plastic strain

$$\log(N_T) = 23.26 - 2.33\exp(-5.5\varepsilon_p) \tag{4.4}$$

The total deformation rate consists of an elastic part, D^e, a plastic part, D^p and a part due to hydrogen-induced lattice deformation, D^h. The hydrogen-induced deformation rate can be expressed as Peisl (1978)

$$D_{ij}^h = \frac{d}{dt}\left\{\ln\left[1 + \frac{(c - c_0)\Delta v}{3\Omega}\right]\right\}\delta_{ij} \tag{4.5}$$

where:

c is the current total hydrogen concentration,

c_0 is initial hydrogen concentration,

Ω is the mean atomic volume of the host metal atom,

V_H is the partial molar volume of hydrogen in solution,

$\Delta\upsilon = V_H/N_A$,

N_A is the Avogadro's constant.

Previous studies of Birnbaum and Sofronis (1994) and Tabata and Birnbaum(1983) showed that the dissolved hydrogen in iron increases the mobility of dislocation, causing the local yield stress to decrease with the increase in hydrogen concentration. Liang et al. (2003) proposed a phenomenological model to describe the hydrogen effect on the local yield stress:

$$\sigma_{\mathrm{Y}}\left(\varepsilon_{\mathrm{p}}, c\right)=\sigma_0(c)\left(1+\frac{\varepsilon_{\mathrm{p}}}{\varepsilon_0}\right)^N \tag{4.6}$$

with

$$\sigma_0(c)=\begin{cases}\left\lfloor(\xi-1)\dfrac{c}{c_0}\right\rfloor\sigma_0 & \sigma_0(c)>\eta\sigma_0\\ \eta\sigma_0 & \sigma_0(c)\le\eta\sigma_0\end{cases} \tag{4.7}$$

where:

$\sigma_0(c)$ is the initial yield stress in the presence of hydrogen,

E is Young's modulus, and ξ is a softening parameter.

In the above equations, $\varepsilon_0 = \sigma_0/E$ with $\sigma_0 = \sigma_0(0)$ representing the initial yield in the absence of hydrogen and $\eta\sigma_0$ is the lowest possible value of the yield stress with η varying between 0 and 1, considering that in reality hydrogen cannot cause the yield stress to vanish.

The above models were implemented in ABAQUS via user subroutines UMATHT and UMAT. Although ABAQUS does not provide a user interface for solving the coupled hydrogen transport equation, it does provide a built-in program for heat transfer analysis and allows the user to define the thermal behavior of the material for transient heat transfer analysis. The analogous structure of the Fourier's equation of thermal conduction and the hydrogen transport equation makes it possible to implement the hydrogen diffusion model in ABAQUS, where a UMATHT subroutine is used to match variables of the governing equations for heat transfer analysis with those for hydrogen diffusion.

4.3 Unit cell model

Experimental evidence over several decades had demonstrated that highly localized ductile rupture process is the trigger of hydrogen-induced fracture. Specifically, Tabata and Birnbaum (1983) revealed that the hydrogen-enhanced ductile fracture process involves microvoid nucleation, growth and coalescence when observe the behavior of pre-existed

crack, Robertson, and Birnbaum (1986) find hydrogen assisted localization shear band presents in the process of void/crack formation in the metal nickel, and Hänninen et al. (1993) reported similar phenomenon in various types of steel. These experiments implicit or explicitly reported that hydrogen intensifies the ductile fracture process by softening of a particular region at the microstructure scale. As shown in the previous chapter, ductile fracture process without the effect of hydrogen is heavily affected by the stress state applied upon representative microstructure of material. Therefore, to consider effect of stress state, studies such as Liang et al. (2007), Ahn et al. (2007) naturally tried to address this issue through unit cell model analysis, because even in carefully designed experiments, the stress state on a local scale is very hard to control and monitor. With carefully prepared numerical model and detailed analysis, the unit cell studies above revealed the effect of HELP under various stress states differentiated by stress triaxiality. However, as demonstrated by Kim et al. (2004) and Bai and Wierzbicki (2008), the micromechanics of ductile fracture process is not only influenced by the stress triaxiality but also by the Lode parameter, and showing by Luo and Gao (2018), a three-layered unit cell model can further correct the previously ignored influence of deformation differential between localized material layer and its adjunct layer. In this section, for the sake of completeness, we will briefly introduce the three-layered unit cell model, which is capable of examining the effect of stress state characterized by both triaxiality and lode parameter from a multi-scale perspective when investigating the effect of hydrogen-enhanced localized plasticity.

4.3.1 Unit cell model formulation

Here a uniform distribution of spherical voids is considered and the ratio between the void diameter and the void spacing is taken as 0.2, resulting in an initial void volume

fraction of f_0 = 0.004189. To simulate flow localization into a band and consider the different deformation process experienced by the material inside and outside the band, Luo and Gao (2018) proposed a unit cell model consists three layers of material units. This unit cell model is capable of robustly determine the material failure strain and easy to implement in finite element analysis compare to previous models. Fig. 4.1 shows a typical ½-symmetric finite element mesh of this unit cell model with an initial size of $D_0 \times 6D_0 \times D_0$ containing three centered, spherical voids. Here the initial void radius is $R_1 = 0.2D_0$ in the middle material unit and $R_2 = 0.198D_0$ in the other two material units. Mesh difference between the middle material unit and the outside material units are carefully controlled as small as possible so that the mesh-introduced inhomogeneity is minimal. The mesh consists of 27,000 hybrid, 8-node thermally coupled hexahedral elements.

To study the behavior of the unit cell under various stress states, the stresses imposed on the unit cell should include both normal and shear components. Here the applied stress consists of three normal stress components and a shear stress component, the same as in Barsoum and Faleskog (2007), Dunand and Mohr (2014), Wong and Guo (2015), and Luo and Gao (2018). Fig. 4.2 illustrates the stress state imposed on the unit cell.

Let Σ_{ij} be the macroscopic Cauchy stress tensor and S_{ij} be the stress deviator, $S_{ij} = \Sigma_{ij} - \Sigma_m \delta_{ij}$, where δ_{ij} denotes the Kronecker delta, Σ_m represents the mean stress, $\Sigma_m = \Sigma_{ii}/3$, and the summation convention is adopted for repeated indices. The von Mises equivalent stress is defined as

$$\Sigma_e = \sqrt{3J_2} = \sqrt{\frac{3}{2} S_{ij} S_{ij}} \,. \tag{4.8}$$

The stress triaxiality is defined as the ratio between the mean stress and the von Mises equivalent stress, $T = \Sigma_m / \Sigma_e$, and the Lode parameter is defined as

$$\mu = \sqrt{3}\tan\left(\theta - \tfrac{\pi}{6}\right), \tag{4.9}$$

where:

θ denotes the Lode angle, with $\cos(3\varphi) = \frac{27J_3}{2\sigma_e^3}$ and $J_3 = \frac{S_{ij}S_{jk}S_{ki}}{3}$.

The in-air material properties used in this study obeys a power-law hardening true stress-strain relation:

$$\begin{aligned} \sigma &= E\varepsilon \qquad \varepsilon \le \varepsilon_0 \,, \\ \sigma &= \sigma_0 \left(\frac{\varepsilon}{\varepsilon_0}\right)^N \quad \varepsilon > \varepsilon_0 \,. \end{aligned} \tag{4.10}$$

where σ_0 represents the yield stress in air of 400 MPa, E representing Young's modulus in air of 200 GPa, υ is the Poisson's ratio of 0.3, and the power-law straining hardening exponent n = 0.1. As mentioned in section 4.2, the following parameters are adopted from Sofronis and McMeeking (1989). The hydrogen lattice diffusion coefficient $D_L = 1.27\times10^{-2}$mm^2/s. The molar volume of iron $V_M = 7.116\times10^3$mm^3/mol and the lattice site density is $N_N = N_A / V_M = 8.46\times10^{19}$ solvent lattice atoms/mm^3. The number of interstitial lattice sites per solvent atom, β, is equal to 6 for BCC materials and number of sites per trap, α, is assumed to be 1 as mentioned by Hirth (1980). The partial molar volume of hydrogen in solid solution $V_H = 2.0\times10^3$ mm^3/mol. The initial hydrogen distribution in the material is assumed to be uniform with $C_L = C_0 = 2.084\times10^{21}$atoms/m^3.

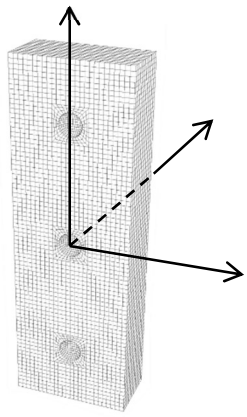

Figure 4.1. A typical ½-symmetric finite element mesh of the unit cell

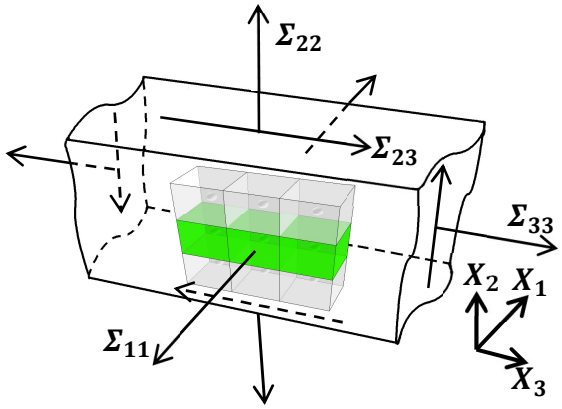

Figure 4.2. The stress state imposed on the unit cell

The displacement boundary conditions on the outer surfaces of the unit cell are prescribed such that the macroscopic stress triaxiality and Lode parameter of the unit cell are kept constant during the entire deformation history. This is realized by using the method described in Luo and Gao (2018). By varying the boundary conditions, different stress state can be imposed on the unit cell and the material failure criterion in terms of failure strain as a function of stress triaxiality and Lode parameter can be obtained.

4.3.2 Material failure criterion

Localization of plastic deformation within a narrow band is an important precursor to ductile fracture. Luo and Gao (2018) presented a numerical approach for determining the material failure criterion based on the response of material outside the localization layer. Ductile fracture (void coalescence) occurs when the effective strain of outside layer no longer increases, and the further accumulated plastic strain only localize into the localization layer. To apply this failure criterion, the measurement of effective strain is required to be carefully defined.

With the approach proposed and described in Luo and Gao (2018) used to apply the displacement-controlled loading, the finite element simulations are under displacement control. By taking the volume average of the local deformation gradient, the macroscopic deformation gradient can be given by the following expression

$$\overline{\boldsymbol{F}} = \frac{1}{V_0}\int_{S_0} \boldsymbol{x}\otimes\boldsymbol{N}\mathrm{d}S_0 \ . \tag{4.11}$$

where V_0 is the volume of the unit cell in the undeformed configuration, S_0 is the outer surface with the outward normal N, and x denotes the current position of a point on the deformed surface. Utilizing the boundary conditions described in Luo and Gao (2018), $\overline{\boldsymbol{F}}$ can be expressed as

$$\overline{\boldsymbol{F}} = \begin{bmatrix} \frac{D_0+\delta_1}{D_0} & 0 & 0 \\ 0 & \frac{D_0+\delta_2}{D_0} & 0 \\ 0 & \frac{\delta_4}{D_0} & \frac{D_0+\delta_3}{D_0} \end{bmatrix}. \tag{4.12}$$

while the macroscopic deformation gradient of a material unit is

$$\overline{\boldsymbol{F}}_m = \begin{bmatrix} \frac{D_0+\delta_1}{D_0} & 0 & 0 \\ 0 & \frac{D_0+\bar{\delta}_2}{D_0} & 0 \\ 0 & \frac{\bar{\delta}_4}{D_0} & \frac{D_0+\delta_3}{D_0} \end{bmatrix}, \tag{4.13}$$

Where the displacement measures δi is adopted from overall unit cell boundary conditions and $\bar{\delta}_2 = \int_{X_2=X_2^*} u_2\mathrm{d}S_0 - \int_{X_2=X_2^*-2D_0} u_2\mathrm{d}S_0$ and $\bar{\delta}_4 = \int_{X_2=X_2^*} u_3\mathrm{d}S_0 - \int_{X_2=X_2^*-2D_0} u_3\mathrm{d}S_0$ are displacement measures for individual material unit, in which $X_2^* = 3D_0$ for the top material unit, and $X_2^* = D_0$ for the middle material unit.

For non-singular deformation gradient **F**, polar decomposition can be performed

$$\boldsymbol{F} = \boldsymbol{RU} = \boldsymbol{VR}, \tag{4.14}$$

where $\boldsymbol{R}$ is an orthogonal rotation tensor, and $\boldsymbol{U}$ and $\boldsymbol{V}$ are symmetric stretch tensors. The left Cauchy-Green deformation tensor is defined as

$$\boldsymbol{B}^{-1} = (\boldsymbol{F}^{-1})^T\boldsymbol{F}^{-1} = (\boldsymbol{V}^{-1})^T\boldsymbol{V}^{-1} = (\boldsymbol{V}^{-1})^2. \tag{4.15}$$

The true strain can now be written in terms of $\boldsymbol{V}$ as

$$\boldsymbol{\varepsilon} = -\frac{1}{2}\ln\boldsymbol{B}^{-1} = -\frac{1}{2}\ln(\boldsymbol{V}^{-1})^2 = \ln\boldsymbol{V}. \tag{4.16}$$

The stretch tensor $\boldsymbol{V}$ can be expressed in term of its eigenvalues and eigenvectors as

$$\boldsymbol{V} = \sum_{i=1}^{3}\lambda_i\boldsymbol{n}_i\otimes\boldsymbol{n}_i, \tag{4.17}$$

where λ_i ($i = 1, 2, 3$) are eigenvalues of $\boldsymbol{V}$ and $\boldsymbol{n}_i$ ($i = 1, 2, 3$) are corresponding eigenvectors.

For a material unit, the macroscopic deformation gradient is given by Eq. (4.13), and the corresponding principal stretches are

$$\begin{aligned}
\lambda_1 &= \frac{\sqrt{2{D_0}^2+{\bar{\delta}_2}^2+{\delta_3}^2+2D_0(\bar{\delta}_2+\delta_3)+{\bar{\delta}_4}^2+\sqrt{\left((\bar{\delta}_2-\delta_3)^2+{\bar{\delta}_4}^2\right)\left((2D_0+\bar{\delta}_2+\delta_3)^2+{\bar{\delta}_4}^2\right)}}}{\sqrt{2}D_0},\\
\lambda_2 &= \frac{(D_0+\delta_1)}{D_0},\\
\lambda_3 &= \frac{\sqrt{2{D_0}^2+{\bar{\delta}_2}^2+{\delta_3}^2+2D_0(\bar{\delta}_2+\delta_3)+{\bar{\delta}_4}^2-\sqrt{\left((\bar{\delta}_2-\delta_3)^2+{\bar{\delta}_4}^2\right)\left((2D_0+\bar{\delta}_2+\delta_3)^2+{\bar{\delta}_4}^2\right)}}}{\sqrt{2}D_0},
\end{aligned} \tag{4.18}$$

and therefore, the principal logarithmic strains are

$$\begin{aligned}
\varepsilon_1 &= \ln\lambda_1,\\
\varepsilon_2 &= \ln\lambda_2,\\
\varepsilon_3 &= \ln\lambda_3.
\end{aligned} \tag{4.19}$$

Finally, the effective strain can be calculated as

$$\varepsilon_e = \sqrt{\frac{2}{3}((\varepsilon_1 - \varepsilon_m)^2 + (\varepsilon_2 - \varepsilon_m)^2 + (\varepsilon_3 - \varepsilon_m)^2)}, \tag{4.20}$$

where $\varepsilon_m = \frac{(\varepsilon_1+\varepsilon_2+\varepsilon_3)}{3}$.

Similarly, the macroscopic effective strain of the whole unit cell can be calculated using the principal stretches given by Eq. (4.21), corresponding to the macroscopic deformation gradient of the unit cell defined by Eq. (4.12)

$$\lambda_1 = \frac{\sqrt{2{D_0}^2+{\delta_2}^2+{\delta_3}^2+2D_0(\delta_2+\delta_3)+{\delta_4}^2+\sqrt{((\delta_2-\delta_3)^2+{\delta_4}^2)((2D_0+\delta_2+\delta_3)^2+{\delta_4}^2)}}}{\sqrt{2}D_0},$$

$$\lambda_2 = \frac{(D_0+\delta_1)}{D_0}, \tag{4.21}$$

$$\lambda_3 = \frac{\sqrt{2{D_0}^2+{\delta_2}^2+{\delta_3}^2+2D_0(\delta_2+\delta_3)+{\delta_4}^2-\sqrt{((\delta_2-\delta_3)^2+{\delta_4}^2)((2D_0+\delta_2+\delta_3)^2+{\delta_4}^2)}}}{\sqrt{2}D_0}.$$

With effective strain measure on the unit cell and individual material unit carefully defined, the material failure strain of the unit cell indicated by the moment when outside material unit reaches its maximum strain value can be easily applied.

4.4 HELP effect under different loading speed

The hydrogen diffusion in metal is not instantaneously and hydrogen requires time to propagation. If the loading speed is fast, the trap generation is ahead of hydrogen diffusion, therefore the effect of HELP may only partially apply due to the lower than saturate concentration of hydrogen in the trapping site. However, if the loading speed is slow such that the hydrogen distribution reaches a steady state, the effect of HELP can reach its maximum. In this part, we will investigate the effect of loading speed on HELP through unit cell model.

Here we define the loading speed as the effective strain per diffusion time at the instant of determined material failure by the criterion introduced in the last part. Loading speed A, B, C, D, E, and F is each faster by one magnitude with A the slowest and F the fastest. Here we take the response of unit cell model undergoing the stress state of T=1 and μ=0 with different loading speed as an example. Fig. 4.3 is the curves of macroscopic stress-strain response of the overall unit cell model, and Fig 4.4 shows the void growth curve under different loading speed. Here f_0 represents the initial void volume fraction, f represents the current void volume fraction. All the curves in both Fig. 4.3 and Fig. 4.4 are cut off at material failure strain. As shown in Fig. 4.3 and Fig. 4.4, as the loading speed decrease, the failure strain and effective stress will decrease but will converge at a low enough loading speed, in this case, speed B. This indicates when the loading speed is lower than speed B, the diffusion time is long enough to saturate the trapping site, therefore considered a steady state. In the following chapter, the loading speed is carefully controlled lower than steady state loading speed and the results will only reflect the effect of HELP when diffusion time is long enough to saturate the trapping site. Furthermore, the stress-strain curve of cases with HELP is uniformly lower than the case without HELP for a certain value, that's due to the softening effect of initial hydrogen concentration.

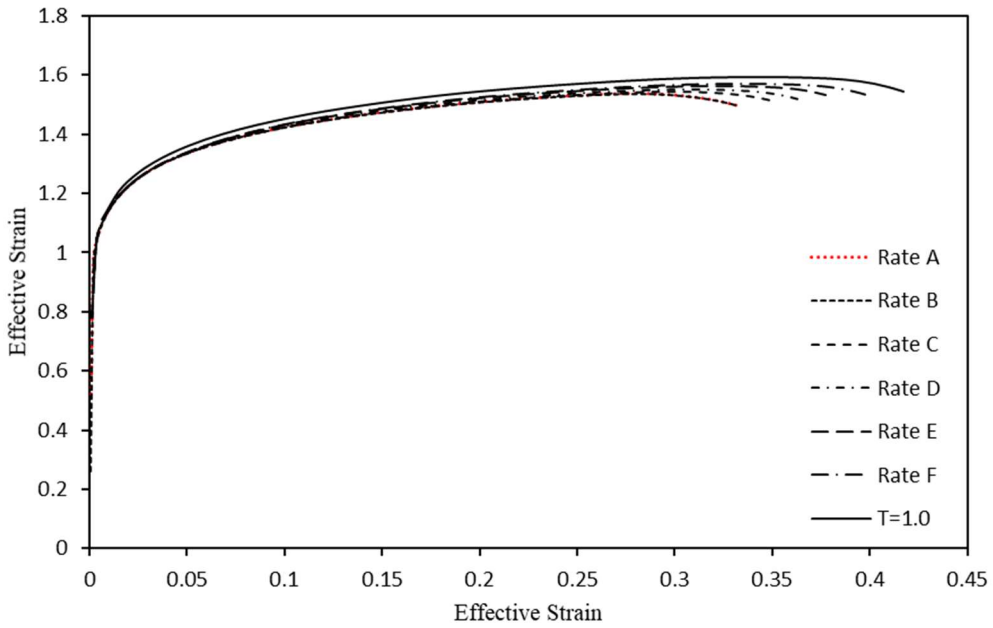

Figure 4.3. Stress-strain curve variation with different loading speed for the case undergo stress state of T=1.0, μ=0.0

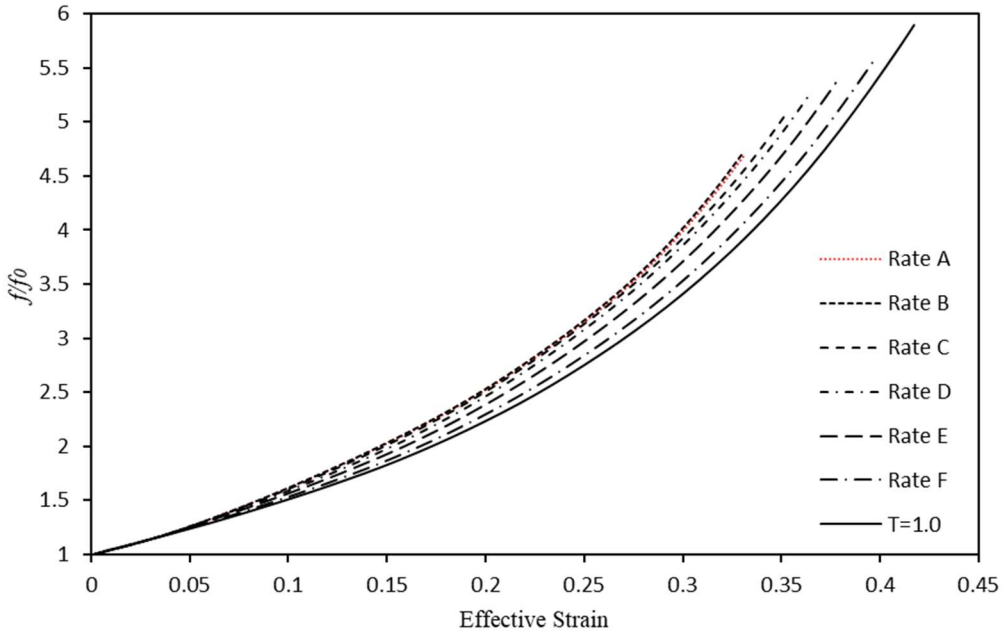

Figure 4.4. Void growth curve variation with different loading speed for the case undergo stress state of T=1.0, μ=0.0

4.5 HELP effect under different stress triaxialities

In the following, the HELP effect is systematically analyzed under various stress states. First, the Lode parameter is kept constant and different stress triaxialities are considered. It is well-known that the void growth rate is strongly influenced by the stress triaxiality as shown in Hancock and Mackenzie (1976) and Hancock and Brown (1983). Fig. 4.5 compares the void growth curve between cases with the effect of HELP and cases without, the curves are again cutoff at failure strain. Here letter "h" in the legends corresponds to the results with the HELP effect included. The considered stress triaxiality varies from T = 0.6 to T = 1.2 while the Lode parameter is kept as $\mu = 0$. As shown in Fig. 4.5, with or without HELP effect, in the considered triaxiality range, the higher stress triaxiality always results in higher void growth rate, and void growth accelerates as deformation increases. Comparing cases with and without the HELP in Fig. 4.5, the cases with HELP effect shows a higher void growth rate than the cases without HELP. Furthermore, void growth is significantly accelerated by the HELP effect for the high stress triaxiality case while the HELP effect on the void growth rate is less pronounced for the low stress triaxiality case.

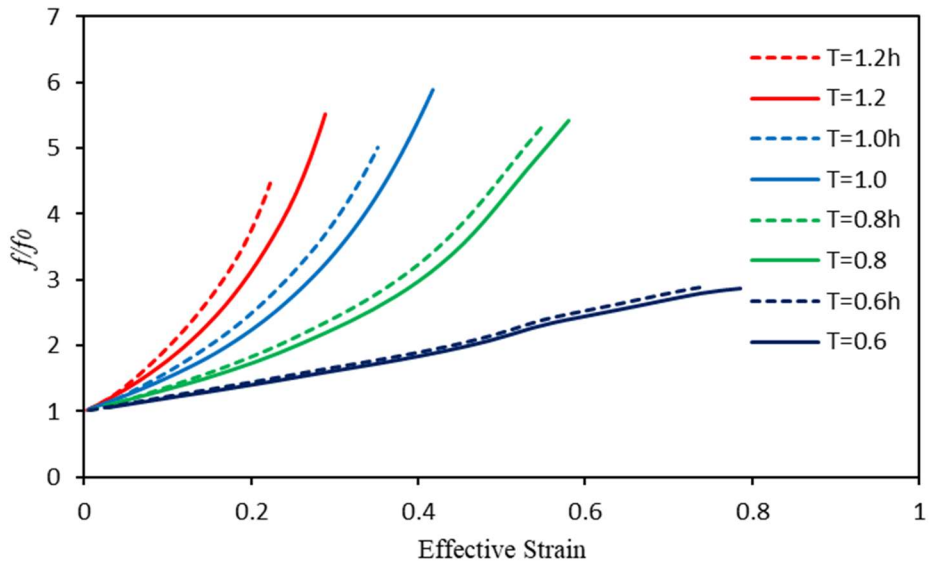

Figure 4.5. Curves of normalized void volume fraction vs. macroscopic effective strain of the unit cell model with and without HELP as the stress triaxiality varies from $T = 0.6$ to $T = 1.2$ while the Lode parameter is kept as $\mu = 0$.

Fig. 4.6 concludes the failure strain of cases with and without HELP for the above stress triaxiality range. The filled dots representing failure strain determined for cases with the effect of HELP while the circle dots representing those without. The results suggest that HELP has little influence on the failure strain when the stress triaxiality is low but has a more significant effect on the failure strain when the stress triaxiality is higher. For $\mu = 0$ and in the range of stress triaxiality of $T = 0.6$, 0.7,0.8,0.9,1.0,1.1, and 1.2, failure strain reduction by the effect of HELP is 96.5%,95.6%,94.3%,85.7%, 84.6% and 77.0%, respectively. As shown in Fig. 4.6, it is found that generally, the higher the void growth rate is, the more significant the HELP effect is on the ductility of the material.

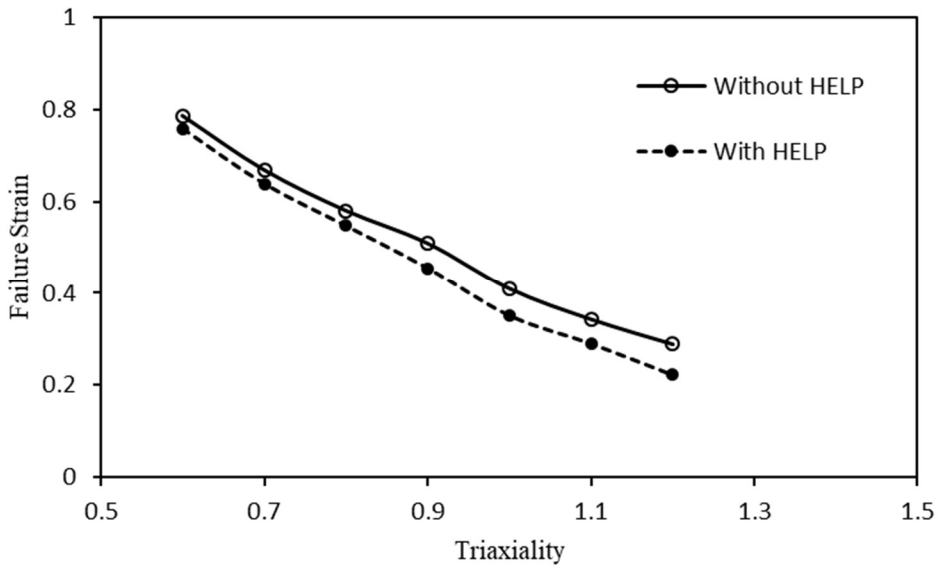

Figure 4.6. Variation of the failure strain with stress triaxiality with and without HELP.

The contours of specific distribution of key values such as Von Mises stress, plastic strain, and hydrogen concentration can help us explain the influence of stress triaxiality on HELP effect in detail. Two cases with the same Lode parameter, $\mu = 0$, but different stress triaxialities, T = 0.6 and T = 1.2, are compared. Fig. 4.7 and Fig. 4.8 shows the case of stress triaxiality T = 0.6 and Fig. 4.9 and Fig. 4.10 shows the case of stress triaxiality T = 1.2. Figs. 4.7 and 4.9 are the contours of von Mises stress, plastic strain and trapping hydrogen concentration when the macroscopic effective strain of the middle material unit is equal to 0.5 for T=0.6 and 0.165 for T=1.2. Fig. 4.8 and Fig.4.10 show the contour of plastic strain when the macroscopic effective strain of overall unit cell model is equal to 0.72 for T=0.6 and 0.2 for T=1.2.

Undergoing the loading of stress state T=0.6 without the HELP effect, the plastic strain is observed localizing into a band with a thickness comparable to the size of the void and more concentrate near the void, Fig. 4.7(a). The higher plastic strain causes more

hydrogen trapped into this area, Fig. 4.7(c). With the HELP effect the plastic strain localization and hydrogen trapping become more significant, Fig. 4.7(b) and Fig. 4.7 (d). The phenomenon of trapped hydrogen accumulating in the area of high plastic strain is also reported in the work by Taha and Sofronis (2001). The higher concentration of trapped hydrogen in the area near the void surface, Fig. 4.7(d), in turn works with the HELP effect resulting in more pronounced material softening (low Mises stress) in this region as shown in Fig. 4.7(f). Consequently, the void growth is accelerated, and the material failure strain is reduced. However, the softening effect brought by HELP is limited under lower triaxiality and therefore under a same macroscopic effective strain shortly before material failure, the unit cell model considered HELP and the one does not only show minor difference in terms of plastic strain and deformation as shown in Fig. 4.8.

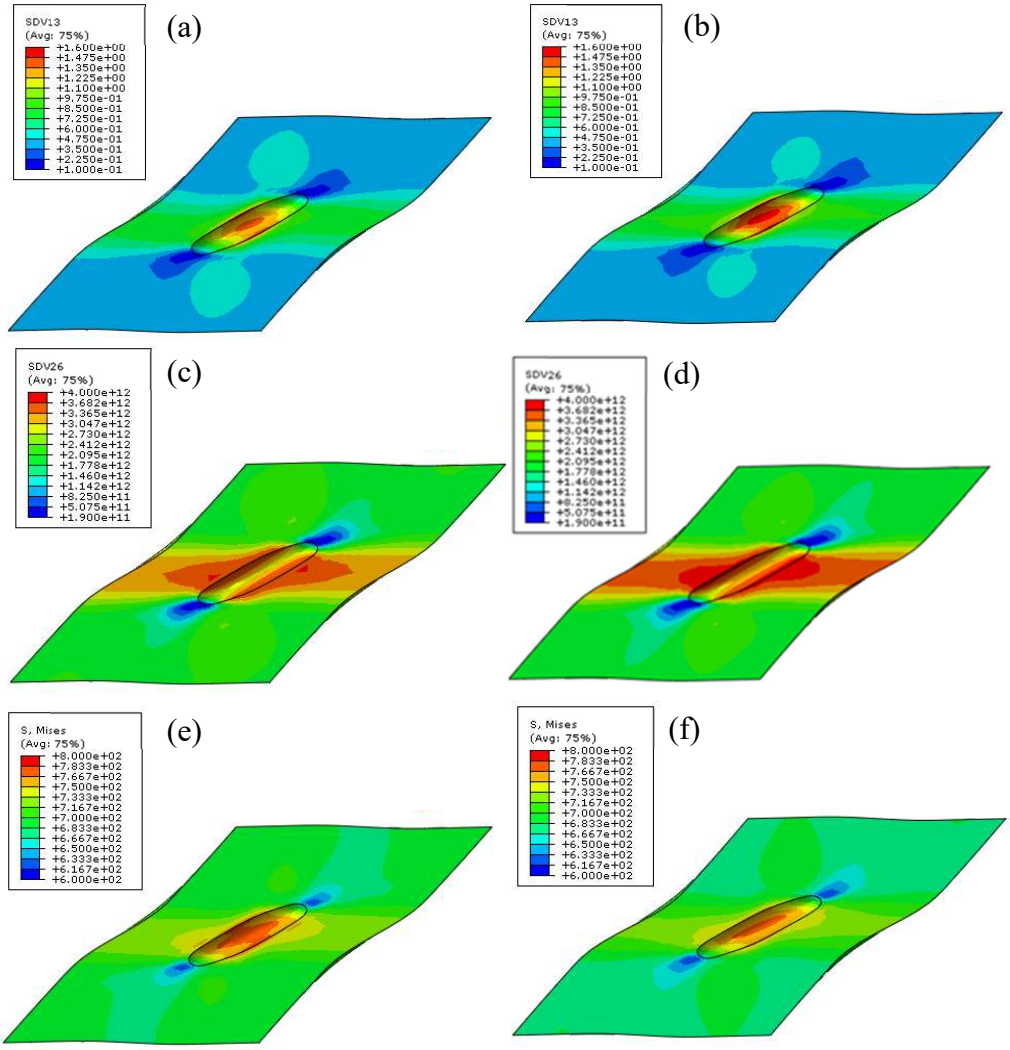

Figure 4.7. Contours of plastic strain (SDV13), trapping hydrogen concentration (SDV26) and von Mises stress when the macroscopic effective strain of the inside layer material unit is equal to 0.5 for the case of low stress triaxiality ($T = 0.6$) and Lode parameter μ=0: (a) plastic strain without HELP effect, (b) plastic strain with HELP effect, (c) trapping hydrogen concentration without HELP effect, (d) trapping hydrogen concentration with HELP effect, (e) von Mises stress without HELP effect, (f) von Mises stress with HELP effect.

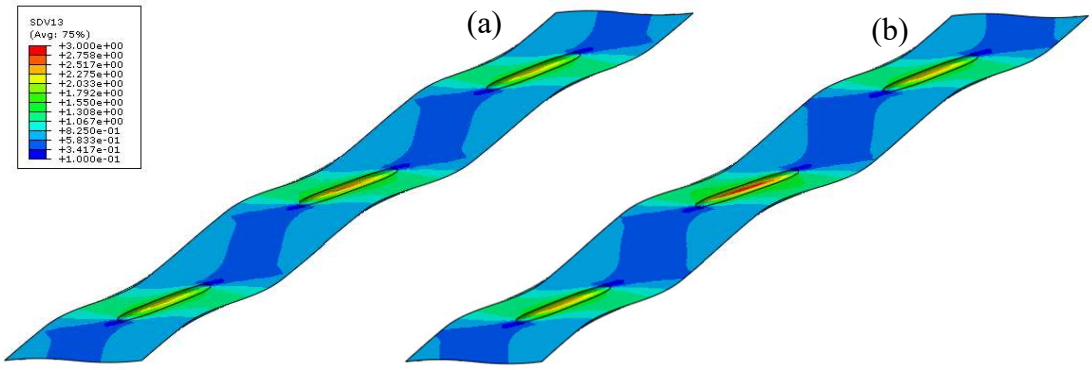

Figure 4.8. Contours of the plastic strain for the case of stress triaxiality $T = 0.6$ and Lode parameter $\mu = 0.0$ at same macroscopic effective strain value of 0.7: (a) plastic strain without HELP effect, (b) plastic strain with HELP effect

The results of plastic strain localization and hydrogen trapping into a band are similar but much more significantly concentrated to the area near the void surface for the stress triaxiality T = 1.2 case, Figs. 4.9(a-d). The significantly higher concentration of trapped hydrogen in the area near the void surface works with the HELP effect and resulting in dramatic material softening in this region, Fig. 4.9(f). Consequently, the void growth is greatly accelerated, and the material failure strain is reduced significantly. As a result, as shown in Fig. 4.10, under a same macroscopic effective strain of 0.2 the HELP case is showing strain localization into the middle layer and will then lead to material failure, while the case without HELP is still showing nearly uniform strain accumulation between outside and inside layer material because the load carrying capacity of the middle layer material did not reduce by HELP. The effect of HELP is therefore more significant when the stress triaxiality is higher compare T=0.6 and T=1.2 cases.

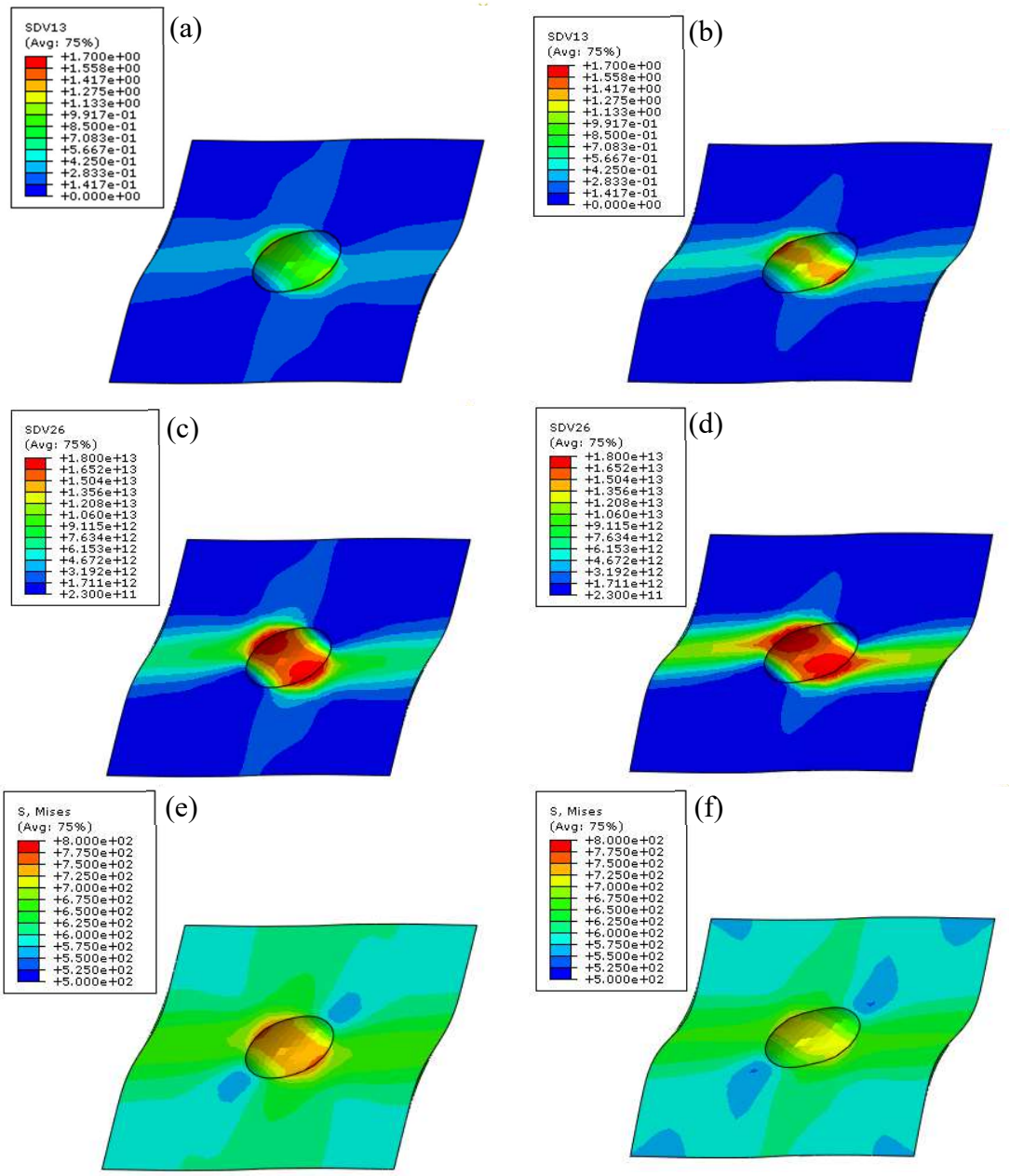

Figure 4.9. Contours of plastic strain, trapping hydrogen concentration and von Mises stress when the macroscopic effective strain of the inside layer material unit is equal to 0.164 for the case of low stress triaxiality (T = 1.2) and Lode parameter μ=0: (a) plastic strain without HELP effect, (b) plastic strain with HELP effect, (c) trapping hydrogen concentration without HELP effect, (d) trapping hydrogen concentration with HELP effect, (e) von Mises stress without HELP effect, (f) von Mises stress with HELP effect.

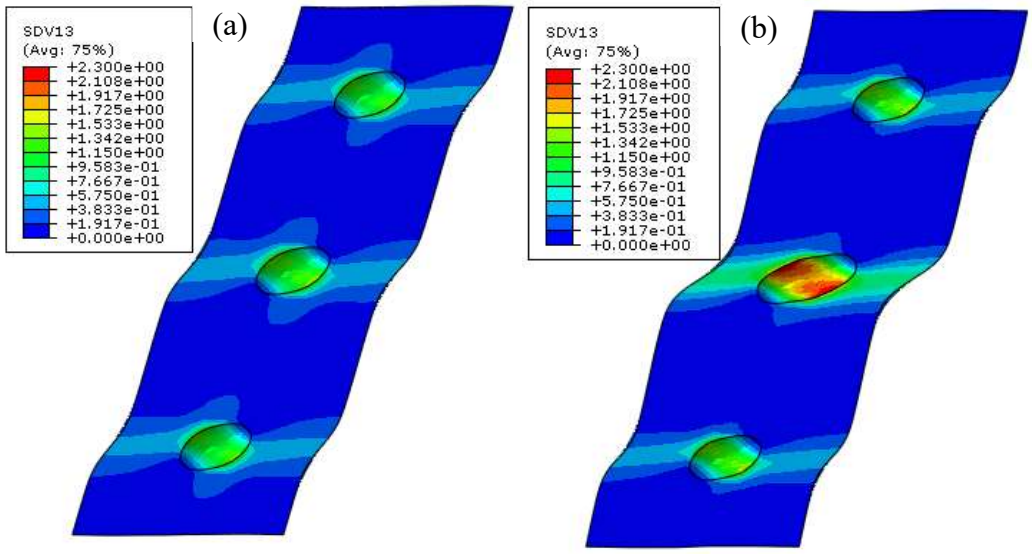

Figure 4.10. Contours of the plastic strain for the case of stress triaxiality $T = 1.2$ and Lode parameter $\mu = 0.0$ at same macroscopic effective strain value of 0.2: (a) plastic strain without HELP effect, (b) plastic strain with HELP effect

4.6 HELP effect under different Lode parameters

In this section, the stress triaxiality is kept at $T = 1.0$ and different Lode parameters of from μ = -1 to μ = 0.63 are considered. Fig. 4.11 compares the void growth curve between cases with the effect of HELP and cases without, the curves are again cutoff at failure strain. The plotted curves of μ =0, μ =0.5 and μ =0.63 with triaxiality kept as T = 1.0 showing that a higher void growth rate is more pronounced in with HELP cases than the cases without HELP. Furthermore, void growth is significantly accelerated by the HELP effect for the μ =0 case while the HELP effect on the void growth rate is less

pronounced for cases with μ values towards 0.63. Although the cases of μ = -1 to μ =0 is omitted in this figure to avoid curve overlapping, but a similar trend of void growth rate higher at 0 and lower towards -1 is also observed.

Fig. 4.12 shows the failure strain determined varying with different Lode parameter. The filled dots representing failure strain determined for cases with the effect of HELP while the circle dots representing those without. Similar with the HELP effect on void growth rate, the effect of HELP on failure strain reduction is most pronounced around L=0 and become less significant towards μ = 0.63 and μ = -1. For T = 1.0 and in the range of Lode parameter of μ = -1, -0.63, -0.3,0,0.3, 0.5, and 0.63, failure strain reduction by the effect of HELP is 96.4%,95.5%,89.0%,85.7%, 94.7%,98.6% and 99.0%, respectively.

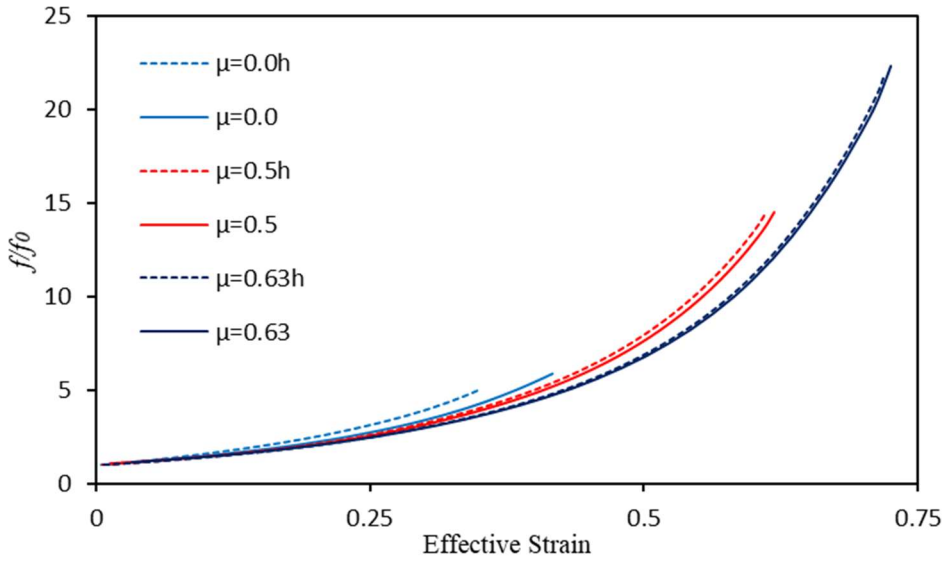

Figure 4.11. Curves of normalized void volume fraction vs. macroscopic effective strain of the unit cell model with and without HELP as the Lode parameter varies from μ=0.0 to μ=0.63 while the Lode parameter is kept as T=1.0.

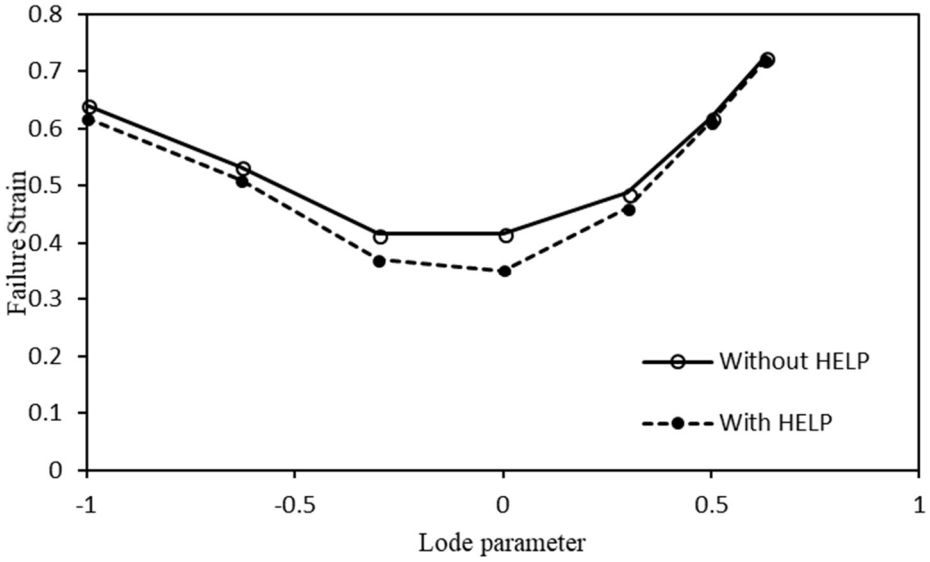

Figure 4.12. Variation of the failure strain with Lode parameter with and without HELP.

Two cases with the same stress triaxiality T=1.0 but different Lode parameters, μ = 0.0 and μ = 0.63, are compared. Fig. 4.13 and Fig. 4.14 are regarding the case of Lode parameter μ = 0.0 and Fig. 4.15 and Fig. 4.16 are regarding the case of μ = 0.63. Figs. 4.13 and 4.15 are the contours of von Mises stress, plastic strain and trapping hydrogen concentration when the macroscopic effective strain of the middle material unit is equal to 0.215 for μ = 0.0 and 0.53 for μ = 0.63. Fig. 4.14 and Fig. 4.16 are the contours of plastic strain when the macroscopic effective strain of overall unit cell model is equal to 0.31 for μ = 0.0 and 0.675 for μ = 0.63.

The T=1.0 and μ = 0.0 case is comparable with T=1.2, μ = 0.0 case. The higher plastic strain localization in the area near the void surface attracts a higher concentration of trapped hydrogen, and with the HELP effect resulting in more pronounced material

softening in this region. Consequently, at the same macroscopic effective strain of 0.31, the with HELP case exhibits larger void and more intense plastic strain localization compare to the without HELP case as shown in Fig. 4.14. As shown in Fig. 4.15, the softening effect brought by HELP is limited in case T=1.0 and $\mu = 0.63$ and only occurs at a very small portion of void surface. Therefore, under a same macroscopic effective strain of 0.675 shortly before material failure, the unit cell model with and without HELP only showed minor difference in terms of plastic strain and deformation as shown in Fig. 4.16.

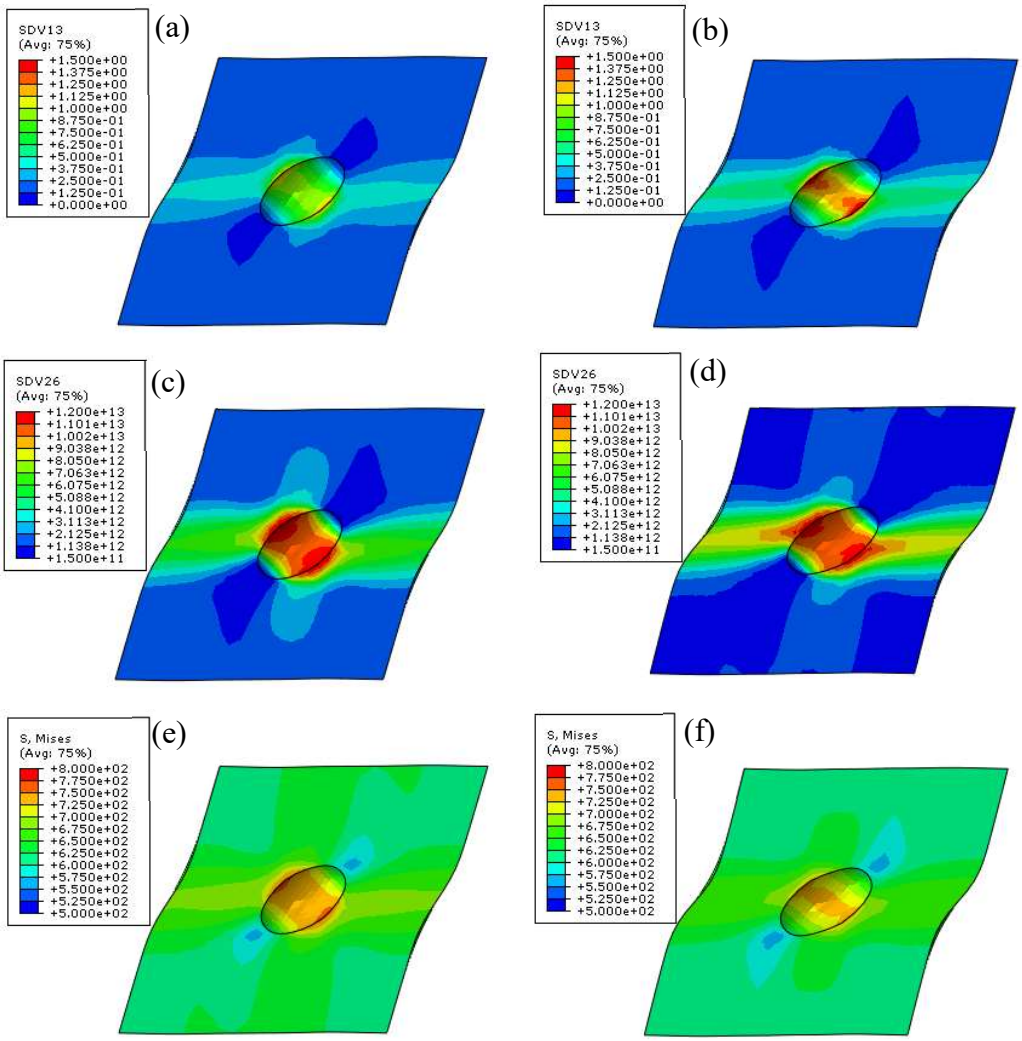

Figure 4.13. Contours of plastic strain, trapping hydrogen concentration and von Mises stress when the macroscopic effective strain of the inside layer material unit is equal to 0.215 for the case of triaxiality $T = 1.0$ and Lode parameter $\mu=0.0$: (a) plastic strain without HELP effect, (b) plastic strain with HELP effect, (c) trapping hydrogen concentration without HELP effect, (d) trapping hydrogen concentration with HELP effect, (e) von Mises stress without HELP effect, (f) von Mises stress with HELP effect.

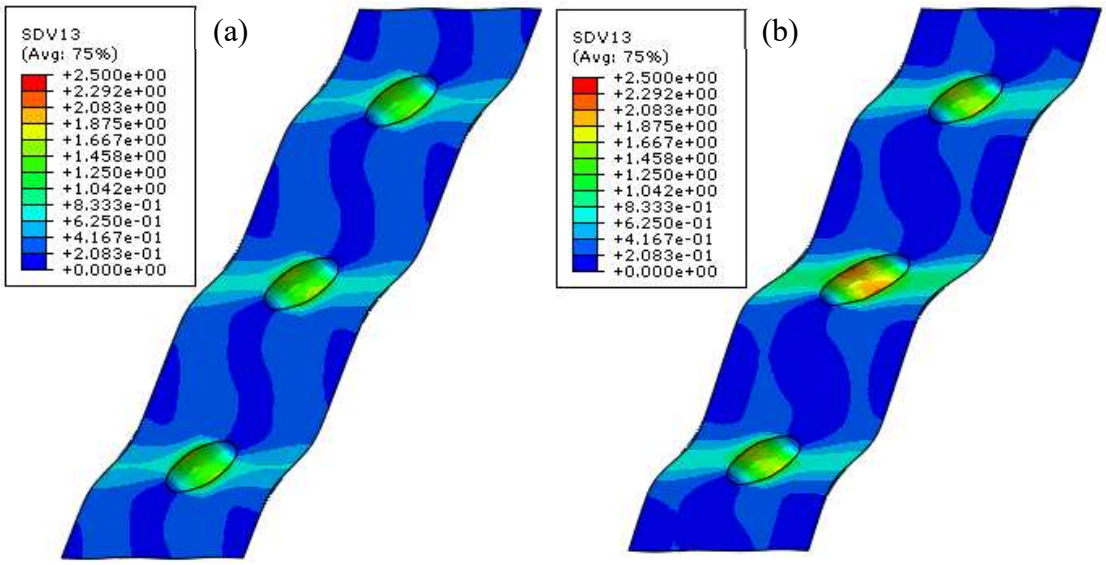

Figure 4.14. Contours of the plastic strain for the case of stress triaxiality $T = 1.0$ and Lode parameter $\mu = 0.0$ at same macroscopic effective strain value of 0.31: (a) plastic strain without HELP effect, (b) plastic strain with HELP effect

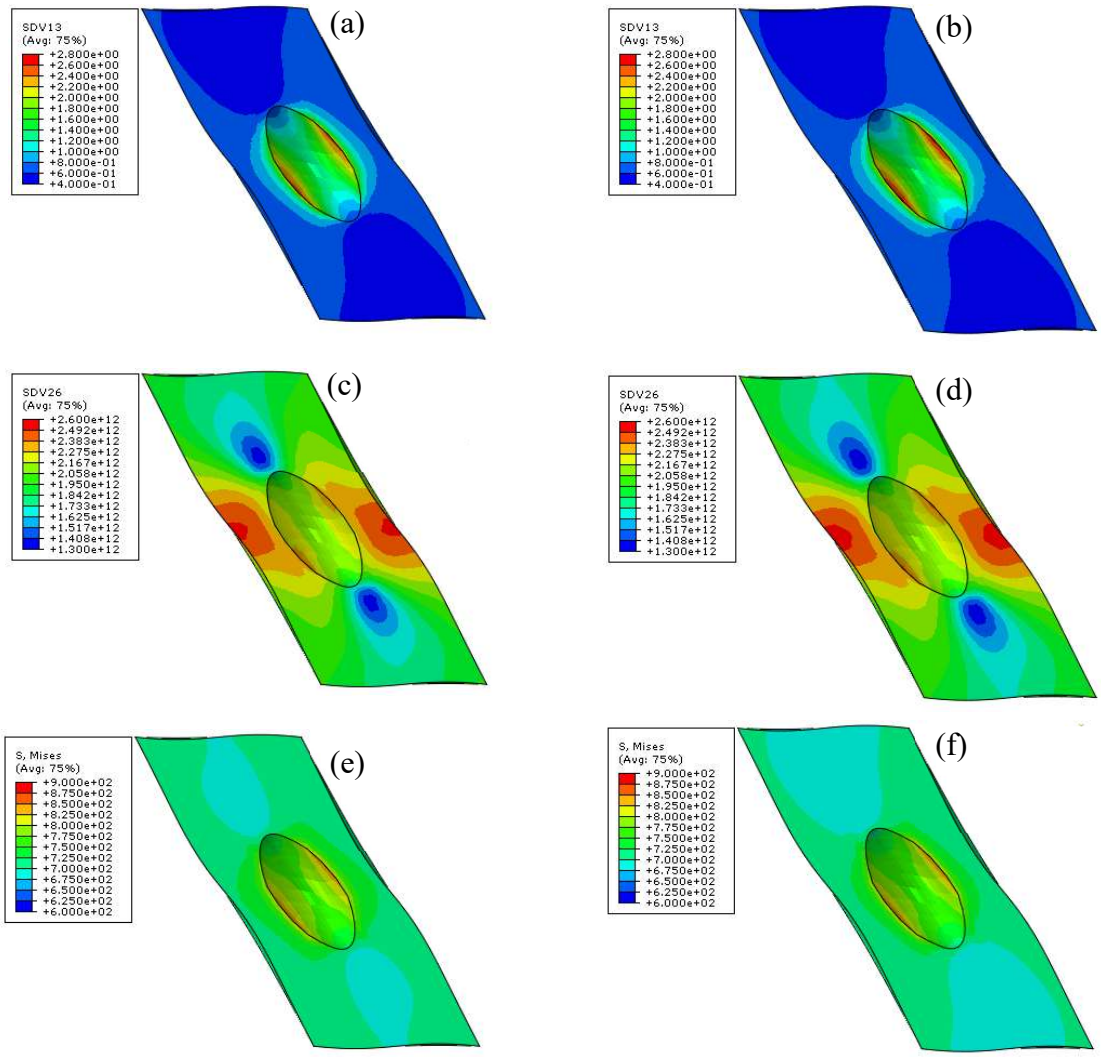

Figure 4.15. Contours of plastic strain, trapping hydrogen concentration and von Mises stress when the macroscopic effective strain of the inside layer material unit is equal to 0.53 for the case of triaxiality T = 1.0 and Lode parameter μ=0.63: (a) plastic strain without HELP effect, (b) plastic strain with HELP effect, (c) trapping hydrogen concentration without HELP effect, (d) trapping hydrogen concentration with HELP effect, (e) von Mises stress without HELP effect, (f) von Mises stress with HELP effect.

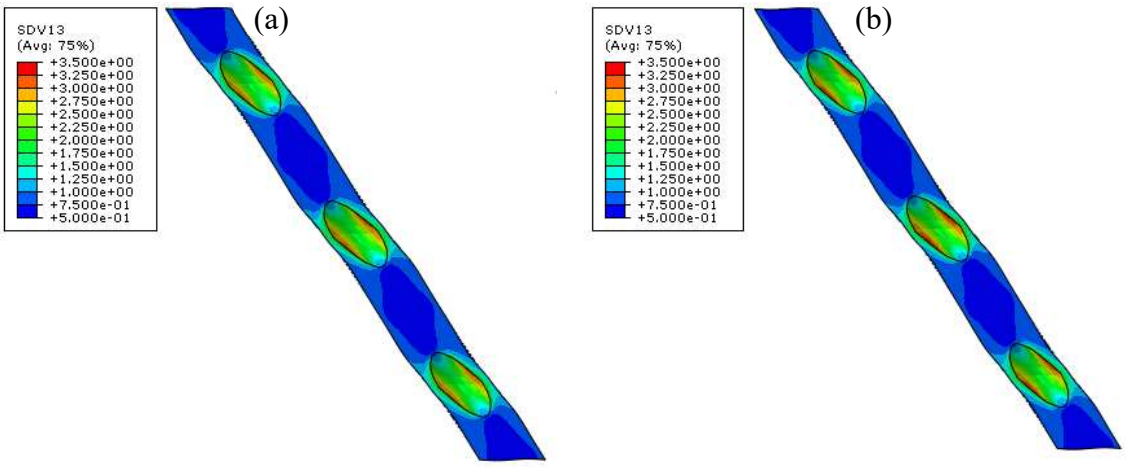

Figure 4.16. Contours of the plastic strain for the case of stress triaxiality $T = 1.0$ and Lode parameter $\mu = 0.63$ at same macroscopic effective strain value of 0.675: (a) plastic strain without HELP effect, (b) plastic strain with HELP effect

4.7 Discussion

From the results present in last two parts, we found that the effect of HELP on failure strain is more pronounced when the void growth process is accelerated by HELP despite the void size at material failure. For example, for a similar material failure void size, the more void growth is accelerated, the more failure strain reduction is observed in T=1.2,1.0 and 0.8 cases with μ=0. Also, with very different material failure void size between T=0.6, μ=0 and T=1.0,μ=0.63, because the void growth rate in both cases are insignificantly accelerated, the reduction on failure strain are both minimums compared with other cases in their group. And the cases with higher void growth rate such as T=1.2, μ=0, and T=1.0,μ=0, all exhibit more pronounced trapped hydrogen concentration and highly localized strain on the void surface are compare to their peers as shown in Figs. 4.7,

4.9, 4.13, 4.15. The hydrostatic stress gradient and plastic strain are two factors that affect trapped hydrogen concentration, the former rises hydrogen concentration in the NILS and the latter generates new trapping sites for hydrogen to fill. To investigate the effect of those two factors, we plot the hydrostatic stress, plastic strain and total hydrogen concentration contour of without HELP cases in Fig. 4.17. All the contours are captured at inside layer material units at a strain of 0.2, and Figs. 4.17(a-c), (d-f), and (g-i), are the invariant I_1=3× hydrostatic stress, plastic strain, and total hydrogen concentration contour for case T=0.6, μ=0, T=1.0, μ=0.63, and T=1.0, μ=0.

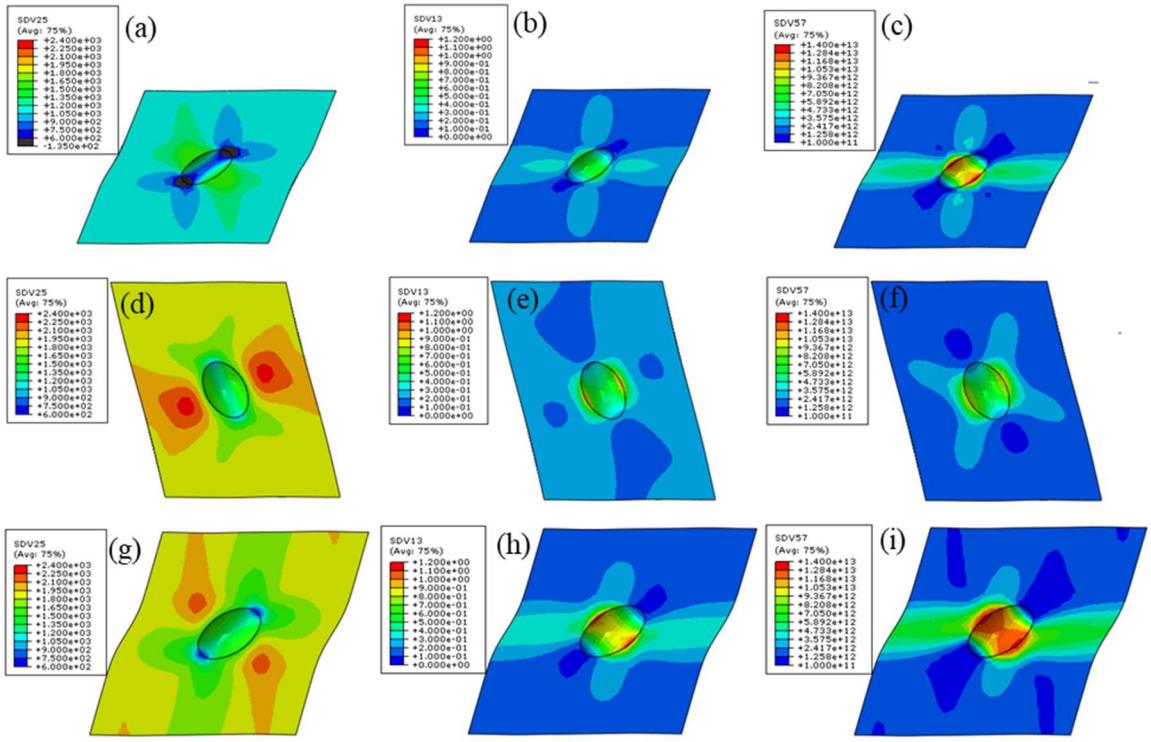

Figure. 4.17. The I_1 invariant, plastic strain, and total hydrogen concentration contours for stress states of T=0.6, μ=0: (a-c), T=1.0, μ=0.63: (d-f), and T=1.0, μ=0.0: (g-i).

As shown in Fig. 4.17, across the evaluated stress triaxialities and Lode parameters, the plastic strain distributions on the material unit always has more influence on the distribution of total hydrogen concentration compare to hydrostatic stress, especially at the area around the surface of voids. This phenomenon shows that in the studied cases, the effect of hydrostatic stress on rising hydrogen concentration by attracting hydrogen to NILS is less than the effect of plastic strain on rising hydrogen concentration achieved by generating new trapping sites.

Therefore, based on micromechanical evidence from the above-performed unit cell analysis, we can conclude that the effect of HELP is mainly depending on the plastic strain distribution within the representative material volume. Specifically, the region of adjunct to void surface is of most interest, with more plastic strain localizing into this area, the void growth process will be more intense under the effect of HELP. And the failure strain reduction by HELP is mainly achieved through accelerating the void growth process.

4.8 Conclusion remarks

Hydrogen effect on material ductility is studied by incorporating the hydrogen diffusion process and the induced HELP effect into a finite element program. A series of finite element analyses of a representative material volume subjected to various stress states were carried out under certain loading speed that ensures the hydrogen distribution reaches steady state. The evolution of local stress and deformation states result in hydrogen redistribution in the material, which in turn changes the material's flow property. In general, the HELP effect promotes material failure by accelerating the void growth process. Furthermore, the HELP effect on ductile fracture is mainly influenced by local plastic strain

distribution, which determined by stress state, as characterized by the triaxiality and Lode parameter. The following briefly summarizes the findings of this study:

1. The loading speed of unit cell with initially evenly distributed hydrogen concentration will affect the ductility reduction intensity of HELP. Lower loading speed will accelerate the void growth process and reduce more failure strain until a low enough speed is reached. Lower than this certain speed, the failure strain will not be further reduced, and the hydrogen distribution is considered reaching a steady state.
2. The localized plastic strain generates new trapping sites and trapping more hydrogen in the localized area. HELP effect will soften this area and leads to further localization of plastic strain and hydrogen concentration.
3. From the analysis results obtained in this study, the effect of hydrostatic stress on rising hydrogen concentration is concluded weaker than the effect of plastic strain localization, which effectively increases local hydrogen concentration by generating new trapping sites.
4. Under stress state of higher triaxiality and near 0 Lode parameter, the plastic strain will be more localized into the region of near void surface, such that enables HELP to significantly accelerate the void growth process and causing pronounced reduction in ductility. The effect of hydrogen on void growth accelerating and failure strain reduction will gradually diminish at lower stress triaxiality and Lode parameter increases or becomes more negative as the plastic strain localization is weaker at the area near void surface.

CHAPTER V

INVESTIGATION OF DUCTILE DAMAGE MODEL THROUGH SINGLE MATERIAL POINT TEST

5.1 Introduction

The unit cell model presented in the last two chapters represents a material volume on the micromechanics scale. The ductile fracture process is investigated by analyzing the overall material response of a material point constructed by matrix material containing an explicit spherical void. Another approach to simulate a material point is to use a homogenized computational cell with implicit void volume friction. Gurson type ductile damage models are among the most popular method to describing the stress-strain relationship and damage evaluation with a computational cell at the similar scale of unit cell model and can be applied to much larger scale by using the computational cell as an element in FEA mesh. With a finite number of elements, ductile damage model can be applied to FEA mesh representing an arbitrary structure of interest, such the stress-strain evaluation and failure analysis can be performed at structure level. With knowledge gained from unit cell model, we can have a more detailed understanding of how ductile damage can be described and what is the effect of stress state on the failure of ductile material. In this chapter, we will discuss several Gurson type ductile damage models and the damage parameters they utilized. The evolution of these damage parameters will be calculated with damage models implemented in single material point model.

5.2 Ductile damage models

Ductile fracture is usually attributed to a process of void nucleation, growth and coalescence under triaxial stress state (McClintock, 1968; Rice and Tracey, 1969; Van Stone et al., 1985; Garrison Jr. and Moody, 1987) and a process due to shear localization when the stress triaxiality becomes low (Rice, 1976; Yamamoto, 1978; Mear and Hutchinson, 1985; Barsoum and Faleskog, 2007; Mohr and Marcadet, 2015). GTN model is one of the most widely used micromechanical models for ductile fracture when considering the void nucleation, growth, and coalescence process. The yield function of the GTN model takes the following form

$$\Phi = \left(\frac{\sigma_e}{\sigma_M}\right)^2 + 2q_1 f \cosh\left(\frac{q_2}{2}\frac{\sigma_{kk}}{\sigma_M}\right) - (1 + q_1 f^2) = 0 \tag{5.1}$$

where f is the current void volume fraction, σ_e is the macroscopic effective stress, σ_{kk} is the hydrostatic stress, and σ_M is the current yield stress of the matrix material. The adjustment parameters q_1 and q_2 were introduced by Tvergaard (1981, 1982) to improve model predictions. The evolution of the void volume fraction is given by

$$\dot{f} = \dot{f}_{growth} + \dot{f}_{nucleation} \tag{5.2}$$

where $\dot{f}_{growt}$ and $\dot{f}_{nucleation}$ represent the growth and nucleation of the voids. Evaluation of the void growth rate is based on the bulk material incompressibility under plastic deformation

$$\dot{f}_{growth} = (1 - f)\dot{\varepsilon}^p_{kk} \tag{5.3}$$

Where $\dot{\varepsilon}^p_{kk}$ represents the first invariant of the plastic strain rate tensor, which defines the rate of volume change. Void nucleation can be stress or strain controlled. A

commonly used strain controlled void nucleation law follows a normal distribution in a statistical way as suggested by Chu and Needleman (1980)

$$\dot{f}_{nucleation} = A_N \dot{\varepsilon}_M^p \,, \quad A_N = \frac{f_n}{S_n\sqrt{2\pi}} \exp\left[-\frac{1}{2}\left(\frac{\varepsilon_M^p - \varepsilon_n}{S_n}\right)^2\right] \tag{5.4}$$

where ε_M^p represents the matrix plastic strain, S_n and ε_n are the standard deviation and the mean value of the distribution of the plastic strain, and f_n is the total void volume fraction that can be nucleated. Parameters f_n, ε_n and S_n can be treated as material constants.

The effect of rapid void coalescence after the onset of localization is taken into account by replacing f in Eq. (5.1) with an effective porosity f^* defined by the following bilinear function (Tvergaard and Needleman, 1984)

$$f^* = \begin{cases} f & \text{for } f \le f_c \\ f_c + \frac{\frac{1}{q_1} - f_c}{f_f - f_c}(f - f_c) & \text{for } f_c \le f \le f_f \end{cases} \tag{5.5}$$

where f_c is the critical void volume fraction at which void coalescence begins and the material softening is accelerated thereafter. As f reaches f_f, the material loses all stress carrying capacity.

GTN model is capable of describing the volumetric damage caused by the nucleation and growth of voids in the matrix material. However, under shear dominated loading, the quantitative relationship between void size and failure strain cannot be firmly established since shear localization can occur with or without the existence of voids. To consider the process of shear localization, recently Xue (2008) and Nahshon and Hutchinson (2008) proposed similar modifications to the original GTN model to incorporate the shear-induced damage. In these modifications, the void volume fraction that appears in Eq. (5.1) is replaced by a general damage parameter containing contributions of both volumetric damage and shear damage while the form of the GTN

yield function is retained. Nahshon and Hutchinson (2008) claimed that f is no longer directly tied to the plastic volume change but rather should be regarded as a damage parameter and introduced an additional term in the evolution equation of f to account for shear damage. Xue (2008) directly introduced a new damage parameter, D, which contains both void damage and shear-induced damage, and substituted the $q_1 f$ term in Eq. (5.1) with D. Zhou et al. (2014) discussed the drawbacks of using a unified single damage parameter in the GTN yield function and suggested that two damage parameters, the volumetric damage (f) and the shear damage (D_s), should be included in the modified GTN model. This is done by combining the damage mechanics concept of Lemaitre with the GTN void growth model. When the total damage ($q_1 f + D_s$) becomes unity, the material loses its load carrying capacity completely. It is shown that this new model is not only capable of predicting damage and fracture under low (even negative) triaxiality conditions but also suppresses spurious damage that has been shown to develop in earlier modifications of the GTN model for moderate to high triaxiality regimes (Zhou et al., 2014). This model takes the form of

$$\Phi = \left(\frac{\sigma_e}{\sigma_M}\right)^2 + 2q_1 f \cosh\left(\frac{q_2}{2}\frac{\sigma_{kk}}{\sigma_M}\right) - [1 + (q_1 f + D_s)^2 - 2D_s] = 0 \qquad (5.6)$$

where f represents the void volume fraction (volumetric damage), which grows due to the hydrostatic tension and the evolution equation for f is the same as in the original GTN model as described in Eqs. (5.2-5.5); D_s represents the shear damage, which accumulates under the deviatoric stress state. This modified model degenerates to the GTN model when shear damage does not exist.

In establishing the shear damage evolution law, Xue (2008), Nahshon and Hutchinson (2008) as well as Zhou et al. (2014) all derived the evolution of shear damage

under the pure shear or simple shear state and then extended it to other stress states by introducing a Lode angle dependent function. The shear damage law of Nahshon and Hutchinson (2008) assumes linear dependence on the porosity and the effective strain increment. Xue (2008) developed his shear damage law based on the change of the void ligament of a unit cell model under simple shear deformation. Zhou et al. (2014) assumed that shear damage is not directly linked to the void volume fraction and regarded it as an accumulation of plastic deformation.

From the unit cell analysis in chapter III and IV, we do observe that the failure strain is strongly related with the plastic strain locally but not macroscopically, so here we use the damage evolution law proposed by Xue (2008) to describe the shear damage mechanism. This evolution law is expressed as

$$\dot{D}_s = q_3 f^{q_4} g(\theta_L) \varepsilon_M^p \dot{\varepsilon}_M^p \tag{5.7}$$

with

$$g(\theta_L) = \left(1 - \frac{6|\theta_L|}{\pi}\right) \tag{5.8}$$

Here shear damage is considered as a weighted integration of the equivalent plastic strain increment. According to Xue (2008), q_4 should be taken as 1/2 for 2D problems and 1/3 for 3D problems. The q_3 term is an adjustable parameter to scale the growth rate of the shear damage. This shear extended GTN ductile damage model can be described by Eq. (5.6), with D_s adopted from Eq.(5.7).

In the current form of shear extended GTN model, the matrix material obeys the isotropic J_2 flow plasticity theory, where σ_e is the von Mises equivalent stress. But as we mentioned in Chapter II, the plasticity response is not always isotropic for real material. Stewart and Cazacu (2011) have extended GTN model to account for the plastic anisotropy and tension-compression asymmetry exhibited by the matrix material. To further consider

the effect of shear damage, as shown by Zhai et al.(2016), a macroscopic yield criterion for anisotropic material based on the above shear extended GTN model can then be expressed as

$$\Phi = \left(\frac{\sigma_{Ae}}{\sigma_M}\right)^2 + 2q_1 f \cosh\left(\frac{q_2}{h_A}\frac{\sigma_{kk}}{\sigma_M}\right) - [1 + (q_1 f + D_s)^2 - 2D_s] = 0$$

$$\dot{f} = \dot{f}_{growt} + \dot{f}_{nucleation} \; ; \dot{f}_{growth} = (1-f)\dot{\varepsilon}^p_{kk} \; ; \dot{f}_{nucleation} = A_N \dot{\varepsilon}^p_M;$$

$$A_N = \frac{f_n}{S_n\sqrt{2\pi}} \exp\left[-\frac{1}{2}\left(\frac{\varepsilon^p_M - \varepsilon_n}{S_n}\right)^2\right];$$

$$\dot{D}_s = q_3 (f^*)^{q_4} g(\theta_L) \varepsilon^p_M \dot{\varepsilon}^p_M \; ; \; g(\theta_L) = \left(1 - \frac{6|\theta_L|}{\pi}\right); \tag{5.9}$$

$$D = q_1 f^* + D_s \, ;$$

$$f^* = \begin{cases} f & \text{for } D \le q_1 f_c \\ f_c + \frac{1/q_1 - f_c}{f_f - f_c}(f - f_c) & \text{for } q_1 f_c \le D \le q_1 f_f \end{cases}$$

where h_A is a material parameter depending on the anisotropy coefficients as well as the strength differential coefficient and σ_{Ae} is defined by Eq. (2.11).

In this model, two damage parameters, accounting for the void damage and the shear damage respectively, are coupled in the yield function and the flow potential. The material is assumed void free initially and nucleation of voids follows a strain-controlled criterion suggested by Chu and Needleman (1980). The majority of void nucleation takes place when the matrix plastic strain reaches the range $\varepsilon_n \pm S_n$. After void nucleation, the evolution of void volume fraction is described by the void growth rate, which is evaluated based on the bulk material incompressibility under plastic deformation. Therefore, the void growth rate is driven by the plastic deformation and the stress triaxiality. Because the matrix material is plastically anisotropic and asymmetric with respect to tension and

compression, the void growth rate is influenced by the anisotropy coefficients as well as the strength differential coefficient. The shear damage is considered as a weighted integration of the equivalent plastic strain increment. The evolution of the shear damage is driven by the matrix plastic strain and plastic strain rate and is also a function of the void volume fraction and Lode angle.

By enforcing equality between the rates of macroscopic plastic work and the matrix plastic dissipation, the matrix yield stress σ_M, and the matrix plastic strain rate $\dot{\varepsilon}_M^p$, are coupled through

$$\left(1-\frac{D}{q_1}\right)\sigma_M\dot{\varepsilon}_M^p = \sigma_{ij}\dot{\varepsilon}_{ij}^p \tag{5.10}$$

where the matrix material follows a prescribed hardening function $\sigma_M\left(\varepsilon_M^p\right)$.

5.3 Single material point test

To illustrate the predicted material response of the different damage models discussed above, a series of numerical tests was conducted, and the results were compared among GTN model, Shear modified GTN model, and the shear modified GTN model applied to anisotropic material. The single material point test will generate the effective stress-plastic strain response with proportional stress loading history. Focused on illustrating the evolution of volumetric and shear damage, void nucleation is omitted for the sake of clarity. In the following content, we will illustrate the implement of single material point calculation using the shear extended GTN model applied to anisotropic material, the model is defined by Eq. (5.9), because other above-mentioned models can be easily degraded from it. With $\boldsymbol{L}$ set to identity matrix and k=0, the model degrades to the

isotropic shear extended GTN model, with further degrading of set q_3 and q_4 to 0, the shear damage is eliminated, and the model then becomes GTN model.

In the numerical examples presented in this section, the isotropic matrix material was assumed to follow the J_2 flow plasticity theory and obey a power-law hardening, which coincides with the uniaxial tensile hardening curve in the rolling direction of anisotropic material.

$$\begin{aligned} \sigma &= E\varepsilon \qquad \varepsilon \le \varepsilon_0 \,, \\ \sigma &= \sigma_0 \left(\frac{\varepsilon}{\varepsilon_0}\right)^N \quad \varepsilon > \varepsilon_0 \,. \end{aligned} \tag{5.11}$$

where E represents the Young's modulus, σ_0 is the initial yield stress, ε_0 is the initial yield strain and N is the strain hardening exponent. The material parameters are taken to be $\varepsilon_0 = \frac{\sigma_0}{E} = 0.002$, $v = 0.3$ (Poisson's ratio), and $N = 0.1$.

The anisotropic material parameters are chosen as Table2.1 representing a transversely isotropic material for which the matrix has a weaker in-plane yield strength than through-thickness yield strength

The damage parameters, if applicable to the model, are listed in Table5.1 with no consideration of void nucleation.

Table 5.1. Model parameters for damage models

q_1	q_2	q_3	q_4	f_0	f_c	f_f
1.5	1.0	2.25	1/3	0.005	0.1	0.25

The stress tensor σ_{ij} can be represented by a proportionality factor $\tilde{\sigma}$ multiplied with a constant tensor R_{ij}. Consider only three principal stress components, then $\sigma_1 = \sigma_{11}$, $\sigma_2 = \sigma_{22}$ and $\sigma_3 = \sigma_{33}$ are the principal stress values, $\sigma_1' = \sigma_{11}'$, $\sigma_2' = \sigma_{22}'$ and $\sigma_3' = \sigma_{33}'$

are the principal values of the deviatoric stress tensor defined by $\sigma'_{ij} = \sigma_{ij} - \sigma_m \delta_{ij}$, where $\sigma_m = \frac{\sigma_{kk}}{3}$ is the mean stress. The anisotropic plasticity model has an effective stress of $\sigma_{Ae} = \sqrt{\frac{(|\hat{\sigma}_1| - k\hat{\sigma}_1)^2 + (|\hat{\sigma}_2| - k\hat{\sigma}_2)^2 + (|\hat{\sigma}_3| - k\hat{\sigma}_3)^2}{(|\theta_1| - k\theta_1)^2 + (|\theta_2| - k\theta_2)^2 + (|\theta_3| - k\theta_3)^2}}$, where $\hat{\boldsymbol{\sigma}} = \boldsymbol{L}: \boldsymbol{\sigma}'$. Note that the concept of triaxiality and Lode parameter does not automatically apply on the anisotropic material model because the term of effective stress in the definition of triaxiality, $\mathrm{T} = \frac{\sigma_m}{\sigma_e}$,is calculated as Von Mises plasticity. Although a similar concept of triaxiality factor of $\mathrm{T}_A = \frac{\sigma_m}{\sigma_{Ae}}$ sometimes is defined for the anisotropic model, but in this chapter, we only use T and μ value based on the isotropic material model.

Due to the softening effect introduced by the damage factors in the model, use $\tilde{\sigma}$ as the loading parameter is impractical. A more feasible approach would be to find plastic multiplier λ and apply it incrementally to compute $\tilde{\sigma}$ and the internal variables ε_M^p, f ,and D_s at each step accordingly.

A consistency condition can be expressed as

$$\dot{\Phi} = \frac{\partial \Phi}{\partial \sigma_{ij}} \dot{\sigma}_{ij} + \frac{\partial \Phi}{\partial \sigma_M} \frac{\partial \sigma_M}{\partial \varepsilon_M^p} \dot{\varepsilon}_M^p + \frac{\partial \Phi}{\partial f^*} \frac{\partial f^*}{\partial f} \dot{f} + \frac{\partial \Phi}{\partial D_s} \dot{D}_s \tag{5.12}$$

Substitute ε_M^p, f ,and D_s as functions of $\dot{\lambda}$:

$$\dot{\lambda} = \frac{1}{H} \frac{\partial \Phi}{\partial \sigma_{ij}} \dot{\sigma}_{ij} \tag{5.13}$$

H is the hardening modulus

$$H = -\left(\frac{\partial \Phi}{\partial \sigma_M} \frac{\partial \sigma_M}{\partial \varepsilon_M^p} \frac{\partial \varepsilon_M^p}{\partial \lambda} + \frac{\partial \Phi}{\partial f^*} \frac{\partial f^*}{\partial f} \frac{\partial f}{\partial \lambda} + \frac{\partial \Phi}{\partial D_s} \frac{\partial D_s}{\partial \lambda} \right) \tag{5.14}$$

for the considered model, $\frac{\partial \sigma_M}{\partial \varepsilon_M^p}$ is the tangent modulus of matrix material in uniaxial tensile direction along rolling direction, and other terms can be calculated as:

$$\frac{\partial \Phi}{\partial \sigma_M} = -2\frac{{\sigma_{Ae}}^2}{{\sigma_M}^3} - 3\frac{q_1 q_2 f^* \sigma_m}{h{\sigma_M}^2}\sinh\left(\frac{3q_2\sigma_m}{h\sigma_M}\right)$$

$$\frac{\partial \varepsilon_M^p}{\partial \lambda} = \frac{\sigma_{ij} n_{ij}}{(1-D/q_1)\sigma_M}, n_{ij} = \frac{\partial \Phi}{\partial \sigma_{ij}}$$

$$\frac{\partial \Phi}{\partial f^*} = 2q_1 \cosh\left(\frac{3q_2\sigma_m}{h\sigma_M}\right) - 2q_1(q_2 f^* + D_s)$$

$$\frac{\partial f^*}{\partial f} = \begin{cases} 1 & \text{for } f \le f_c \\ \frac{1/q_1 - f_c}{f_f - f_c} & \text{for } f_c \le f \le f_f \end{cases}$$

$$\frac{\partial f}{\partial \lambda} = (1-f) n_{kk}$$

$$\frac{\partial \Phi}{\partial D_s} = 2 - 2(q_1 f^* + D_s))$$

$$\frac{\partial D_s}{\partial \lambda} = q_3 (f^*)^{q_4} g(\theta_L) \varepsilon_M^p \frac{\partial \varepsilon_M^p}{\partial \lambda}$$

For stress state of components with fixed ratio, Eq. (5.13) can be written as Eq. (5.15) and the increment of $\tilde{\sigma}$ is obtained as Eq. (5.16).

$$\dot{\lambda} = \frac{\dot{\tilde{\sigma}}}{H}\frac{\partial \Phi}{\partial \sigma_{ij}} R_{ij} \tag{5.15}$$

$$\dot{\tilde{\sigma}} = \frac{H\dot{\lambda}}{\frac{\partial \Phi}{\partial \sigma_{ij}} R_{ij}} \tag{5.16}$$

We use MATLAB to solve Eq. (5.16) numerically using a forward Euler integration scheme. $\dot{\lambda}$ is chosen to be small enough that the solution was converged. Initial value of $\tilde{\sigma}$, corresponding to the onset of plastic deformation were solved from the yield function Φ in Eq. (5.9).

5.4 Results and discussion

5.4.1 Uniaxial loading

Fig. 5.1 and Fig. 5.2 are the comparison of the Von Mises effective stress versus effective plastic strain curves and the void growth rates among three models. The black solid curve, red dashed curve, and blue single dotted curve represent the uniaxial tensile results predicted by GTN model, shear modified GTN model, and the shear modified GTN model applied to anisotropic material along rolling direction. Additionally, the green solid curve is the material response of no damage matrix material, which plotted as a reference.

As shown by Fig. 5.1, for uniaxial tensile loading, corresponding to T=0.33 and μ=-1 for isotropic material, there is no difference between predicted results from GTN and GTN-Shear model as there is no shear damage generated under this loading condition. The softening of materials is solely caused by the same amount of volumetric damage for those two models under uniaxial tensile loading as shown by Fig. 5.2. The predicted anisotropic material response of uniaxial tensile loading along rolling direction however showed some deviation from the isotropic results under the influence of h, which reflected the effect of anisotropy on damage evolution. Because the anisotropic material considered here is overall stronger than the isotropic material, the applied h value decreases the void growth rate for anisotropic material, resulting a larger failure strain. Despite the anisotropic material response in rolling direction is softened from the same damage free matrix material hardening curve, the strain-stress and the void growth rate curves of anisotropic material are significantly different from the isotropic cases, showing that the modified parameters for anisotropic material in ductile damage model do have some effect on damage evolution.

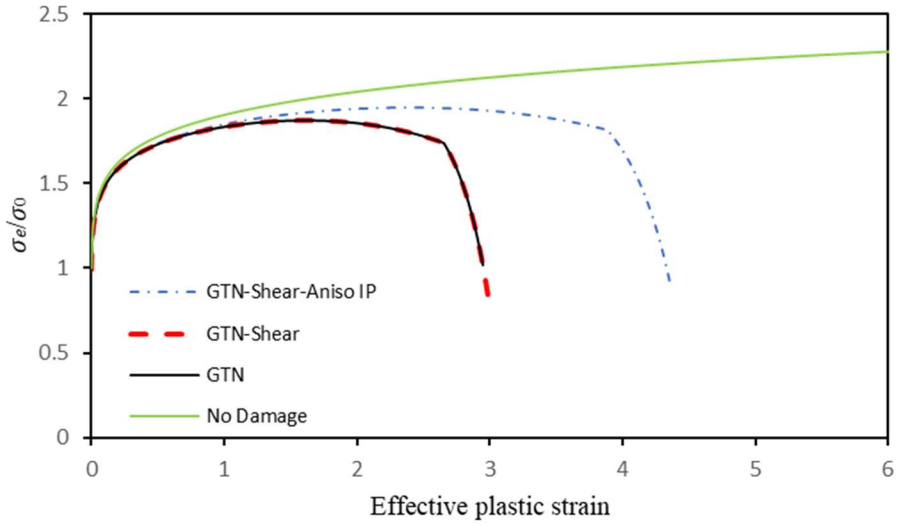

Figure 5.1. Comparison of the Von Mises effective stress versus effective plastic strain response between the GTN model, GTN-Shear model, and GTN-Shear model with anisotropic material under uniaxial tensile loading.

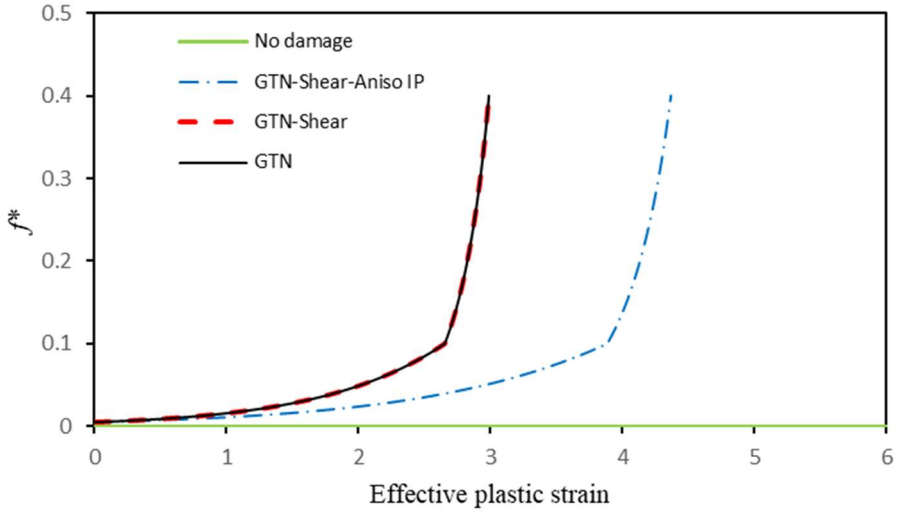

Figure 5.2. Comparison of the effective void growth rates predicted by the GTN model, GTN-Shear model, and GTN-Shear model with anisotropic material under uniaxial tensile loading.

The stress triaxiality and Lode parameter considered in this study can only apply to isotropic material obeying Von Mises plasticity or the plasticity response of uniaxial loading along rolling direction of the anisotropic material. Therefore, the comparison of results with the same T or μ value is only feasible for isotropic material model. And the predicted results are compared separately as two groups, namely isotropic and anisotropic groups. The results of damage models based on isotropic material are focused on illustrating the evolution of volumetric and shear damage parameters under different T and μ, while results from the anisotropic material will be focusing on the difference of material response between different loading directions.

5.4.2 Evolution of volumetric and shear damage

As illustrated in the above uniaxial loading case, under generalized tensile loading, both GTN and GTN-Shear damage model predicted the same result because GTN-Shear model is predicting no shear damage D_s under this stress state.

Under generalized shear loading condition, corresponding to a θ_L value of 0, i.e. μ of 0, the predicted results nevertheless showed some discrepancy. As shown in Fig. 5.3, when the triaxiality is low, at 0.7, the predicted stress-strain curve of GTN-Shear model is much lower than the GTN model, and the predicted material failure indicated by the sudden drop of stress-strain curve is at much smaller effective strain for GTN-Shear model. The additional softening of material and reduction on failure strain on top of GTN model is caused by the accounted shear damage as hinted by Fig. 5.4. The additional shear damage softened the material while f^* is the same value at an earlier stage in both models, and the shear damage contributed in critical void volume fraction of void coalescence and resulting

an earlier coalescence shown by the earlier sudden rise of f^* value in GTN-Shear model. As triaxiality raise to 1.0 and 1.3, the difference between stress-strain results predicted by GTN model and shear extended GTN model become less significant. As shown in Fig. 5.5, the decreased difference between two models is because the volumetric damage, i.e. effective void friction f^*, becomes dominant in GTN-Shear model, and the shear damage no longer plays a greater role in damage mechanics. Note the shear damage is still increasing with triaxiality, and that is due to its correlation with the void volume friction f, which is larger at higher triaxiality. The phenomenon of volumetric damage domination at higher triaxiality is consistent with the observation in unit cell analysis that the void size is larger at the point of material failure when the triaxiality is higher.

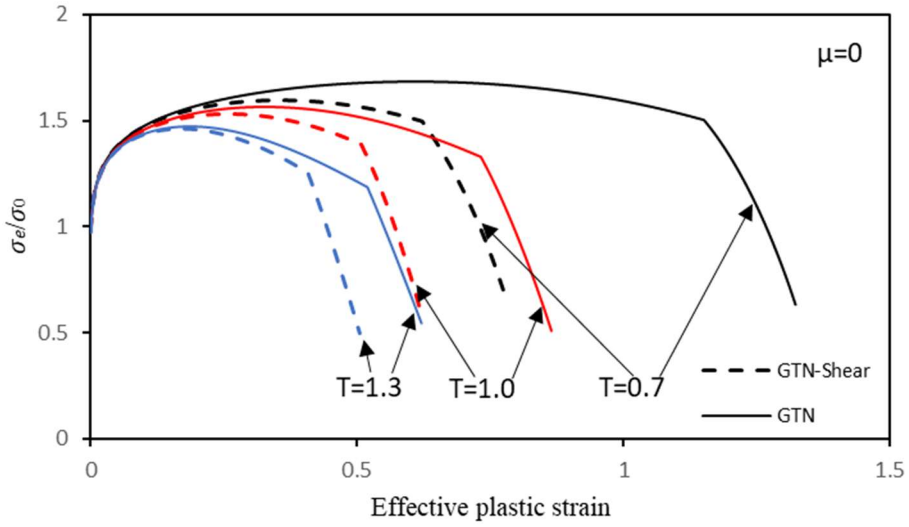

Figure 5.3. Comparison of the predicted Von Mises effective stress versus effective plastic strain response between GTN and GTN-Shear model under different triaxiality of 0.7,1.0 and 1.3 when Lode parameter kept as 0.

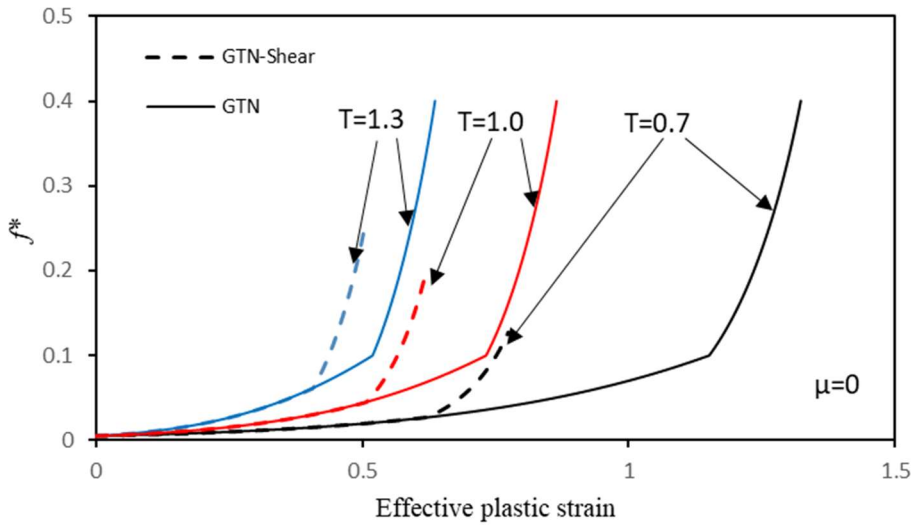

Figure 5.4. Comparison of the effective void growth rates predicted by GTN and GTN-Shear model under different triaxiality of 0.7,1.0 and 1.3 when Lode parameter kept as 0.

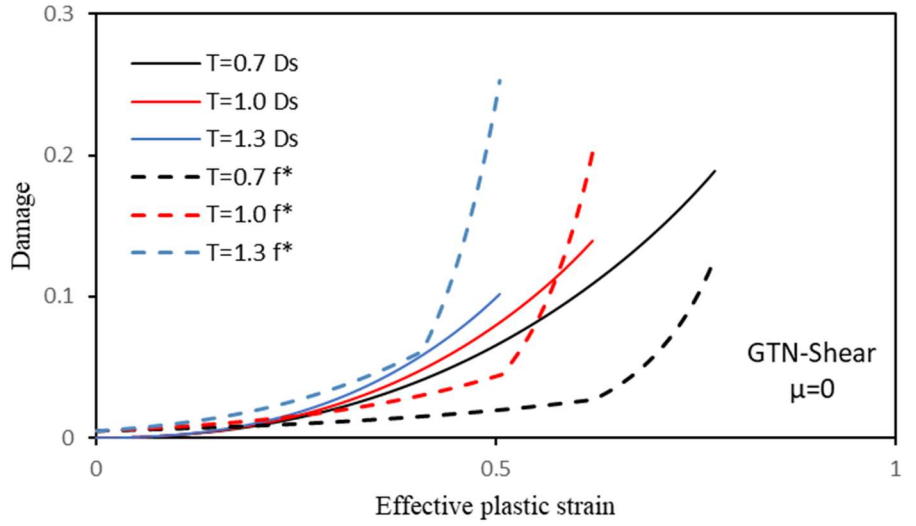

Figure 5.5. Comparison of the effective void growth rates and the shear damage evolution predicted by GTN-Shear model under different triaxiality of 0.7,1.0 and 1.3 when Lode parameter kept as 0.

The shear damage predicted by GTN-Shear model is not only affected by volume friction but also depending on the Lode parameter as calculated by Eq.(5.6). As shown by Fig. 5.6, under a certain triaxiality, the predicted shear damage is highest at Lode parameter μ=0 and become gradually lower when Lode parameter moves toward-1 or 1. It's worth mention that the demonstrated shear damage counter from Xue (2008) did not differential the damage evolution between positive and negative Lode parameter values, while the unit cell model suggests that the failure strain is not symmetric about 0 Lode parameter, and this difference might worth investigation and probably should be accounted in future studies.

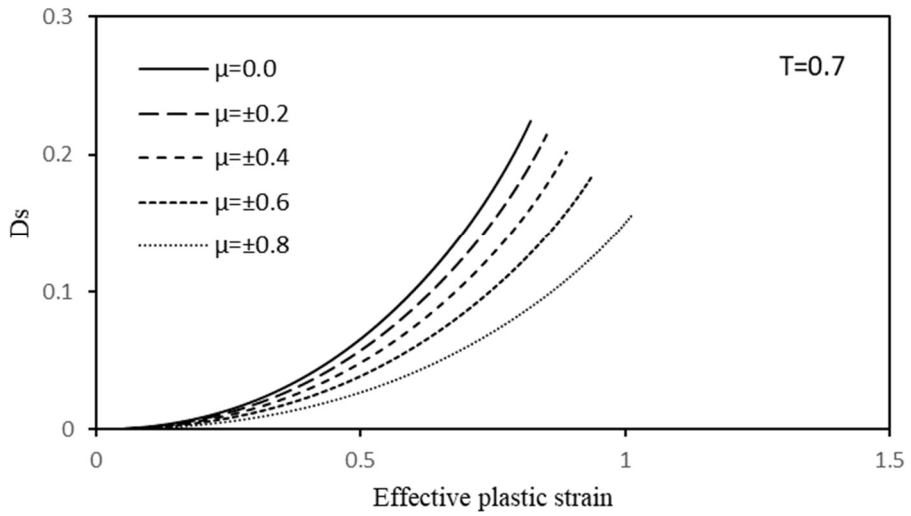

Figure 5.6. Comparison of the shear damage evolution predicted by GTN-Shear model under different Lode parameter of 0, ±0.2, ±0.4, ±0.6, ±0.8 when triaxiality kept as 0.7.

5.4.3 Response of an anisotropic material

The GTN-Shear damage model is modified and applied to the anisotropic plasticity material discussed in section 2.3. By modify equivalent stress and therefore yield condition, plus accounting volumetric and shear damage evolution affected by anisotropy, this model can capture the ductile damage process of an orthotropic material with tension-compression strength differential. In this section, we will be focus on the anisotropic stress-strain response and damage evolution of this model, other complex factors of this model will be demonstrated in the next chapter by the calibration and verification of this model with experimental data.

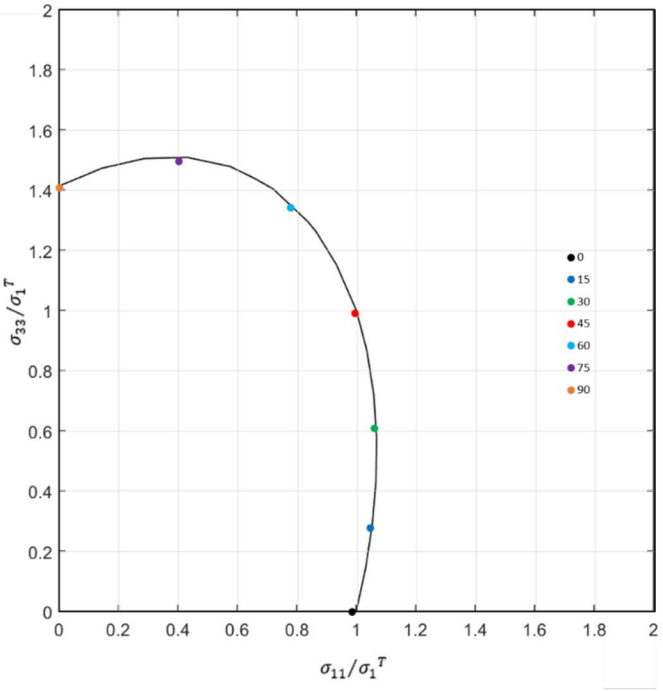

Figure 5.7. Normal-rolling plane stress yield locus for void-free material (black line) and the initial yield points predicted by GTN-Shear model with anisotropic material for uniaxial tensile loading along directions of 0, 15, 30, 45, 60, 75, 90 degrees from rolling direction to normal direction.

Fig. 5.7 shows the initial yielding points predicted by GTN-Shear model with anisotropic material for uniaxial loading along directions of 0, 15, 30, 45, 60, 75, 90 degrees from rolling direction to normal direction. The points are marked by stress components ratio of $\sigma_{11}/{\sigma_1}^T$ and $\sigma_{33}/{\sigma_1}^T$, with σ_{11} and σ_{33} respect to the material coordinate. Because of the identical principal stress components ratio, the effective stress ratio($\sqrt{{\sigma_{11}}^2+{\sigma_{33}}^2}$) versus effective strain curve shown in Fig. 5.8 are proportional and reflecting the proportional hardening evolution law and proportional damage evolution among those loading cases along different uniaxial loading directions.

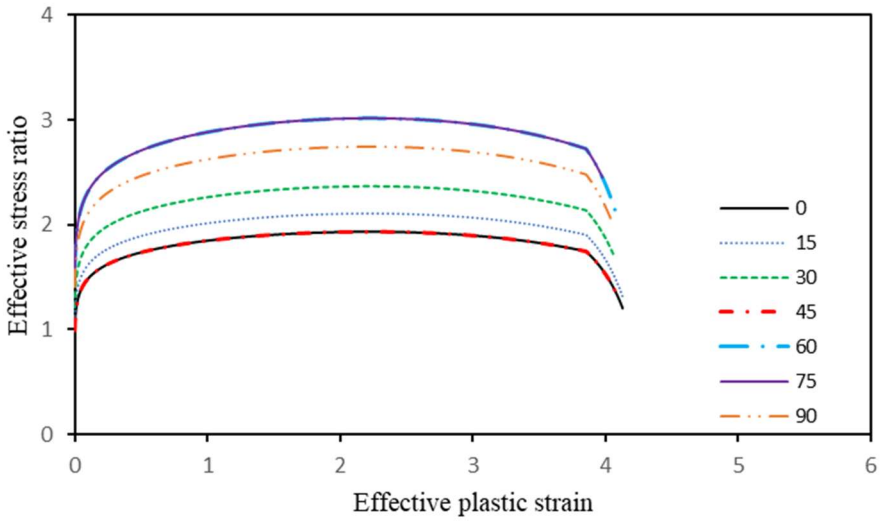

Figure 5.8. Comparison of effective stress ratio versus effective plastic strain results predicted by GTN-Shear model with anisotropic material for uniaxial tensile loading along directions of 0, 15, 30, 45, 60, 75, 90 degrees from rolling direction to normal direction.

Fig. 5.9 shows the initial yield points predicted by GTN-Shear model with anisotropic material for shear loading in normal-rolling plane and rolling-transverse plane. The points are again marked by stress components ratio of the shear plane. From effective stress ratio versus effective strain curve shown in Fig. 5.10, now we notice that the curves are not proportional alike uniaxial tensile loading, this is mainly because the shear damage in the model is not factored by yield stress or the stress components over the rolling direction yield stress, therefore passively reflected the strength differential along different directions.

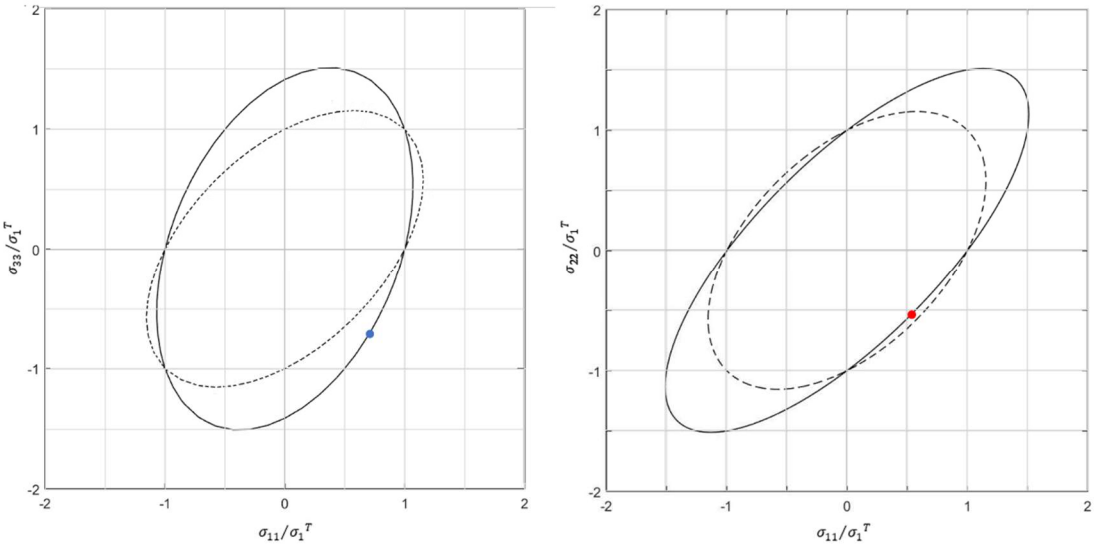

Figure 5.9. Normal-rolling and rolling-transverse plane stress yield locus for void-free material (black line) and the initial yield points predicted by GTN-Shear model with anisotropic material for shear loading in normal-rolling plane and rolling-transverse plane.

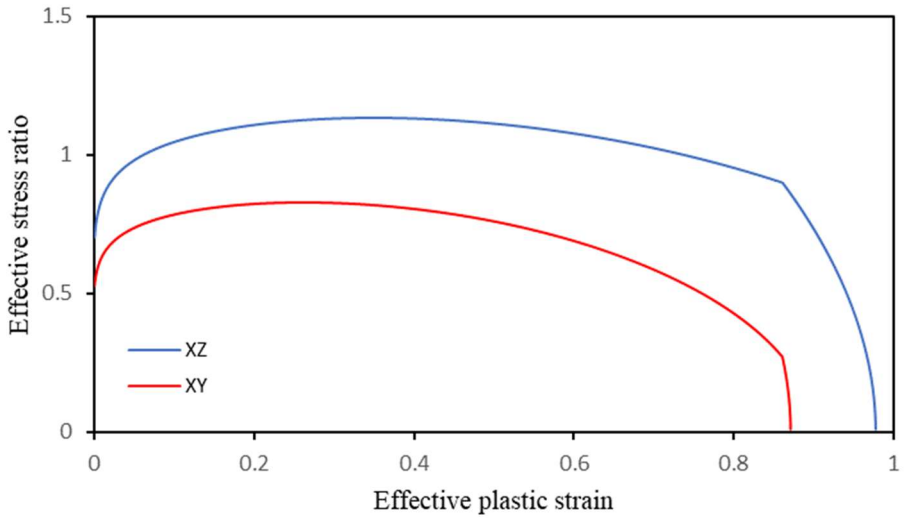

Figure 5.10. The effective stress ratio versus effective plastic strain response predicted by GTN-Shear model with anisotropic material for shear loading in normal-rolling plane and rolling-transverse plane.

From the damage evolution of anisotropic material through single material point model, we can see the damage parameters are still treated as ad-hoc parameter due to the complex nature of the anisotropic material and didn't quite evolved from its carefully formed isotropic definition. Still, this damage parameter setup is already capable of describing complex ductile damage process accounting shear and volumetric damage as shown in the following chapter. Together with the anisotropic model extending its potential to capture incrementally evolved yield locus at various effective plastic strain levels and tension-compression strength differential.

CHAPTER VI

APPLICATION OF THE DUCTILE DAMAGE MODEL TO PREDICT THE RESPONSE OF A COMMERCIALLY PURE TITANIUM

6.1 Introduction

We have learned from the unit cell models that the volumetric damage alone, a damage factor closely affected by the intensity of stress triaxiality, is insufficient to describe the material damage process. At least other damage factors affected by the Lode parameter, such as shear damage, should be also considered when modeling ductile damage. In last chapter, we have reviewed the shear considering GTN damage model, and discussed briefly on its application on anisotropic material. In this chapter, we will further demonstrate the capacity of this model through a complex process of calibration and verification with commercially pure titanium test data, and detail the evolution of the damage parameters and the effect of anisotropy of matrix material.

The commercially pure titanium (CP-Ti) considered in this study has a hexagonal closed packed (hcp) crystal structure at room temperature and is known to display plastic anisotropy and have a strong strength differential in tension and compression. It is generally agreed that the strong strength differential is associated with the activation of twinning (Chun et al., 2005; Salem et al., 2003; Hosford et al., 1973).

To consider damage evolution in anisotropic material such as CP-Ti, we use the GTN-Shear model with anisotropic material from the last chapter, combined from Stewart and Cazacu (2011) and Zhou et al. (2014), to describe ductile damage evolution in CP-Ti.

6.2 Specimens and material properties

The CP-Ti considered in this study was purchased in the form of 12.7mm thick hot-rolled plate, and all specimens were machined from this plate.

The test matrix included uniaxial tensile specimens and compressive specimens in the rolling (RD), transverse (TD) and normal through thickness (ND) directions, tensile notched round bars, grooved plane strain specimens, and thin wall torsion specimens in the RD and TD. Thin wall specimens were subjected to pure torsion and combined tension-torsion loading. Sketches of selected specimens are shown in Fig. 6. 1., detailed description can be found in Zhai et al. (2016).

Figure 6.1. Sketches of a smooth round bar, a notched round bar, a compression specimen, a torsion tension specimen, and a flat grooved plane strain specimen.

6.2.1 Matrix material calibration

Among the experiments conducted, the uniaxial tensile and compressive data in RD, TD, and ND, the in-plane tensile data along the 45° direction, the pure torsion data with the axis of the specimen along RD and TD are used for calibrating the matrix plasticity model, and the round tensile specimen and the pure torsion specimen in TD are used for the ductile damage model calibration. Other specimens, including the notched round tensile specimens, the flat grooved plane strain tensile specimens and the tension-torsion specimens are used for model validation.

The engineering stress-strain curves and true stress vs. true plastic strain curves obtained from the uniaxial tension and the uniaxial compression tests in the RD, TD, and ND are shown in Figs. 6.2-6.4.

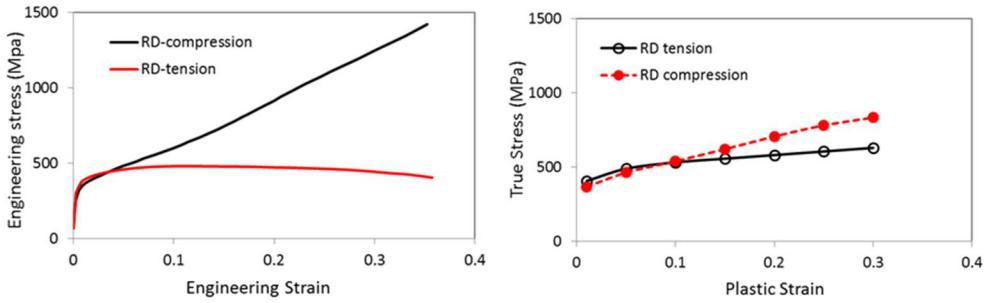

Figure 6.2. Stress-strain curves in tension and compression along the in-plane rolling direction (RD): (a) the engineering stress-strain curve; (b) the true stress vs. true plastic strain curve.

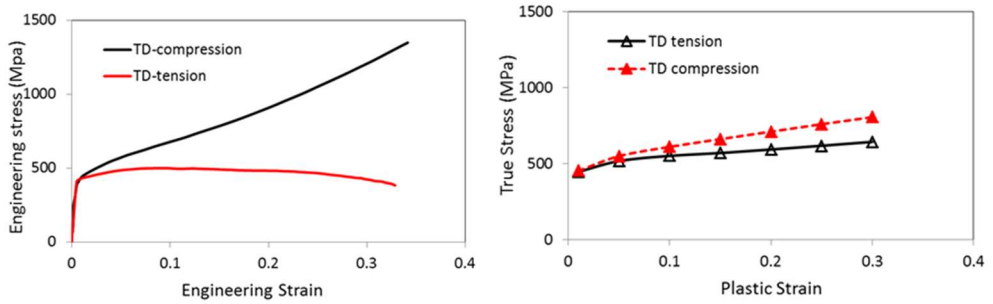

Figure 6.3. Stress-strain curves in tension and compression along the in-plane transverse direction (TD): (a) the engineering stress-strain curve; (b) the true stress vs. true plastic strain curve.

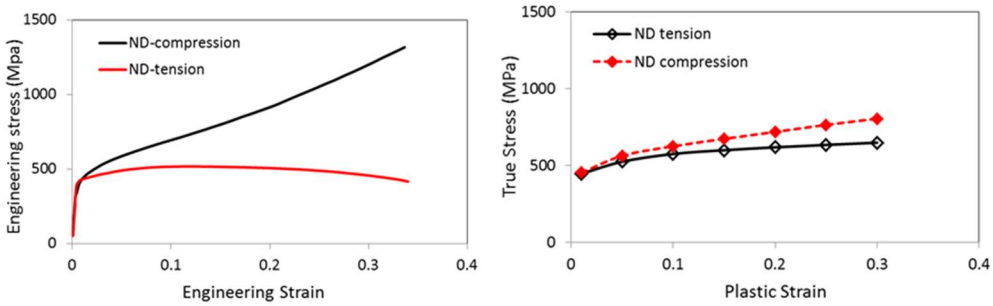

Figure 6.4. Stress-strain curves in tension and compression along the normal direction (ND): (a) the engineering stress-strain curve; (b) the true stress vs. true plastic strain curve.

The different stress-strain curve obtained from various directions confirm that the material is anisotropic and displays tension-compression asymmetry. Furthermore, the extent of plastic anisotropy and strength differential response evolves as the plastic deformation increases. In Figs. 6.2-6.4, the symbols, for which the numerical values are listed in Table 6.1, indicate the data point used in the optimization process to calculate the linear transformation matrix $\boldsymbol{L}$ and the strength differential coefficient k.

Table 6.1. Stress-strain data in rolling, transverse and normal directions at different plastic strain levels

Plastic Strain	True stress (MPa)					
	Uniaxial Tension in Rolling Direction	Uniaxial Compression in Rolling Direction	Uniaxial Tension in Transverse Direction	Uniaxial Compression in Transverse Direction	Uniaxial Tension in Normal Direction	Uniaxial Compression in Normal Direction
0.01	405.07	365.65	445.04	451.71	444.99	451.98
0.05	487.76	461.73	515.96	548.27	523.38	561.92
0.1	530.59	538.25	550.00	609.23	573.94	623.87
0.15	555.62	619.20	568.64	660.00	598.09	672.11
0.2	579.71	704.65	591.62	709.26	617.11	717.44
0.25	603.92	779.38	616.64	758.32	632.69	763.12
0.3	628.28	831.93	642.09	804.44	647.22	803.43

The anisotropy and strength differential coefficients, $\boldsymbol{L}$ and k, involved in the matrix plasticity model is determined by minimizing the error function given by Eq. (6.1).

$$Error(\boldsymbol{L},k) = \sum_i w_i \left(\frac{\sigma_{e\alpha}^T}{\sigma_0^T} - 1\right)^2 + \sum_j w_j \left(\frac{\sigma_{e\alpha}^C}{\sigma_0^T} - 1\right)^2 + \sum_k w_k \left(\frac{\sigma_{e\tau}}{\sigma_0^T} - 1\right)^2 + \sum_m w_m \left(\frac{r_\alpha^T}{r_\alpha^{exp}} - 1\right)^2 \qquad (6.1)$$

where i represents the number of experimental tensile yield stress, j represents the number of experimental compressive yield stress, k represents the number of experimental shear yield stress, w_i, w_j and w_k are the weighting factors given to the respective experimental values, r is the Lankford coefficient, σ_0^T is the experimental tensile yield stress along the rolling direction and the theoretical values $\sigma_{e\alpha}^T$ and $\sigma_{e\alpha}^C$ are calculated through the equations given in Zhai et al.(2016) . MATLAB programs are written to compute the error function and find optimal sets of anisotropic coefficients. The MATLAB built-in minimization function “fminsearch” are used for finding the error function minimums.

Using the tensile and compressive flow stress data in RD, TD, and ND, the in-plane tensile flow stress data along the 45° direction, the pure torsion data with the axis of the specimen along RD and TD, and the *r*-values obtained in the uniaxial tensile test along RD, the anisotropy coefficients $\boldsymbol{L}$ and k are calibrated, and the parameters are listed in Table 6.2. The experimental data indicate that there is distortion of the yield surface even for the simplest monotonic loading paths. As a result, the anisotropy coefficients vary with the plastic strain.

Table 6.2. Calibrated anisotropy and strength differential coefficients

ε^p	k	L_{11}	L_{12}	L_{13}	L_{22}	L_{23}	L_{33}	L_{44}	L_{55}	L_{66}
0.01	*-0.0167*	0.9997	-0.0017	0.0020	0.0655	0.9362	0.0618	1.0525	0.7544	1.0250
0.05	-0.0850	1.0556	-0.0314	-0.0242	1.0030	0.0284	0.9957	1.1517	0.8924	1.1436
0.1	-0.1528	0.9790	-0.0013	0.0224	0.9539	0.0475	0.9302	1.0362	0.8087	1.0350
0.15	-0.2329	1.0359	-0.0342	-0.0018	1.0185	0.0157	0.9861	1.1191	0.9590	1.1919
0.2	-0.3254	0.9515	0.0118	0.0367	0.9390	0.0492	0.9141	0.9737	0.8644	1.1677
0.25	-0.4510	1.0152	-0.0155	0.0003	0.9999	0.0156	0.9841	1.0613	0.9924	1.5451
0.3	-0.5226	1.0078	-0.0075	-0.0003	0.9933	0.0142	0.9861	1.0386	0.9983	1.7473

Fig. 6.5 plots the predicted yield loci given by Eq. (2.11) in comparison with the experimental data at different strain levels, where the open circles represent the RD tensile flow stress data, the solid circles represent the RD compressive flow stress data, the open triangles represent the TD tensile flow stress data, the solid triangle represent the TD compressive flow stress data, the open diamonds represent the ND tensile flow stress data, and the solid diamonds represent the ND compressive flow stress data. It is shown that the criterion describes well the asymmetry and anisotropy in yielding. Furthermore, the yield loci change shape as the plastic strain increases, reflecting the material's texture evolution.

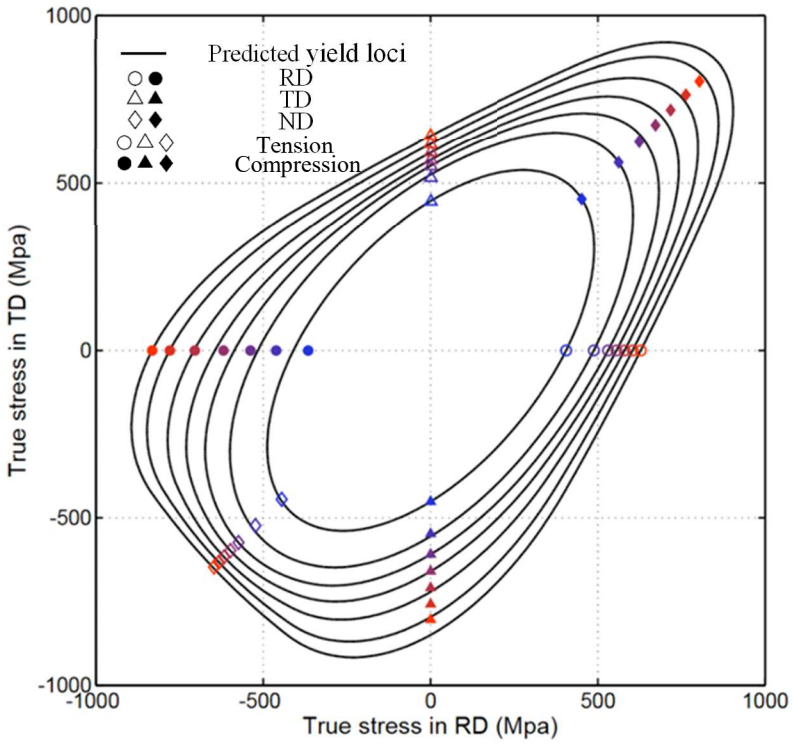

Figure 6.5. The evolution of the yield loci with accumulated plastic strain

6.2.2 Calibration of the ductile damage model

In Eq. (5.9), parameters q_1 and q_2 were introduced by Tvergaard (1981, 1982) to the original Gurson model to improve model predictions. Here the values suggested by Tvergaard (1981, 1982) are adopted, i.e., $q_1 = 1.5$, $q_2 = 1$. The ductile damage model calibration follows a two-step strategy as shown in Zhai et al. (2016). For specimens that the onset of fracture was dominated by the void damage mechanism, e.g., the round tensile specimens, the calibration of void related parameters are conducted. The shear damage parameters are calibrated using the test data, which fracture was dominated by shear damage, e.g., the pure torsion specimen.

Table 6.3 lists the calibrated damage model parameters. The B-notched, D-notched, E-notched round bar, the flat grooved plane strain tensile specimen and tension-torsion specimen are simulated using the calibrated model parameters and the numerical results are compared with the experimental data in section 6.3. All the specimens are modeled in three dimensions because the material is anisotropic.

Table 6.3. Calibrated damage model parameters

f_n	f_c	q_3
0.002	0.035	1.6

6.3 Comparison between the numerical and the experimental results

This section shows the comparisons between the model predictions and the experimental data. In the numerical simulations, the tensile stress-strain curve obtained from the smooth round specimen in the rolling direction is used together with the calibrated model parameters listed in Tables 6.2 and 6.3.

6.3.1 Finite element models of specimens

In the finite element analyses, three-dimensional, 8-node brick elements with reduced integration (C3D8R) are used for all specimens, the element size is 63.5μm ×63.5μm × 63.5μm in sensitive regions where failure may occur. Fig. 6.6 shows typical finite element meshes of the notched round tensile specimen, the plane strain tensile specimen, and the torsion specimen.

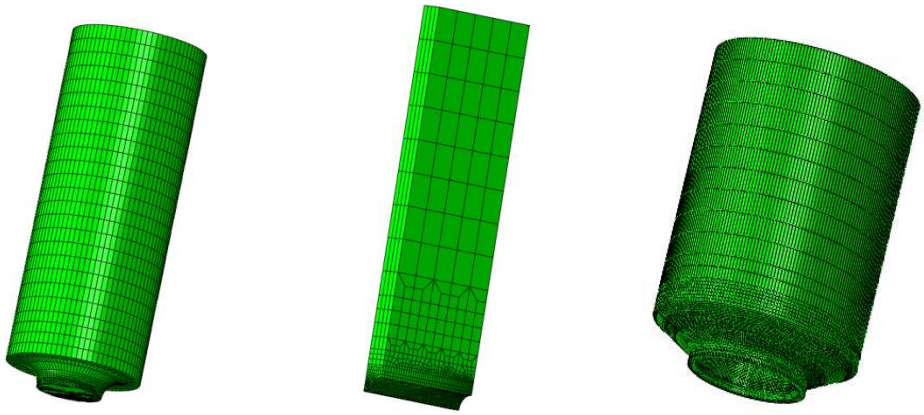

Figure 6.6. Typical finite element meshes of the notched round tensile specimen, the plane strain tensile specimen and the torsion specimen

6.3.2 Load vs. displacement and torque vs. twist angle response

Figs. 6.7(a-b) compare the computed load vs. displacement curves of the smooth round tensile specimens in RD and TD with the experimental data while Fig. 6.7 (c) compares the computed load vs. displacement curve of the miniature tensile specimen in ND with the experimental data. Figs. 6.7(d-f) compares the load vs. displacement response between the numerical simulations and the experimental data for the compression specimens in the RD, TD, and ND. There was no failure observed in compression specimens before the experiments were stopped. In these figures, the thicker lines (in red) represent the simulation results and the thinner lines (in black) represent the corresponding experimental data. Fig. 6.8 compares the computed torque vs. twist angle responses of the pure torsion specimens with the experimental data. Since all these specimens are used to identify the anisotropic and strength differential coefficients of the plasticity model, the

predicted mechanical responses of these specimens agree very well with the experimental measurements.

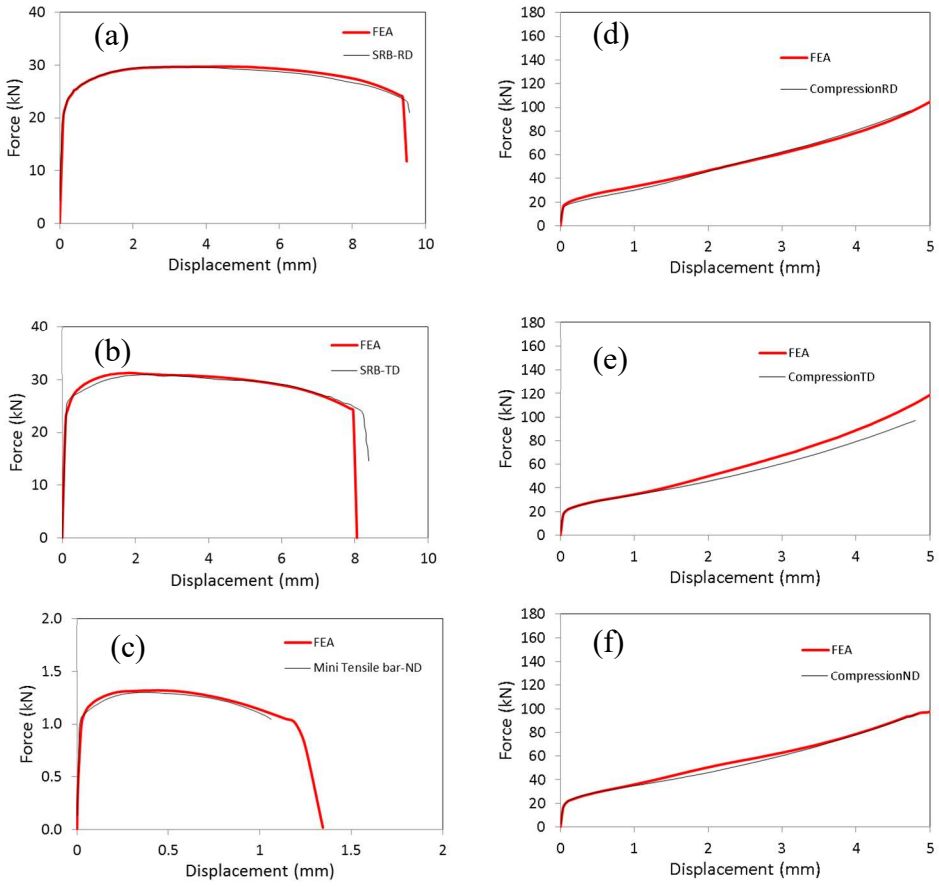

Figure 6.7. Comparisons between the numerical predictions and the experimental data for the tension specimens: (a) smooth round bar in rolling direction; (b) smooth round bar in transverse direction; (c) tensile bar in normal direction, and compression specimens: (d) rolling direction; (e) transverse direction; (f) normal direction.

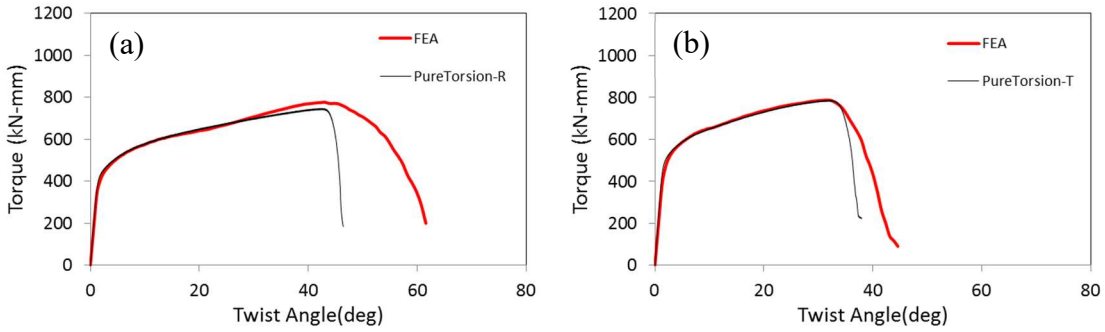

Figure 6.8. Comparisons of the computed torque vs. twist angle response with the experimental data for the pure torsion specimen ("R" refers to the rolling direction and "T" refers to the transverse direction)

To validate the calibrated model, the notched round tensile specimens, the flat grooved plane strain tensile specimens and the tension-torsion specimens were analyzed. Fig. 6.9 compares the computed load vs. displacement responses with the experimental data for the notched round tensile specimens having different notch radii. The comparisons are made in both rolling and transverse directions. The load-displacement discrepancy is partially due to material hardening and plastic anisotropic effects without explicitly considering the different values of stress triaxiality. Generally, the model can accurately predict the load-displacement responses of these specimens.

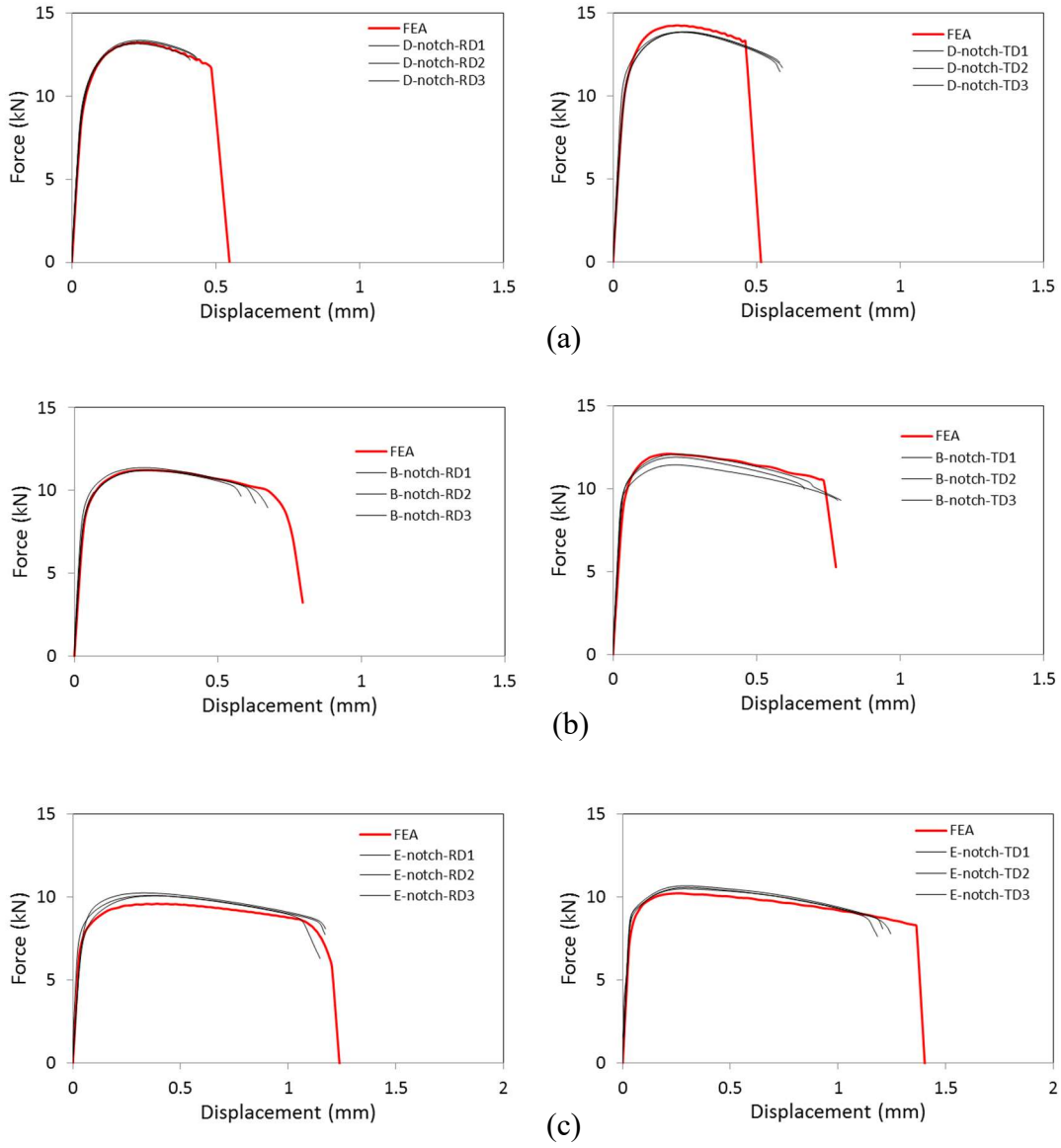

Figure 6.9. Comparisons of the computed force vs. displacement responses with the experimental data for the notched round tensile specimens in rolling and transverse directions: (a) Specimen D (notch radius = 0.762mm); (b) Specimen B (notch radius = 1.524mm); (c) Specimen E (notch radius = 3.81mm)

Fig. 6.10 compares the computed load vs. displacement responses with the experimental data for the flat grooved plane strain tensile specimens having different groove radii. The comparisons are made in both rolling and transverse directions. The predicted load and displacement curves are higher than the experimental results especially along the rolling directions. One likely reason of this error is the overprediction of compressional yield tress in ND direction. According to Fig. 6.5, the yield loci for plastic strain larger than 0.1 falls outside the corresponding experimental points, this means the model will predicts a higher compression yield stress value in ND direction than experiment value. And during the tensile loading, plane strain specimens are experiencing the most compression in ND direction among all tested specimens.

In general, the model is reasonably capable of predicting the load-displacement responses of these specimens. The failure predictions of the round notched specimens show better agreement with experimental observations than the flat grooved specimens.

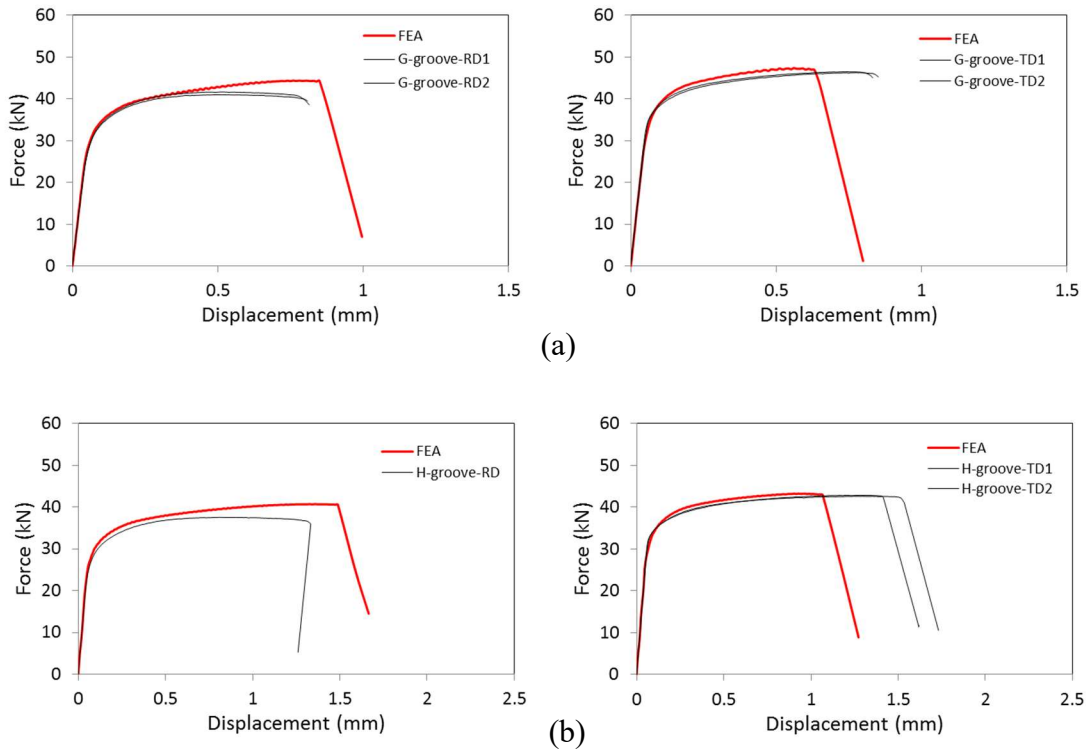

Figure 6.10. Comparisons of the computed force vs. displacement responses with the experimental data of plane strain tensile specimens in rolling and transverse directions: (a) Specimen G (groove radius = 5.08mm); (b) Specimen H (groove radius = 16.256mm)

Figs. 6.11-6.14 provide the comparisons of the axial force vs. axial displacement and torque vs. twist angle responses between the numerical simulations and the experimental data for the tension-torsion specimens with various applied tensile displacement/twist angle ratios. These displacement/angle (mm/radian) ratios are listed in Table 6.4. Different applied tensile displacement/twist angle ratio leads to different stress states experienced by the specimen (Graham et al., 2012). Model predictions agreed very well with experiments. Specimens with lower tensile displacement/twist angle ratios tend to show a sharp decrease in axial force in the plastic region. This is possibility because the material exhibits the so-called Swift effect, i.e., the material elongates naturally under torsional loading. Because of the displacement-controlled loading of the experiment, when the applied tensile displacement is less than the natural elongation of the specimen, a compressive force will be resulted on the specimen.

Table 6.4. Ratio of the applied tensile displacement over the applied twist angle used in the tension-torsion test

Specimens	Rotation axis along the rolling direction	L9	L8	L7, L10	L6, L11
	Rotation axis along the transverse direction	T5 ,T11	T10	T9, T6	T8, T1
Tensile displacement/twist angle (mm/radian)		0.10668	0.2794	0.5334	1.1684

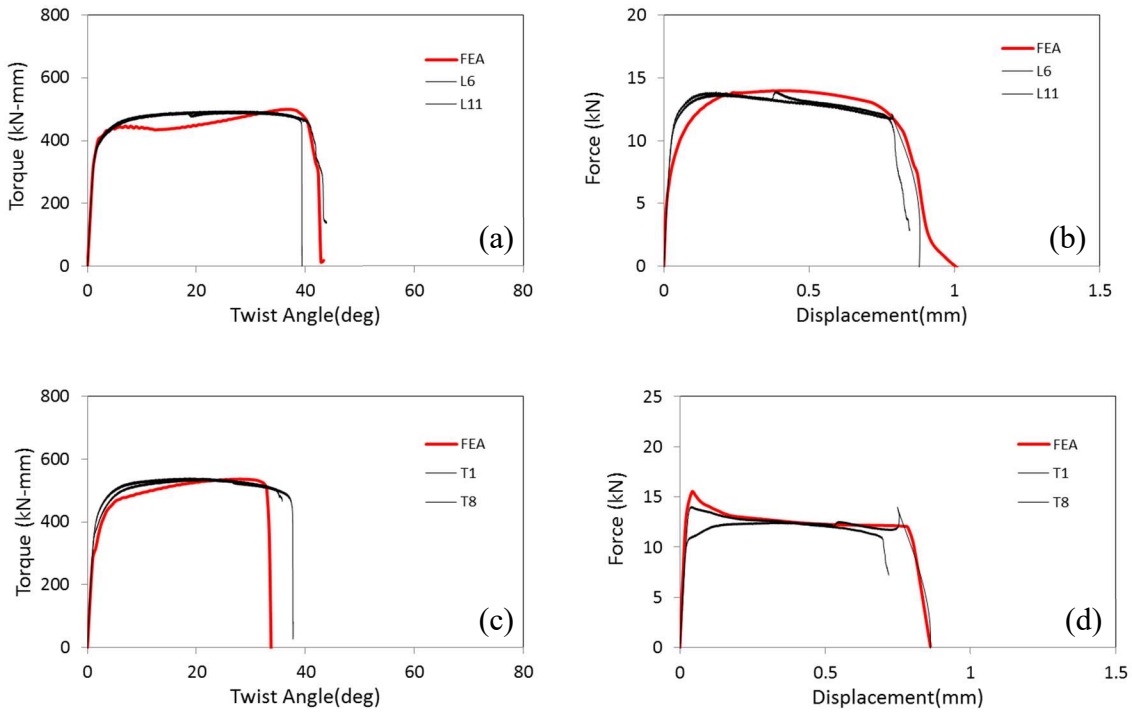

Figure 6.11. Comparisons between the numerical predictions and the experimental data for the tension-torsion specimen (tensile displacement/twist angel (mm/radian) = 1.1684) in rolling direction: (a) torque vs. twist angle; (b) axial force vs. axial displacement, and transverse direction: (c) torque vs. twist angle; (d) axial force vs. axial displacement.

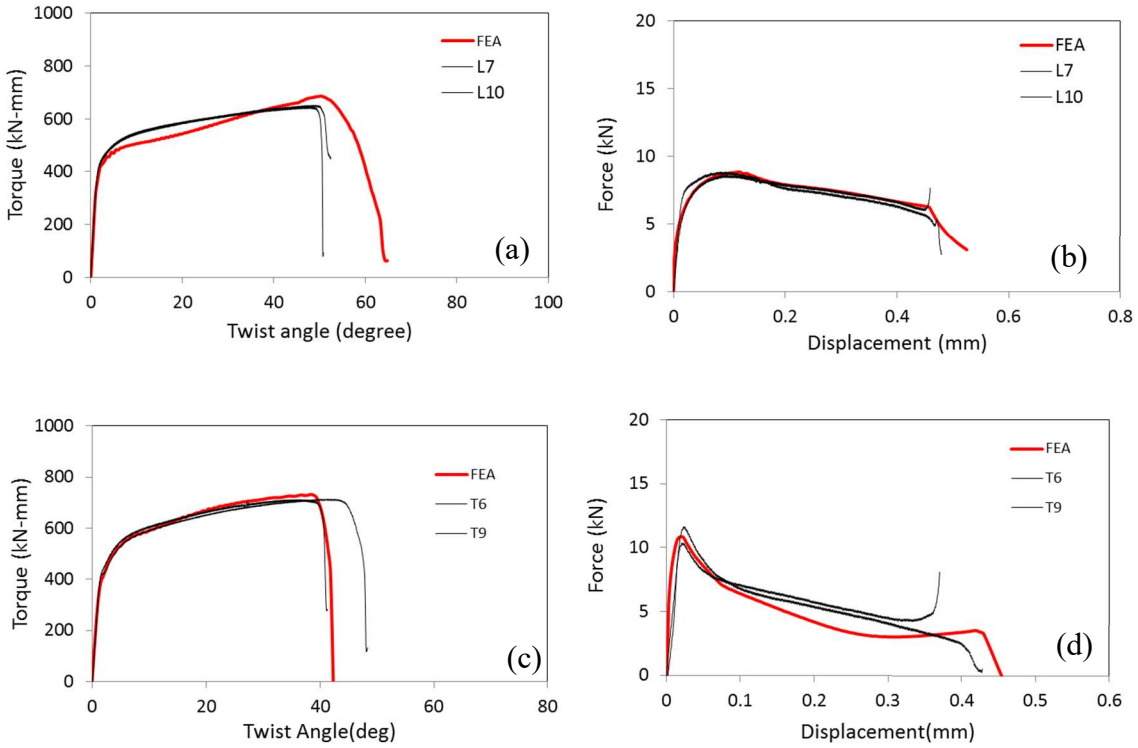

Figure 6.12. Comparisons between the numerical predictions and the experimental data for the tension-torsion specimen (tensile displacement/twist angel (mm/radian) = 0.5334) in rolling direction: (a) torque vs. twist angle; (b) axial force vs. axial displacement, and transverse direction: (c) torque vs. twist angle; (d) axial force vs. axial displacement

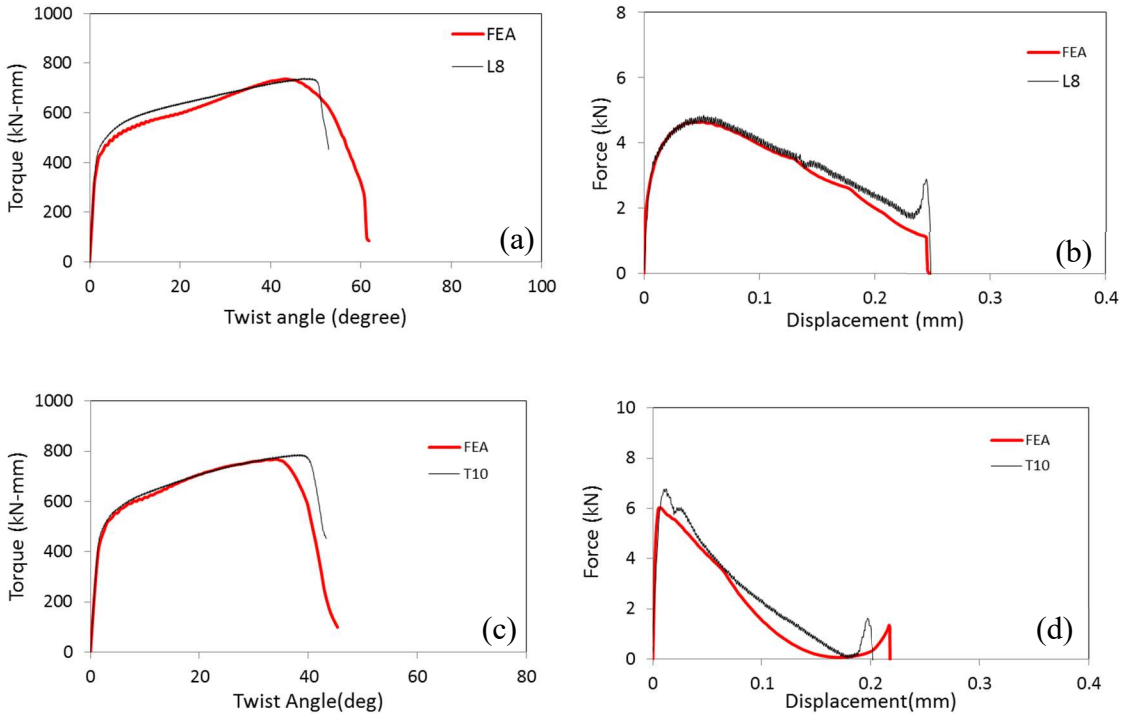

Figure 6.13. Comparisons between the numerical predictions and the experimental data for the tension-torsion specimen (tensile displacement/twist angle (mm/radian) = 0.2794) in rolling direction: (a) torque vs. twist angle; (b) axial force vs. axial displacement, and transverse direction: (c) torque vs. twist angle; (d) axial force vs. axial displacement

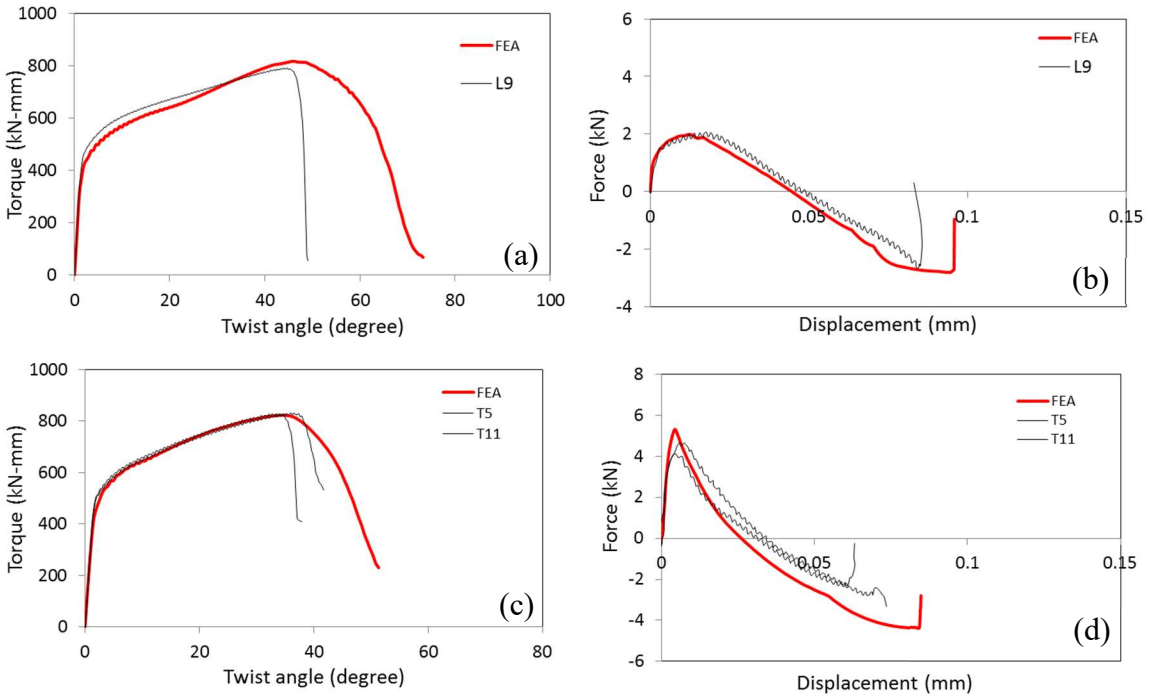

Figure 6.14. Comparisons between the numerical predictions and the experimental data for the tension-torsion specimen (tensile displacement/twist angel (mm/radian) = 0.10688) in rolling direction: (a) torque vs. twist angle; (b) axial force vs. axial displacement, and transverse direction: (c) torque vs. twist angle; (d) axial force vs. axial displacement

6.3.3 Prediction of fracture initiation and propagation

Fig. 6.15 shows the contour plots of the G-grooved plane strain specimen (groove radius is 5.08 mm) in RD. Both the stress triaxiality and the total damage have higher values in a region at the specimen center, shown in Figs. 6.15 (a-b). Figs. 6.15 (a-b) are the center section view of the specimen. Consequently, fracture initiates at the center of the specimen and propagates to the sides of the specimen, Fig. 6.15 (c). This figure is a front view of the specimen. Fig. 6.15 (d) shows the photo of a fractured specimen which verifies the simulation result shown in Fig. 6.15 (c).

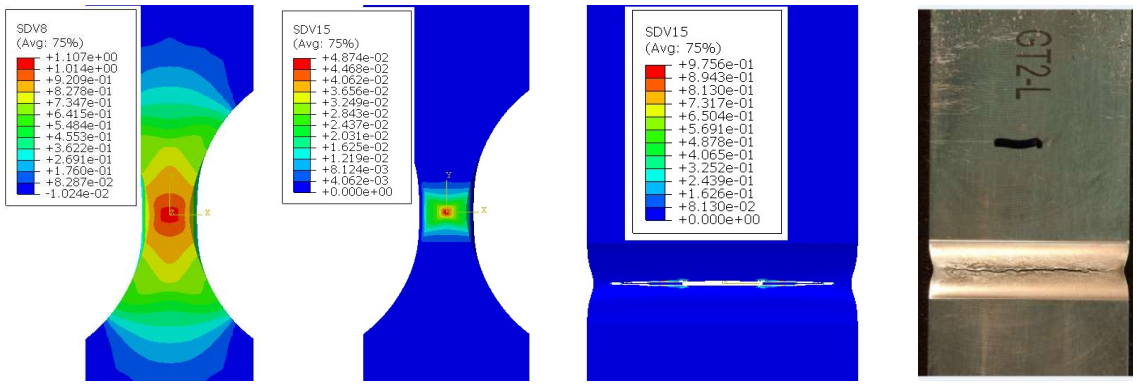

Figure 6.15. Crack initiation and growth in the flat grooved plane strain tensile specimens (groove radius is 5.08 mm) in the rolling direction: (a) contour plot of triaxiality before fracture initiation; (b) contour plot of total damage before fracture initiation; (c) final fracture; (d) photo of a fractured specimen.

Fig. 6.16 shows the fracture initiation and propagation process in the pure torsion specimen with the axis along TD. The maximum plastic strain occurs in the transition region due to strain concentration, and as a result, the shear damage is highest in the

transition region. The model predicts fracture initiates in the transition region and propagates circumferentially, Fig. 6.16 (c), which agrees with the experimental observation, Fig. 6.16 (d).

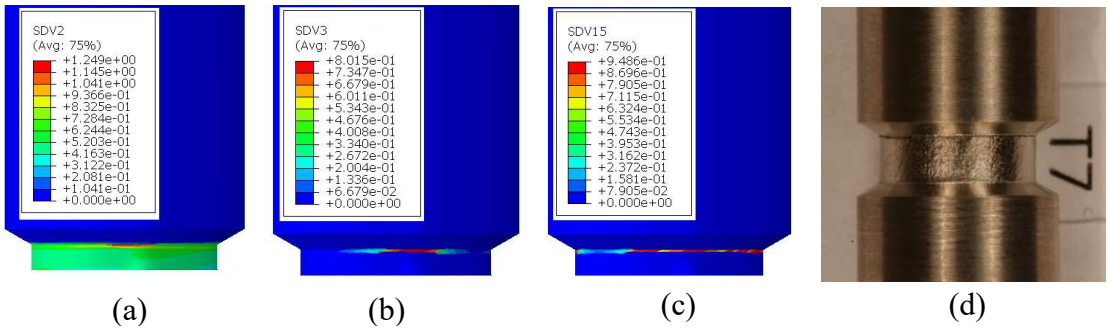

Figure 6.16. Crack initiation and growth in the pure torsion specimen (specimen axis is along the transverse direction): (a) equivalent plastic strain contour; (b) shear damage contour; (c) final fracture; (d) photo of the fractured specimen.

Fig. 6.17 shows the fracture initiation and propagation process in a tension-torsion specimen with a small tension-torsion ratio. Here the specimen axis is along TD and the applied tensile displacement/twist angle (mm/radian) ratio is 0.10688. Similar to the pure torsion specimen, fracture initiates at the transition region where the plastic strain is the highest and propagates circumferentially.

As the applied tension-torsion ratio changes, the stress state experienced by the material changes, which affects the ductile damage evolution process. Fig. 6.18 shows the fracture initiation and propagation process in a tension-torsion specimen with a larger applied tension-torsion ratio. Here the specimen axis is along TD and the applied tensile displacement/twist angle (mm/radian) ratio is 1.1684. The contour plots of equivalent

plastic strain, shear damage, porosity and total damage are shown in Figs. 6.18(a-d). In this case, fracture initiates at the outer equator in the middle of specimen gauge section and propagates circumferentially, Fig. 6.18 (e), which agrees with the experimental observation, Fig. 6.18 (f). Also a similar conical phenomenon in gage section was observed from both the simulation and experiment test result.

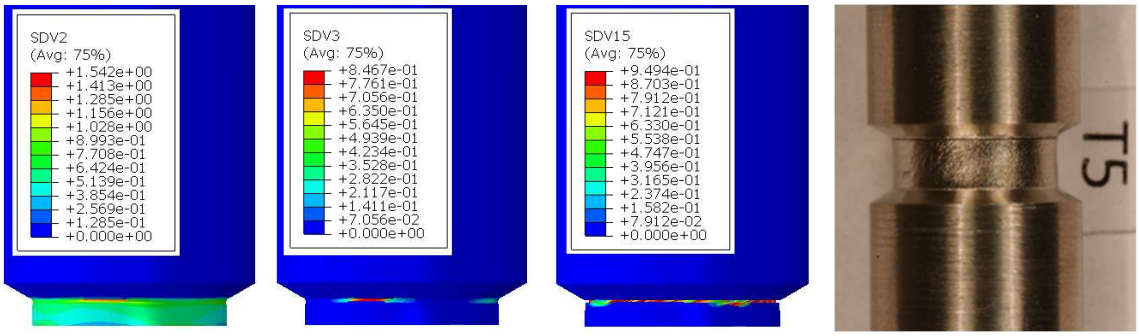

(a) (b) (c) (d)

Figure 6.17. Crack initiation and growth in the tension-torsion specimen (specimen axis is along the transverse direction; applied tensile displacement/twist angel ratio is 0.10688 mm/radian): (a) equivalent plastic strain contour; (b) shear damage contour; (c) final fracture; (d) photo of the fractured specimen.

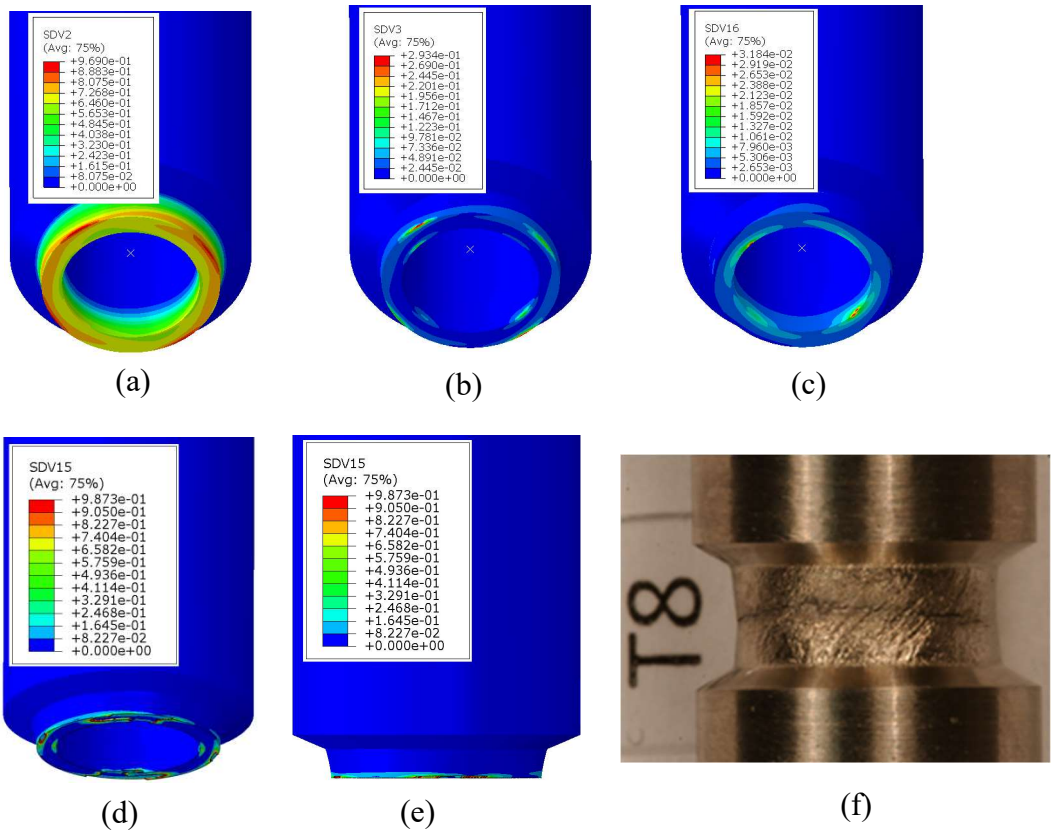

Figure 6.18. Crack initiation and growth in the tension-torsion specimen (specimen axis is along the transverse direction; applied tensile displacement/twist angel ratio is 1.1684 mm/radian): (a) equivalent plastic strain contour; (b) shear damage contour; (c) porosity; (d) total damage; (e) final fracture; (f) photo of the fractured specimen.

The change of fracture initiation locations reflects the damage evolution process in the specimen, which contains two contributions, void damage and shear damage. Figs. 6.19-6.21 show the damage evolution in the element where fracture initiated in the pure torsion specimen, the tension-torsion specimen (applied tensile displacement/twist angel ratio = 1.1684 mm/radian), and the B-notch specimen. In the pure torsion specimen, void nucleates at a plastic strain value around 0.22 but does not grow as plastic deformation increased. Therefore, the total damage is solely due to shear damage accumulation. In the tension-torsion specimen, both void growth and shear deformation contribute to the total damage. In the B-notch specimen, the total damage is almost entirely due to void growth. The model is able to capture the effect of stress state and the change of fracture mechanism.

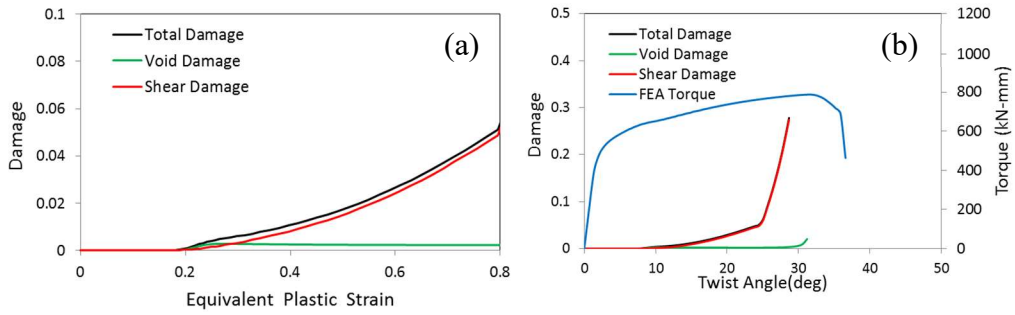

Figure 6.19. Pure torsion specimen in transverse direction: (a) damage evolution in a critical element in the transition region; (b) specimen torque vs. twist angle response and damage evolution in the critical element.

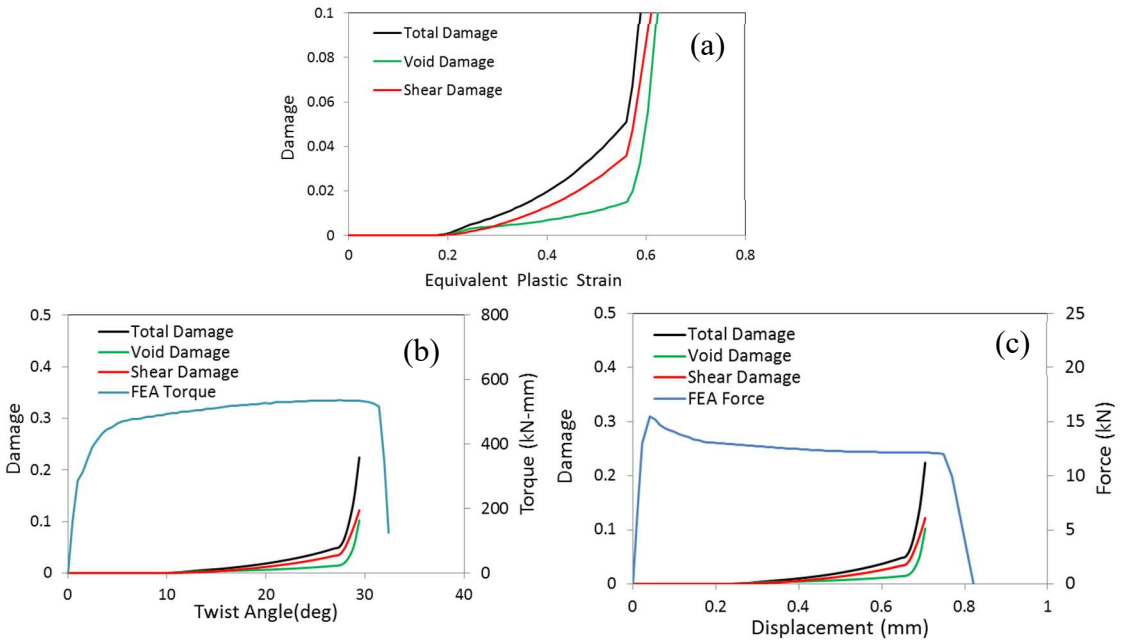

Figure 6.20. Tension-torsion specimen in transverse direction (the ratio of tensile displacement vs. twist angel = 1.1684 mm/radian): (a) damage evolution in the element at the outer equator of the specimen; (b) specimen torque vs. twist angle response and damage evolution in the critical element; (c) specimen axial force vs. axial displacement response and damage evolution in the critical element

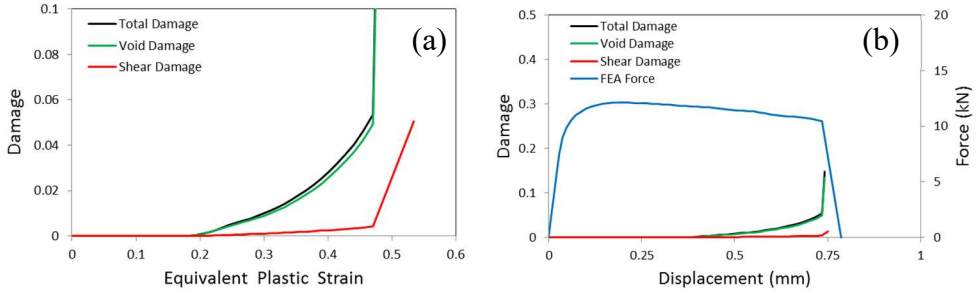

Figure 6.21. B-notch tensile specimen in transverse direction: (a) damage evolution in the center element; (b) specimen load-displacement response and damage evolution in the critical element

6.4 Concluding remarks

In this chapter, the shear-modified GTN model applied to anisotropic material is applied to describe the ductile fracture process in commercially pure titanium.

Uniaxial tension and compression tests were conducted at different orientations to quantify the plastic behavior of the material. It's found that not only the material exhibits strong plastic anisotropy and tension-compression asymmetry, but the extent of plastic anisotropy and strength differential response also evolves as the plastic deformation increases. Experiments of notched round specimens, grooved plane strain specimens, pure torsion specimens and tension-torsion specimens were conducted to consider the effect of stress state on ductile damage evolution. With carefully calibrated material parameters, the shear-modified GTN model applied with anisotropic material can accurately capture the responses of above specimens in terms of load-displacement or torque-twist angle curves and the fracture initiation locations.

CHAPTER VII

CONCLUSIONS AND FUTURE WORKS

7.1 Conclusions

In this dissertation, the micromechanics of ductile fracture process has been investigated from many perspectives. The conclusion from the study is summarized as following:

1.) A unit cell model consists of three void-containing material units is proposed based on the observation that plastic flow is localized in a band when ductile fracture occurs. Three material units are stacked in the direction normal to the localization plane, with the help of periodic boundary conditions and slightly void size differential, the localization can then take place in the middle material unit. This unit cell model allows material failure point to be unambiguously captured by the unloading of outside material units due to the loss of loading carrying capacity of the middle material unit. This failure criterion is very easy to implement in finite element analysis and proven to be robust for determining failure strain compare to previous models proposed by Barsoum and Faleskog (2007) and Wong and Guo (2015). Boundary conditions of this unit cell model are prescribed such that the macroscopic stress can be kept proportionally during the loading history, therefore a constant triaxiality and Lode parameter can be prescribed.

A series of unit cell analyses are conducted for various macroscopic stress triaxialities and Lode parameters. The analysis results confirm that for a fixed Lode

parameter, the failure strain decreases exponentially with the stress triaxiality and for a given stress triaxiality, it increases as L approaches -1 and 1. It is found that the effect of the Lode parameter is more pronounced when the stress triaxiality is low. The effect of the stress state on the orientation of the localization plane is investigated by considering T = 1 with varying L values following the approach of Barsoum and Faleskog (2011).

Additionally, analyses are conducted to study the effect of voids outside the localization band. It is found that for most cases voids in the outside layer do affect the stress state and void behavior in the inside layer and therefore should be accounted for in the unit cell model. The analysis results also reveal the effect of the stress state on the deformed void shape within and near the localization band. In particular, under shear dominated conditions, voids tend to elongate and rotate, resulting in spindle-shaped voids aligning towards the direction of the localization plane.

2). Hydrogen effect on material ductility is studied by incorporating the hydrogen diffusion process and the induced HELP effect into a unit cell model. A series of finite element analysis subjected to various stress states are carried out under certain loading speed. It's found that the loading speed of unit cell with initially evenly distributed hydrogen concentration will affect the ductility reduction intensity of HELP. Lower loading speed will accelerate the void growth process and reduce more failure strain until a low enough speed is reached. Lower than this certain speed, the failure strain will not be further reduced, and the hydrogen distribution is considered reaching a steady state. The analyses are then all conducted at a steady state loading speed for comparison on the same basis.

The analyses results reveal that the higher local stress and large deformation in the material will attract more hydrogen by generates new trapping sites, and higher hydrogen concentration in turn softens the material and leads to further localization of plastic strain and hydrogen concentration. The material softening effect of HELP is observed to be more effective on reducing material ductility when the hydrogen concentration site is at the region near the void surface, because softening in this region will significantly accelerate the void growth process. It's concluded from the analyses that that under stress state of higher triaxiality and near 0 Lode parameter, HELP will cause pronounced reduction in ductility because the plastic strain will be more localized into the region of near void surface under this stress state. Accordingly, the effect of hydrogen on ductile reduction will gradually diminish at lower stress triaxiality and Lode parameter increases or becomes more negative as the plastic strain localization is weaker at the area near the void surface.

3). Applied on isotropic material, the damage model of GTN and shear extended GTN model is carefully evaluated through a single material point test. It's shown that under uniaxial loading, both models predict identical result as there is no shear damage under this loading condition. But under general shear loading, the predicted result is much different because the shear caused damage is accounted in the shear extended GTN model. In the shear extended GTN model, the shear damage is more pronounced when the triaxiality is lower and the Lode parameter is close to 0. The shear damage will decrease as the Lode parameter value increase or becomes more negative and will increase when triaxiality becomes higher. But as the increase of shear damage for higher triaxiality is at a lower rate compared to the increase of volumetric damage, such that the volumetric damage will still become more dominant as the triaxiality is higher despite the increased shear damage.

When applied to an anisotropic material, the damage parameters in shear extended GTN model are influenced by the anisotropy of material, but still considered as ad-hoc parameters as they did not deviate much in terms of damage evolution from its carefully formed isotropic definition. However, this damage parameter setup nevertheless can describe complex ductile damage process accounting shear and volumetric damage when calibrated with experimental data. Together with the anisotropic plasticity calibrated for different stages of effective strain, the anisotropic damage model is capable of capture complex ductile fracture behaviors of various specimens under various loading condition covering a wide range of stress states.

7.2 Future works

The unit cell model supporting a simple and robust failure criterion was developed, but the matrix material of this model is currently narrowed to only isotropic and disregarded the effect of secondary void nucleation. With further implementation of anisotropic matrix material, this unit cell model could be used for quantifying the evolution of ductile damage affected by material anisotropy. With the consideration of void nucleation, a more realistic macroscopic material response can be obtained.

The unit cell model proposed in this dissertation is at the microscopic scale, experiments at this scale is rare and incomplete when the model was under development. Recently, research featuring micro-tension and micro shear experiments with very precise stress state control starts to emerge, such as Gorji and Mohr (2017), as well as in-situ tomography observations of these experiments done by Roth et al. (2018). The unit cell model can be calibrated and be compared against these newly generated experimental data

to further examine the assumptions and limitations of this model and the criterion. Much is expected to be learned during this process.

The effect of the stress state on the orientation of the localization plane considered in Chapter III following the approach of Barsoum and Faleskog (2011) did not consider the void topology change along different orientations of the localization plane. For example, when the orientation of the localization plane changed from 0 degree to 45 degrees, the voids on the localization plane is in fact also changed. If the distance between the voids along localization plane of 0 degree is l, then the distance between voids along localization plane of 45 degrees is now changed to $\sqrt{2}l$. If a method to account for this void topology can be established and tested, the effect of stress state on the orientation of localization plane can be established more realistically.

From what we have already learned from the unit cell model results, it's obvious that the effect of Lode parameter on failure strain is not symmetry to 0 Lode parameter value. We don't exactly know if this asymmetry should be attributed to shear damage or the volumetric damage. Further investigation could be done on this topic.

BIBLIOGRAPHY

ABAQUS Version 6.13, 2013. User's Manual Version 6.13 (Providence, RI, USA).

Ahn, D. C., Sofronis, P., & Dodds Jr, R. H.,2007. On hydrogen-induced plastic flow localization during void growth and coalescence. International Journal of Hydrogen Energy, 32(16), 3734-3742.

Bao, Y., Wierzbicki, T., 2004. On fracture locus in the equivalent strain and stress triaxiality space. Int. J. Mech. Sci. 46, 81-98.

Bai, Y. and Wierzbicki, T.,2008. A new model of metal plasticity and fracture with pressure and Lode dependence. International Journal of Plasticity, 24(6):1071-1096.

Barlat, F. , Lege, D. J. and Brem, J. C., 1991. A six-component yield function for anisotropic materials. International Journal of Plasticity, 7(7):693-712.

Barlat, F., Becker, R.C., Hayashida, Y., Maeda, Y., Yanagawa, M., Chung, K., Brem, J.C., Lege, D.J., Matsui, K., Murtha, S.J., Hattori, S., 1997. Yielding description of solution strengthened aluminum alloys. Int. J. Plast. 13:385–401.

Barsoum, I., Faleskog, J., 2007. Rupture mechanisms in combined tension and shear—Micromechanics. Int. J. Solids Struct. 44, 5481–5498.

Barsoum, I., Faleskog, J., 2011. Micromechanical analysis on the influence of the Lode parameter on void growth and coalescence. Int. J. Solids Struct. 48, 925-938.

Basu. S., Benzerga, A. A., 2015. On the path-dependence of the fracture locus in ductile materials: Experiments. Int. J. Solids Struct.71, 79-90.

Benzerga, A. A., Leblond, J., 2010. Ductile fracture by void growth to coalescence. Adv. Appl. Mech. 44, 169–305.

Birnbaum, H. K., & Sofronis, P.,1994. Hydrogen-enhanced localized plasticity—a mechanism for hydrogen-related fracture. Materials Science and Engineering: A, 176(1-2), 191-202.

Bridgeman, P.W., 1952. Studies in large plastic flow and fracture. McGraw-Hill Inc., New York.

Cazacu, O. and Barlat, F.,2004. A criterion for description of anisotropy and yield differential effects in pressure-insensitive metals. International Journal of Plasticity, 20(11):2027- 2045.

Cazacu, O., Plunkett, B., Barlat, F., 2006; Orthotropic yield criterion for hexagonal closed packed metals. Int. J. Plast. 22:1171 – 1194

Chateau, X., & Dormieux, L.,2002. Micromechanics of saturated and unsaturated porous media. International Journal for Numerical and Analytical Methods in Geomechanics, 26(8), 831-844.

Chu, C., Needleman, A., 1980; Void nucleation effects in biaxially stretched sheets. J. Eng. Mater. Technol. (Trans. ASME) 102: 249–256.

Chun, Y.B., Yu, S.L., Semiatin, S.L., Hwang, S.K., 2005; Effect of deformation twinning on microstructure and texture evolution during cold rolling of cp titanium. Mater. Sci. Eng. A 398: 209–219.

Dunand, M., Mohr, D., 2014. Effect of Lode parameter on plastic flow localization after proportional loading at low stress triaxialities. J. Mech. Phys. Solids 66, 133–153.

Faleskog, J., Gao, X., Shih, C.F., 1998. Cell model for nonlinear fracture analysis-I. Micromechanics calibration. Int. J. Fract. 89, 355-373.

Gao, X., Kim J., 2006. Modeling of ductile fracture: Significance of void coalescence. Int. J. Solids Struct. 43, 6277-6293.

Gao, X., Zhang, G., Roe, C., 2010. A study on the effect of the stress state on ductile fracture. Int. J. Damage Mech. 19, 75-94.

Garrison Jr, W.M., Moody, N.R., 1987. Ductile fracture. J. Phys. Chem. Solids. 48, 1035-1074.

Gorji, M.B. and Mohr, D., 2017. Micro-tension and micro-shear experiments to characterize stress-state dependent ductile fracture. Acta Materialia, 131, pp.65-76.

Graham, S.M., Zhang, T., Gao, X., Hayden, M., 2012; Development of a combined tension–torsion experiment for calibration of ductile fracture models under conditions of low triaxiality. Int. J. Mech. Sci. 54: 172-181.

Gurson, A.L.,1977. Continuum of ductile rupture by void nucleation and growth: Part I-Yield criteria and flow rules for Porous ductile media. J. Engng. Mater. Tech. 99, 2-55.

Hancock, J.W., Brown, D.K.,1983. On the role of strain and stress state in ductile failure. J. Mech. Phys. Solids 31, 1-24.

Hancock, J.W., Mackenzie, A.C.,1976. On the Mechanisms of ductile failure in high-strength steels subjected to multi-axial stress-states. J. Mech. Phys. Solids 24, 147-169.

Hänninen, H. E., Lee, T. C., Robertson, I. M., & Birnbaum, H. K.,1993. In situ observations on effects of hydrogen on deformation and fracture of A533B pressure vessel steel. Journal of materials engineering and performance, 2(6), 807-817.

Hanson, B.H., 1986; Present and future uses of titanium in engineering. Mater. Des. 7(6): 301–307.

Hill, R., 1948. A theory of the yielding and plastic flow of anisotropic metals. Proc. Roy. Soc. Lond., A 193(1033):281-297.

Hirth, J. P., 1980. "Effects of hydrogen on the properties of iron and steel." Metallurgical Transactions A, Vol. 11, No. 6, pp861-890.

Huang, C., Luo, T., Gao, X., Graham, S. M., 2018. Modeling the Effect of Hydrogen on Ductile Fracture. Materials Performance and Characterization, 7(2).

Hosford, W. F., Allen, T. J., 1973; Twinning and directional slip as a cause for a strength differential effect. Mater. Trans. 4:1424-1425.

Johnson Jr, C. E., & Bovey, F. A.,1958. Calculation of nuclear magnetic resonance spectra of aromatic hydrocarbons. The Journal of Chemical Physics, 29(5), 1012-1014.

Johnson, G.R., Cook, W.H., 1985. Fracture characteristics of three metals subjected to various strains, strain rates, temperatures and pressures. Engng. Fract. Mech. 21, 31-48.

Karafillis, A. P. and Boyce, M. C., 1993. A general anisotropic yield criterion using bounds and a transformation weighting tensor. Journal of the Mechanics and Physics of Solids, 41(12):1859-1886.

Kim, J., Gao, X., Srivatsan, T.S., 2004. Modeling of void growth in ductile solids: Effects of stress triaxiality and initial porosity. Engng. Frac. Mech. 71, 379-400.

Koplik, J., Needleman, A., 1988. Void growth and coalescence in porous plastic solids. Int. J. Solids Struct. 24, 835-853.

Lademo, O.G., Hopperstad, O.S., Langseth, M., 1999. An evaluation of yield criteria and flow rules for aluminum alloys. Int. J. Plast. 15:191–208.

Liang, Y., Sofronis, P., & Aravas, N.,2003. On the effect of hydrogen on plastic instabilities in metals. Acta Materialia, Vol. 51, No. 9, pp2717-2730.

Liang, Y., Ahn, D. C., Sofronis, P., Dodds, R. H., & Bammann, D., 2008. Effect of hydrogen trapping on void growth and coalescence in metals and alloys. Mechanics of Materials, Vol. 40, No. 3, pp115-132.

Liu, Z.G., Wong, W.H., Guo, T.F., 2016. Void behaviors from low to high triaxialities: Transition from void collapse to void coalescence. Int. J. Plast. 84,183-202.

Lode, W. Z.,1926. Versuche über den Einfluß der mittleren Hauptspannung auf das Fließen der Metalle Eisen, Kupfer und Nickel. Physik,36,11-12: 913-939

Luo, T., & Gao, X.,2018. On the prediction of ductile fracture by void coalescence and strain localization. Journal of the Mechanics and Physics of Solids, 113, 82-104.

Malcher, L. Andrade Pires, F.M., Cesar de Sa, J.M.A. 2014. An extended GTN model for ductile fracture under high and low stress triaxiality. Int. J. Plast. 54,193-228.

Maier, J.,1995. Ionic conduction in space charge regions. Progress in solid state chemistry, 23(3), 171-263.

McClintock, F.A., 1968. A criterion of ductile fracture by the growth of holes. J. Appl. Mech. 35, 362-371.

Mear, M. E., & Hutchinson, J. W.,1985. Influence of yield surface curvature on flow localization in dilatant plasticity. Mechanics of Materials, 4(3-4), 395-407.

Mohr, D., & Marcadet, S. J.,2015. Micromechanically-motivated phenomenological Hosford–Coulomb model for predicting ductile fracture initiation at low stress triaxialities. International Journal of Solids and Structures, 67, 40-55.

Nahshon, K., Hutchinson, J.W., 2008. Modification of the Gurson model for shear fracture. Eur. J. Mech./A Solids 27, 1–17.

Needleman, A., Tvergaard, V., 1992. Analysis of plastic flow localization in metals. Appl. Mech. Rev. 45, S3–S18.

Nielsen, K.L., Dahl, J., Tvergaard, V., 2012. Collapse and coalescence of spherical voids subject to intense shearing: studies in full 3D. Int. J. Fract. 177, 97–108.

Oh, C. S., Kim, Y. J., & Yoon, K. B., 2010. Coupled analysis of hydrogen transport using ABAQUS. Journal of Solid Mechanics and Materials Engineering, Vol. 4, No. 7, pp908-917.

Oriani, R. A.,1970. The diffusion and trapping of hydrogen in steel. Acta metallurgica, 18(1), 147-157.

Papasidero, J., Doquet, V., Mohr, D., 2015. Ductile fracture of aluminum 2024-T351 under proportional and non-proportional multi-axial loading: Bao–Wierzbicki results revisited. Int. J. Solids Struct. 69-70, 459-474.

Peisl, H.,1978. Lattice strains due to hydrogen in metals. In Hydrogen in metals I (pp. 53-74). Springer, Berlin, Heidelberg.

Revil-Baudard, B., Cazacu, O., Flater, P., Chandola, N., Alves, J.L., 2016; Unusual plastic deformation and damage features in titanium: Experimental tests and constitutive modeling, J. Mech. Phys. Solids 88: 100–122

Revil-Baudard, B., Yoon, J., Stewart, J.B., Cazacu, O., 2012; On the influence of damage evolution in an incompressible material with matrix displaying tension-compression asymmetry. Procedia IUTAM 3: 331-349.

Rice, J.R., 1977. The localization of plastic deformation. In: Koiter, W.T. (Ed.), Proceedings of the 14th International Congress on Theoretical and Applied Mechanics. North-Holland, Amsterdam, 207–220.

Rice, J.R., Tracey, D.M., 1969. On the ductile enlargement of voids in triaxial stress fields. J. Mech. Phys. Solids 17, 201-217.

Roth, C.C., Morgeneyer, T.F., Cheng, Y., Helfen, L. and Mohr, D., 2018. Ductile damage mechanism under shear-dominated loading: In-situ tomography experiments on dual phase steel and localization analysis. International Journal of Plasticity.

Robertson, I. M., & Birnbaum, H. K.,1986. An HVEM study of hydrogen effects on the deformation and fracture of nickel. Acta Metallurgica, 34(3), 353-366.

San Marchi, C., Somerday, B. P., Tang, X., & Schiroky, G. H.,2008. Effects of alloy composition and strain hardening on tensile fracture of hydrogen-precharged type 316 stainless steels. International Journal of Hydrogen Energy, 33(2), 889-904.

Salem, A.A., Kalidindi, S.R., Doherty, R.D., 2003; Strain hardening of titanium: role of deformation twinning. Acta Mater. 51: 4225–4237

Sofronis, P., & McMeeking, R. M.,1994. The effect of interface diffusion and slip on the creep resistance of particulate composite materials. Mechanics of materials, 18(1), 55-68.

Sofronis, P., & McMeeking, R. M.,1989. Numerical analysis of hydrogen transport near a blunting crack tip. Journal of the Mechanics and Physics of Solids, 37(3), 317-350.

Stewart, J.B., Cazacu, O.,2011. Analytical yield criterion for anisotropic material containing spherical voids and exhibiting tension-compression asymmetry. Int. J. Solids Struct. 48:357-373.

Tabata, T., & Birnbaum, H. K.,1983. Direct observations of the effect of hydrogen on the behavior of dislocations in iron. Scripta Metallurgica, 17(7), 947-950.

Taha, A., & Sofronis, P.,2001. A micromechanics approach to the study of hydrogen transport and embrittlement. Engineering Fracture Mechanics, 68(6), 803-837.

Tekoğlu C, Hutchinson JW, Pardoen T. 2015. On localization and void coalescence as a precursor to ductile fracture. Phil. Trans. R. Soc. A 373, 20140121.

Thomas, N., Basu, S., Benzerga, A. A., 2016. On fracture loci of ductile materials under non-proportional loading. Int. J. Mech. Sci. 117, 135-151.

Troiano, A. R.,1960. The role of hydrogen and other interstitials in the mechanical behavior of metals. trans. ASM, 52, 54-80.

Tvergaard, V., 1981. Influence of voids on shear band instabilities under plane strain conditions. Int. J. Fract. 17, 389-407.

Tvergaard, V., 1982. On localization in ductile materials containing spherical voids, Int. J. Fract. 18, 237-252.

Tvergaard, V., 2008. Shear deformation of voids with contact modeled by internal pressure. Int. J. Mech. Sci. 50, 1459–1465.

Tvergaard, V., 2009. Behavior of voids in a shear field. Int. J. Fract. 158, 41–49.

Tvergaard, V., 2012. Effect of stress-state and spacing on voids in a shear-field. Int. J. Solids Struct. 49, 3047–3054.

Tvergaard, V., Needleman, A., 1984. Analysis of the cup-cone fracture in a round tensile bar. Acta. Metall. 32, 157-169.

Van Stone, R.H., Cox, T.B., Low Jr, J.R., Psioda, J.A., 1985. Microstructural aspects of fracture by dimple rupture. Int. Met. Rev. 30, 157-179.

Vlasov, N. M., & Zaznoba, V. A.,1999. Diffusion processes in the vicinity of triple conjunctions of special grain boundaries. Fizika Tverdogo Tela, 41(1), 64-67.

Wong, W.H., Guo, T.F., 2015. On the energetics of tensile and shear void coalescences. J. Mech. Phys. Solids 82, 259-286.

Xue, L., 2007. Damage accumulation and fracture initiation in uncracked ductile solids subject to triaxial loading. International Journal of Solids and Structures, 44(16):5163-5181

Xue, L., 2008. Constitutive modeling of void shearing effect in ductile fracture of porous materials. Eng. Fract. Mech. 75, 3343–3366.

Yamamoto, H.,1978. Conditions for shear localization in the ductile fracture of void-containing materials. International Journal of Fracture, 14(4), 347-365.

Zhai, J. Luo, T., Gao, X., Graham, S.M., Baral, M, Korkolis, Y.P., Knudsen, E., 2016, Modeling the ductile damage process in commercially pure titanium. Int. J. Solids Struct. 91, 26-45.

Zhou, J., Gao, X., Hayden, M., Joyce, J.A., 2012. Modeling the ductile fracture behavior of an aluminum alloy 5083-H116 including the residual stress effect. Eng. Fract. Mech. 85, 103-116.

Zhou, J., Gao, X., Sobotka, J.C., Webler, B.A., Brian, V., Cockeram, B.V., 2014. On the extension of the Gurson-type porous plasticity models for prediction of ductile fracture under shear-dominated conditions. Int. J. Solids Struct. 51, 3273–3291.